Stony Brook University

Electromechanical Response of Piezoelectric Cellular Architectures: The effect of topological features and deformation modes

A Dissertation presented

by

Sumantu Iyer

to

The Graduate School

in Partial Fulfillment of the

Requirements

for the Degree of

Doctor of Philosophy

in

Mechanical Engineering

Stony Brook University

August 2014

Stony Brook University

The Graduate School

Sumantu Iyer

We, the dissertation committee for the above candidate for the
Doctor of Philosophy degree, hereby recommend
acceptance of this dissertation.

Dr. Maen Alkhader - Dissertation Advisor
Assistant Professor, Mechanical Engineering

Dr. Robert V. Kukta - Chairperson of the Defence
Associate Professor, Mechanical Engineering

Dr. David Hwang
Assistant Professor, Mechanical Engineering

Dr. T.A. Venkatesh
Associate Professor, Materials Science and Engineering

This dissertation is accepted by the Graduate School

Charles Taber
Dean of the Graduate School

ii

Abstract of the dissertation

Electromechanical Response of Piezoelectric Cellular Architectures: The effect of topological features and deformation modes

by

Sumantu Iyer

Doctor of Philosophy

in

Mechanical Engineering

Stony Brook University

2014

Piezoelectric composites have played a major role in significantly enhancing the capabilities of hydrophones, sensors and actuators by providing better electromechanical coupling and lower acoustic impedances when compared to monolithic piezoelectric ceramics. Recent developments in the field of piezoelectric composites has led to the investigation into piezoelectric cellular designs that have the potential to further increase the sensitivity of existing piezoelectric devices. Accordingly the present study involves:- i) Investigating the role of topology and the direction of poling on the effective properties of piezoelectric cellular solids; ii) The role of deformation mechanisms on the structure-property relation of piezoelectric cellular architectures to categorize cellular topologies based on the dominant mode of deformation (i.e., bending vs. stretching) and iii) Develop an analytical model based on the homogenization technique to predict the overall electromechanical properties of piezoelectric foam structures. First, a finite element model is developed to characterize the complete electromechanical properties of the most general

form of elastically anisotropic and piezoelectrically active foams with honeycomb structures has been proposed. Four classes of piezoelectric honeycomb structures are identified depending on the relative orientation of the poling direction with the porosity direction (longitudinal and transverse) and the geometry of the honeycombs (isotropic and anisotropic).

To study the role of the major deformation modes in the ligaments of piezoelectric cellular struts on the effective electromechanical properties of the given cellular topology, three main architectures (foams) that exemplify bending and stretching dominated piezoelectrically active cellular solids cellular solids are considered. These structures represent hexagonal, tetragonal and triangular cellular topologies with the connectives of three, four and six cell walls per vertex, respectively.

An analytical framework based on the homogenization method has been developed to predict the effective electromechanical properties of periodic, particulate and porous, piezoelectric composites with anisotropic constituents. Expressions are provided for the effective moduli tensors of n-phase composites based on the respective strain and electric field concentration tensors. By taking into account the shape and distribution of the inclusion and by invoking a simple numerical procedure, solutions for the electromechanical properties of a general anisotropic inclusion in an anisotropic matrix are obtained.

Finally using Bloch's theorem in conjunction with finite element analysis, this work investigates the relationships between inherent microstructural features (such as lattice symmetry, relative density and constituent material) and the acoustic properties (such as wave dispersion, band gaps, and acoustic anisotropy) of architectured lattice materials. The coupling between microstructural features and band gaps is investigated in hexagonal lattice geometry which is inspired by the two dimensional Bravais family of lattices.

To my parents

Contents

List of Figures

xi

List of Tables

Acknowledgements

Much thanks must be given to my dissertation advisors, Prof. Maen Alkhader and Prof. T.A. Venkatesh. It is only with their expert guidance that I have got this far with my research. They have instilled in me a sense of scientific inquisitiveness that I cannot thank them enough for.

Prof. Maen Alkhader has been a deeply insightful person to work and interact with over the past three years. His in-depth knowledge in the field of finite-element analysis threw a new light on a subject I had been working on prior to our association. His openness in trying out new ideas has brought about many fruitful collaborations in our work on piezoelectric cellular architectures. His relaxed method of functioning allowed me to experiment with new ideas by eliminating the fear of failure. I have had a wonderful time associating with him outside of the workspace where his friendly nature makes interacting with him a joyous experience.

I have known Prof. T.A. Venkatesh since January 2009, when I walked into his office as a fresh Masters student in Mechanical Engineering. He introduced me to a method of expanding ones scientific knowledge by asking pertinent questions and never resting till a solution is reached. I will always cherish the many discussions we have had over the years and cannot thank him enough for showing faith in me.

I must mention the contribution of Prof. Oscar Lopez-Pamies who introduced me to the concept of analytical modeling. His acute knowledge on the subject helped sharpen many conceptual ideas, that culminated in the homogenization model derived in this dissertation.

I am also grateful to Prof. Robert V. Kukta for helping at multiple times during my Ph.D. I appreciate all the help that he provided me by hiring me as the Teaching Assistant in his courses which helped me learn the value of

CHAPTER 1

Introduction

1.1 Prior work in the area of cellular architectures

Cellular materials in the form of foams [8, 9], hierarchical and lattice-based architectures [10, 11, 12, 13] have gained substantial importance in a wide range of automotive (e.g. [14, 15, 16]), aerospace (e.g. [3, 17]), naval (e.g. [18, 19]), and biomedical (e.g. [9, 20, 21]) applications. Traditionally, cellular solids have been attractive for their ability to provide, at low densities, many practical properties such as significant stiffness and strength as well as energy absorption capabilities. More recently, cellular solids have also been recognized for their tremendous potential as multifunctional and active materials and several efforts have been focused on developing smart foam materials from electric field activated piezoelectric materials [22, 23, 24, 25, 26], temperature activated shape memory materials and magnetic field activated shape memory materials [27].

Amongst smart foams, piezoelectric foams, with their electromechanical coupling properties and low densities, have been recognized for their unique set of piezoelectric properties such as reduced acoustic impedance and enhanced sensitivity which are desirable in many sensor and device applications such as hydrophones. Consequently, several experimental studies, analytical and numerical models have been developed towards understanding the electromechanical properties of piezoelectric foams with both closed type porosity (i.e., 3-0 connectivity) and open type porosity (i.e., 3-1 and 3-3 connectivity) [28, 29].

Haun and Newnham fabricated 1-3-0 type piezoelectric lead zirconate titanate (PZT) - polymer composites using a single large void at the center

of the composite and showed that such a composite significantly enhances a hydrophones sensing abilities by increasing the figures of merit such as the hydrostatic strain coefficient (d_h) and the hydrostatic figure of merit $(d_h \cdot g_h)$ [28]. Arai et al. constructed a hydrophone using porous piezoelectric ceramics of 3-0 type and demonstrated that the hydrophone sensitivity was higher than that of solid piezoceramic by 20 db [30]. Li et al. used a sintering process to fabricate 3-0 type porous piezoelectric ceramics and observed a large increase in the piezoelectric charge coefficient with increasing porosity volume fraction [31]. Marselli et al. also fabricated 3-0 type porous PZT piezoelectric materials which exhibited hydrostatic figures of merit which were significantly higher than that observed in solid PZT [32]. Ueda et al. presented PZT based 3-0 type cellular architectures that exhibited large-strain responses using a multilayer mechanism which overcomes the small-strain limitation of solid piezoelectric ceramic materials thereby making them useful for a broad range of applications. Ting et al. studied the effects of several materials and processing parameters on the piezoelectric properties and identified an epoxy coating on a 3-0 type porous sample to generate improved piezoelectric figures of merit [33, 34].

Bast and Wersing showed that the acoustic impedance (Z) for PZT materials with 3-1-type porosity decreases with increasing porosity volume fraction [35]. Wirges et al. developed an optimized sequence of steps for preparing 3-1 type piezoelectric structures from non-voided polyethylene tetraphalate (PETP) films by foaming with carbon dioxide, biaxial mechanical stretching, controlled void inflation and bipolar electric discharge. Their new optimized PETP foams exhibited a large piezoelectric coefficient with low elastic stiffness [36].

Roncari et al. demonstrated that by using different techniques to fabricate the 3-3 type porous PZT composites, the pore size distribution, pore volume fractions and their acoustic impedance could be affected significantly. Lee et al. also fabricated 3-3- type porous PZT-PZN piezoelectric materials using a ball-milling method and reported large hydrostatic figures of merit values as well [37, 38].

Analytical models developed to study the behavior of composite piezoelectric materials include the preliminary works by Banno who used a modified cubes model to explain the behavior of piezoelectric ceramics with closed pores (3-0 type) and open pores (3-1 type) [39]. Dunn and Taya solved the equivalent Eshelby inclusion problem for a single ellipsoidal inclusion in an infinite piezoelectric medium using the Greens function approach [40, 41]. By combining their results for a single particle with the effective medium approach of Mori and Tanaka, they derived closed form solutions for porous piezoelectric materials with 3-0 type closed porosity and with 3-1 type open porosity for the case of piezoelectric materials that exhibit transverse isotropy in their elastic properties. Bowen and Topolov also provided a method to predict the electromechanical properties of piezoelectric materials with 3-0 type closed porosity and 3-1 type open porosity as well [42]. Gomez and Espinosa derived a model to predict the dielectric properties of porous piezoelectric materials and the dielectric coupling generated by the introduction of a second phase to the pores as well [43].

Challagulla and Venkatesh [44] formulated an asymptotic homogenization method to obtain the complete electromechanical properties of 2-2 type layered composites with anisotropic constituents. They studied two classes of layered piezoelectric composites (i.e., longitudinally layered and transversely layered) to obtain the effective properties in the limits of both large-volume (i.e., bulk) and small-volume (i.e., thin-film) systems. An extension of the asymptotic homogenization method to obtain the properties of 1-3 type long-fiber piezoelectric composites with transversely isotropic constituents was presented in the works of Bravo-Castillero,et al. [2]. Bisegna and Luciano [45, 46] provided variational bounds to estimate the homogenized properties of piezoelectric composites as well. Hori and Nemat-Nasser [47] have obtained Hashin-Shtrikman type exact bounds for electroactive composites. The bounds presented by them are general and apply to non-linear constituent phases although exact solutions are not provided for the fully anisotropic matrix-particle material property tensors.

A summary of the existing analytical and numerical models developed to

Table 1.1: A summary of the analytical and numerical models developed to predict the electromechanical response of three types of piezoelectric composites.

Existing models developed to predict the effective properties of piezoelectric composites.			
		Particulate composites	Long-fiber composites	Laminate-composites

		Particulate composites	Long-fiber composites	Laminate-composites
Analytical Models	Transversely Isotropic	Dunn and Taya [48] Mikata [51]	Dunn and Taya [49] Mikata [52] Bravo-Castillero et al. [53]	Otero et al. [50]
	Anisotropic	Banno [39] Hori and Nemat-Nasser [47] Bowen and Topalov [55] Present Model	Banno [39] Hori and Nemat-Nasser [47] Bowen and Topalov [55] Kar-Gupta and Venkatesh [57] Present model	Banno [39] Lee [54] Hori and Nemat-Nasser [47] Chen et al. [56] Bowen and Topalov [55] Challagulla and Venkatesh [44] Present model
Numerical Models	Transversely Isotropic	Kar-Gupta and Venkatesh [58]	Pettermann and Suresh [59] Kar-Gupta and Venkatesh [61]	Kar-Gupta and Venkatesh [60]
	Anisotropic	Kar-Gupta and Venkatesh [58] Iyer and Venkatesh [63]	Pettermann and Suresh [59] Kar-Gupta and Venkatesh [58] Iyer and Venkatesh [64]	Wang [62] Kar-Gupta and Venkatesh [60]

study the effective response of periodic piezoelectric composites is presented in Table 1.1.

Iyer and Venkatesh developed three-dimensional finite element models to characterize the electromechanical response of 3-0 type closed foams and demonstrated that such closed foam systems exhibited a strong dependence on the shape of the enclosed porosity [24, 25]. Kar-Gupta and Venkatesh also developed numerical models to examine the electroelastic properties of 3-1 type open foam structures with circular and elliptical porosity and demonstrated that the orientation of the porosity with respect to the poling direction had a significant influence on the effective piezoelectric properties [26, 65]. Marcheselli and Venkatesh presented models to characterize the piezoelectric properties of 3-1 type open foam structures with hollow fibers and demonstrated that the effective properties of such foam materials can be suitably tailored by

modifying the matrix and the fiber material [66]. Challagulla and Venkatesh developed three-dimensional finite-element models to completely characterize the elastic, dielectric and piezoelectric properties of 3-3 type open piezoelectric foam structures with asymmetric interconnects, symmetric interconnects, and without any interconnects and benchmarked them with respect to 3-1 type long porous piezoelectric foams [22, 23, 67]. Bosse et al. extended the work of Challagulla and Venkatesh and investigated the role of porosity shape in determining the effective properties of 3-3 type open piezoelectric foams [67].

One of the most significant issues related to topology-property coupling is the role of the dominant deformation mode. Existing piezoelectric foams have architectures with low nodal connectivity (i.e. average number of ligaments connected to a vertex is approximately three). It is generally recognized that the low connectivity of solid foams leads to a bending dominated deformation mode (i.e. cell walls deform mainly by bending), and therefore, their macroscopic mechanical properties (i.e. stiffness and strength) are far from being optimal [68, 69]. Similarly, the electromechanical properties of piezoelectric foams with low nodal connectivity might be far from optimal. To understand the impact of deformation mode on the electromechanical properties one can refer to scaling laws developed for structural passive cellular solids [70]. These laws show that stiffness and strength for bending dominated 2D foam structures scale with relative density as $\overline{\rho}^3$ and $\overline{\rho}^2$, respectively. On the other hand, stiffness and strength, for 2D cellular solids whose cell walls deform mainly by stretching (i.e. stretching dominated foam), scale linearly with relative density as $\overline{\rho}$. Clearly, switching ligament deformation mode from bending to stretching is accompanied by an order of magnitude increase in the mechanical properties (i.e., stiffness and strength), especially at very low relative densities (<30%). Generalizing these trends and extending them to piezoelectric foams is not straightforward as the role of deformation modes on the electromechanical response of piezoelectric foams is inherently more complex than in structures with non-active constituents. The added complexity is due to the anisotropy of the foam constituent material (i.e., piezoelectric

5

material), the coupled electro-mechanical nature of the problem, the sensitivity of the foam properties to the poling direction and its orientation with respect to the porosity of cellular solids. Nevertheless, it can be predicted that in bending-dominated foam, the deformation is not uniform and is localized near vertices while large population of the cell walls will be almost stress free. Accordingly, charge will be localized near bending zones, while a majority of the ligaments will be charge free. In addition, at charge localized zones, the charge will change sign abruptly across the thin ligaments as one side is under tension and the other is under compression. On the other hand, in stretching-dominated foams, deformation and charge distribution will be more uniform, in terms of magnitude and sign. So, stretching-dominated piezoelectric foams will exhibit higher stiffness, strength, toughness, better load sharing, more uniform deformations and uniform charge, as compared to bending dominated foams.

Periodic cellular (lattice) materials, by virtue of their repeating microstructures and associated geometric impedance mismatch, also exhibit wave dispersion, frequency dependent transmissibility, and directional characteristics that are inherently dependent on their constituent material and mesoscale microstructural features [71]. These characteristics render lattice materials as potential candidates to perform as low frequency phononic crystals and metamaterials for radar, sonar, wave guiding, wave modulation and isolation applications. To accelerate the wide-spread implementation of lattice materials as hinges for phononic crystals, it is of empirical importance to first establish the ability to engineer them to exhibit application-tailored properties and tunable behavior (e.g. to activate/deactivate band gaps). Achieving tunability and application-oriented tailorablity requires an understanding of the phononic, acoustic, wave dispersive and directional properties of the lattices and their interactions with various lattice features (e.g., cell wall thickness, ligament deformations modes, etc.)[72].

Accordingly, using Bloch's theorem in conjunction with finite element

analysis, this work investigates the relationships between inherent microstructural features (such as lattice symmetry, relative density and constituent material) and the acoustic properties (such as wave dispersion, band gaps, and acoustic anisotropy) of architectured lattice materials [73]. The coupling between microstructural features and band gaps is investigated in hexagonal lattice geometry which is inspired by the two dimensional Bravais family of lattices. Results illustrate that band structure and phononic properties are highly sensitive to relative density and can scale non-uniformly with it as eigenmodes are associated with relative density dependent deformation mechanisms. Moreover, results show that band gaps can potentially be activated and deactivated using macroscopic strain fields. The latter opens horizons for realizing cellular based phononic crystals with tunable properties.

1.2 Outline of the dissertation

Overall, a comprehensive set of models and results exist to demonstrate that the introduction of (closed or open) porosity in piezoelectric materials enhances their utility in certain practical applications. Furthermore, the influence of microstructural features on the effective properties of certain classes of piezoelectric foams such as those exhibiting 3-3 type connectivity have been presented [32, 38]. However, within the context of 3-1 type piezoelectric foams, the effective electromechanical properties of honeycomb-type foam structures have not yet been investigated.

Moreover it has been well established that periodic composite materials exhibit wave dispersive properties due to the repeating lattice structure and material properties mismatch. However whether cellular solids can expand the scope of the current applicability of lattice architectures to provide a noiseless environment in devices, is yet to be established. It will be shown that the cellular topologies studied in the current work, can operate in the sub kHz range and block out undesirable frequencies and provide a vibrationless environment.

Furthermore, as passive honeycomb type foam structures with their unique and tailorable microstructural and topological features have already been proven

to provide enhanced stiffness to out-of-plane shear deformations, an interesting question that follows naturally is:

"Can active honeycomb foams with a desirable combination of mechanical stiffness, piezoelectric properties and dynamic properties be developed?"

Hence, the objectives of the present study are:

1. To develop a finite element model to characterize the complete electromechanical properties of the most general form of elastically anisotropic and piezoelectrically active foams with honeycomb structures;

2. To establish the relationships between the microstructural features of the honeycomb structures and their effective properties over a range of relative densities; and

3. To identify novel piezoelectric honeycomb structures that provides the best combination of mechanical and piezoelectric properties.

4. To realize the potential of cellular topologies as frequency band gap generators to be applied as noise filters, wave guides and acoustic isolators.

The present work has been organized as follows. Chapter 2 concerns a detailed analysis on the electromechanical response of piezoelectric cellular architectures using a finite-element model. Chapter 3 looks at the electromechanical response of cellular solids and the role of cellular topology by studying the dominant deformation modes in the struts of a given cellular solid. The role of bending vs. stretching deformation in the struts is looked at by analysing three characteristic unit-cells. Chapter 4 presents the details of the analytical model developed to study and characterize piezoelectric particulate/porous composites using a homogenization method. Finally, Chapter 5 contains details of the method used in studying the frequency-structure coupling properties of cellular architectures.

Electromechanical Response of Piezoelectric Honeycomb Foam Structures

2.1 Outline of the chapter

The present work has been organized as follows. Section 2.2 illustrates a classification of porous piezoelectric materials. Section 2.3 highlights the constitutive relations that govern the behavior of coupled piezoelectric materials in the linear elastic domain and identifies the characteristic figures of merit of significance to the applications of piezoelectric materials (e.g., in sensors). Section 2.4 presents the details of the finite element-based numerical model developed in the present study to characterize the effects of microstructural features and relative densities on the electro-elastic behavior of piezoelectric honeycomb foam structures. The electromechanical properties of piezoelectric honeycomb structures predicted by the finite element model are discussed in Section 2.5 and principal conclusions from the present study are highlighted in Section 2.6.

2.2 Classification of Piezoelectric Honeycomb Foams

In general, piezoelectric foam materials can be grouped into three distinct types:

1. 3-0 type, where the porosity is enclosed in all three dimensions by the continuous matrix phase;

2. 3-1 type, where the porosity exhibits connectivity in the 1-direction, which is similar to the case of long fibers embedded in the continuous

matrix phase which is connected to itself in all three directions.

3. 3-3 type, where the porosity exists in an open inter-connecting network where both the matrix phase and the porosity exhibiting connectivity in all three directions.
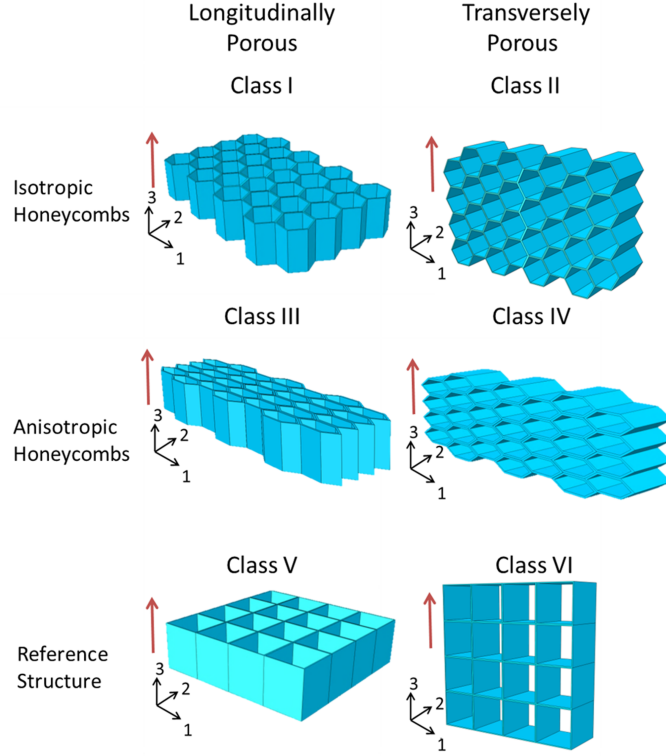
Figure 2.1: Schematic illustration showing: Schematic illustrating four classes of (longitudinally or transversely porous and isotropically or anisotropically shaped) piezoelectric honeycomb foam structures (with hexagonal porosity) and two classes of reference foam structures (with square porosity) investigated in the present study. (The poling direction is indicated by the red arrow).

The honeycomb foam structures considered in the present study exhibit 3-1 type connectivity. Depending on the relative orientation of the poling direction with the porosity direction and the geometry of the honeycombs, four classes of piezoelectric honeycomb foam structures are identified (Fig. 2.1):

1. Longitudinally porous honeycombs: Structures where the poling direction is parallel to the porosity direction.

2. Transversely porous honeycombs: Structures where the poling direction is orthogonal to the porosity direction.

3. Isotropic/Regular honeycombs: Structures which exhibit in-plane geometric isotropy with an aspect-ratio of $\sqrt{3}$.

4. Anisotropic/Irregular honeycombs: Structures which exhibit in-plane geometric anisotropy with an aspect-ratio less than or greater than $\sqrt{3}$.

In the present study, the electromechanical response of the four classes of piezoelectric honeycomb foam structures are characterized over a range of porosity volume fractions and benchmarked with the properties of a reference foam structure with square-shaped porosity. An overview of the constitutive relations that govern the electromechanical response of piezoelectric materials in the linear elastic domain is given in Section 2.3.

2.3 Constitutive Relations for Piezoelectric Materials

The constitutive relations that govern the behavior of piezoelectric materials in the linear elastic domain as represented (in stress-charge) form is as follows:

$$\sigma_{ij} = \mathrm{C}^E_{ijkl}\varepsilon_{kl} - \mathrm{e}_{kij}E_k \tag{2.1}$$

$$D_k = \mathrm{e}_{kij}\varepsilon_{ij} + \kappa^\varepsilon_{ki}E_i \tag{2.2}$$

where $\boldsymbol{\sigma}$ is the stress tensor, $\boldsymbol{\varepsilon}$ is the strain tensor, $\boldsymbol{E}$ is the electric field vector, $\boldsymbol{D}$ is the electric displacement vector, $\boldsymbol{C^E}$ is the stiffness tensor with the superscript '$\boldsymbol{E}$' indicating that the measurement of the components have been carried out at zero/constant electric field, $\boldsymbol{\kappa^\varepsilon}$ is the permittivity tensor with the superscript '$\boldsymbol{\varepsilon}$' indicating that the components of $\boldsymbol{\kappa}$ have been measured at constant or zero strain, $\boldsymbol{e}$ is the piezoelectric coupling tensor. Following the

representation of Nye [74], Eq. (2.1) and (2.2) can also be written as:

$$\sigma_a = C_{ab}^E \varepsilon_b - e_{kij} E_k \qquad (2.3)$$

$$D_i = e_{ib} \varepsilon_b + \kappa_{ki}^\varepsilon E_k \qquad (2.4)$$

where a and b are derived from ij and kl as follows: for ij or $kl = 11, 22, 33, 23, 13,$ and $12, a$ and b, respectively, correspond to $1, 2, 3, 4, 5,$ and 6. In Eqns. (2.1) and (2.2) i, j, k, l correspond to regular Cartesian coordinates ranging from 1 to 3. Eqns. (2.3) and (2.4) are the most general representation of the constitutive behavior of the piezoelectric materials with 45 independent constants - 21 elastic, and 18 piezoelectric and 6 dielectric (or permittivity) constants. For the complete characterization of the piezoelectric behavior of a material all 45 material constants have to be determined. In order to assess the utility of piezoelectric composites in practical applications, combinations of the fundamental electromechanical properties (i.e., figures of merit) are usually invoked. Some figures of merit that are of direct importance to porous piezoelectric materials and their potential applications (e.g., in hydrophones) are the piezoelectric coupling constant (k_t), the acoustic impedance (Z), the hydrostatic strain coefficient (d_h), and the hydrostatic figure of merit ($d_h g_h$)[25, 24]. The finite element model developed in the present study to characterize the complete electromechanical properties and the corresponding figures of merit of piezoelectric honeycombs is described in Section 2.4.

2.4 Finite-element model for piezoelectric honeycomb foams

The finite-element model developed in the present study uses the basis that the complete electromechanical response of a large periodic piezoelectric foam structure can be captured by characterizing the electromechanical behavior of a representative volume element of the material, i.e., the unit cell. The finite-element analysis of the unit cell is carried out using a commercially available software (ABAQUS). Eight-node linear piezoelectric brick (C3D8E)

12

elements are used to mesh the unit cell. Each node is allowed a total of four degrees of freedom three translational degrees of freedom (i.e., $1, 2, 3$) and one electric potential degree of freedom (i.e., 9). To ensure that the unit cell
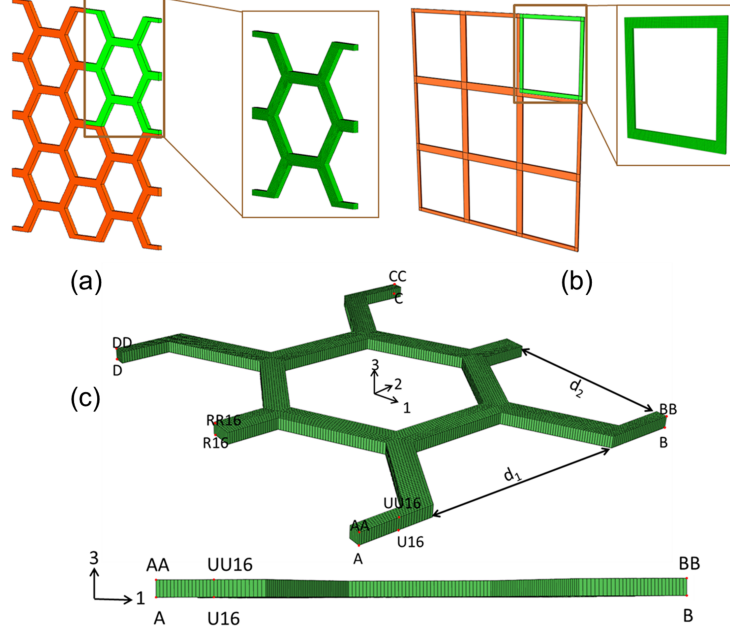
Figure 2.2: (a, b) Schematic illustrating the piezoelectric honeycomb and reference foam structures and their corresponding unit cells. (c, d) The unit-cell finite-element models representing an isotropic honeycomb foam structure with 25% relative density. All isotropic honeycombs regardless of relative density have aspect ratio (d_1/d_2) equal to 1.73. The aspect ratio of the anisotropic honeycomb considered in the present study is ten times that of the regular/isotropic honeycomb. The figures show the master nodes located at the vertices of the unit-cell. R16, RR16, U16, UU16 are shown as examples of the nodes on the boundary that are used to set up the periodic constraint equations (Eqn. (2.5),(2.6)).

captures the response of the entire foam material, certain periodic boundary conditions must be enforced. These conditions make sure that the deformation and electric potential of a unit cell are compatible across its boundaries with that of the adjacent unit cells [25]. Compatibility is ensured by forcing parallel faces of the unit cell to remain parallel during deformation. To facilitate applying the periodic conditions, the honeycomb unit cell is modeled using a periodic mesh that is symmetric in the xy, yz and xz planes. The periodic boundary conditions are achieved by connecting each node on one side (e.g.,

left) with the corresponding node on the opposite side of the unit cell (e.g., right) using constraint equations that are defined with respect to the master nodes, located on the vertices of the unit cell. They are shown in Fig. 2.2 and are referred to as A, AA, B, BB, C, CC, D, and DD. The constraint equations are designed such that they allow the master nodes to control the overall behavior of the unit cell. All loads (mechanical and electrical) are applied to the master nodes only. The master node A is fixed and electrically grounded for all simulations to prevent rigid body motion. The total number of constraint equations is almost half the number of boundary nodes in the model. To write the constraint equations in a compact form, nodes on boundary lines connecting two master nodes are assigned to a node set. Therefore, eight node sets are defined such that: R contains the nodes between A and D; RR contains nodes between AA and DD; S contains nodes between B and C; SS contains nodes between BB and CC; U contains nodes between A and B; UU contains nodes between AA and BB; T contains nodes between C and D; TT contains nodes between CC and DD. In terms of the node sets and master nodes the constraint equations are given as:

$$P_i^R - P^A = P_i^S - P^B; P_i^{RR} - P^{AA} = P_i^{SS} - P^{BB}; \qquad (2.5)$$

$$P_i^T - P^D = P_i^U - P^A; P_i^{TT} - P^{DD} = P_i^{UU} - P^{AA} \qquad (2.6)$$

where"P" refers to the degrees of freedom (i.e., $P = 1, 2, 3$, and 9) and i represents the node in the set (Figure 2.2). By subjecting a particular unit cell to a set of controlled mechanical and electrical loading conditions and studying its response, all 45 corresponding material constants (i.e. complete electroelastic moduli) can be determined. The main feature of this three-dimensional finite element model is that all four types of unit cells that represent the four classes of piezoelectric honeycombs identified in Section 2.2, are subject to a common set of electrical and mechanical loading conditions in order to determine the components of the electroelastic moduli of a given foam structure. For the present study the piezoelectric honeycomb unit-cell is assigned a thickness of one-element in the out-of-plane direction, i.e., 3-direction. This generalized

14

plane-strain approach is valid as we consider 3-1 type foams where the material is considered to be fairly thick along the 3-direction. Furthermore, the electromechanical response of a unit-cell has also been checked to ensure that it accurately represents the electromechanical response of a larger volume of material comprised of many unit-cells. Earlier work by Kar-Gupta and Venkatesh also demonstrated that the generalized plane strain models accurately capture the results of three-dimensional finite element models as well [75, 76].

2.5 Results and Discussions

The finite element model developed in the present study for characterizing the electromechanical properties of honeycomb foams structures is first validated with an analytical model developed earlier to predict the elastic properties of such honeycombs. Upon verifying that the results of the finite element model agree well with the analytical model for elastic properties, the finite element model is extended to predict the structure-electromechanical property relationships in honeycomb foam structures. A model piezoelectric system PZT-7A with a high piezoelectric coefficient d_{33} is chosen for the present study. As the primary focus of the present study is on low-density piezoelectric foams (which are expected to exhibit enhanced hydrostatic figures of merit), foam structures over a limited range of relative densities from 5% to 30% are analyzed. However, the finite element models can be readily extended to characterize the electromechanical properties of high-density foams with relative densities that are greater than 30% as well. The properties for a polycrystal PZT-7A poled in the 3-direction can be found in Table A.1.

2.5.1 Comparison of the numerical model with analytical models for honeycomb foam structures

An analytical model that predicts the complete electromechanical properties of bulk piezoelectric honeycomb structures is at present not available.

By taking into consideration, several deformation mechanisms such as

15

flexure, hinging and stretching, Evans and Masters [1] developed an analytical model for predicting the elastic properties (i.e., the elastic moduli and Poisson's ratios) of honeycomb foam structures made from constituent materials that exhibit elastic isotropy. The accuracy of the finite element model developed in the present study in predicting the properties of the honeycomb structures is assessed by comparing the results of the finite element with those of the analytical model for a model material such as aluminum that exhibits elastic isotropy. Fig. 2.3(a) illustrates that there is indeed very good agreement between the predictions of the finite element model and the analytical model, for the elastic moduli in two directions and the Poisson's ratio.
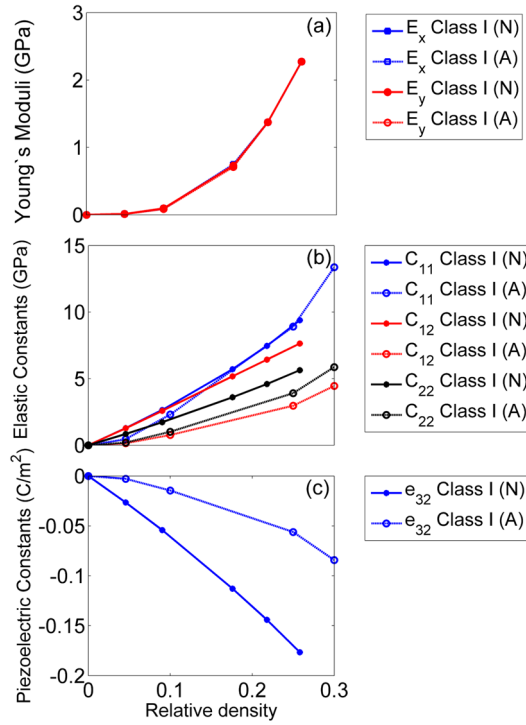
Figure 2.3: Comparison between the predictions of the analytical model (A) by Masters et al. [1] and those of the finite element model (FEM) developed in the present study for the Young's Moduli of an aluminum honeycomb.

An analytical model based on the asymptotic homogenization method was developed by Saha et al. [77] for predicting some of the elastic and piezoelectric constants of Class I type longitudinally porous honeycomb-cored sandwich

shell structures (in the thin-film limit where the out-of-plane thickness is vanishingly small). Figures 2.3(b) and 2.3(c) provide a comparison of the results of analytical model (for thin-film honeycombs) with the results of the finite element model developed in the present study (for bulk honeycombs). It is observed that some of the elastic constants such as C_{11} and C_{22} are reasonably well-predicted by the analytical model as compared to other elastic constants (such as C_{12}) or piezoelectric constant (such as e_{32}) - As the analytical model [77] was developed for thin shell structures, out-of-plane constants such as C_{33} or e_{33} are not predicted by the model. Furthermore, the analytical model [77] also does not provide explicit expressions for dielectric constants of the honeycomb structures.
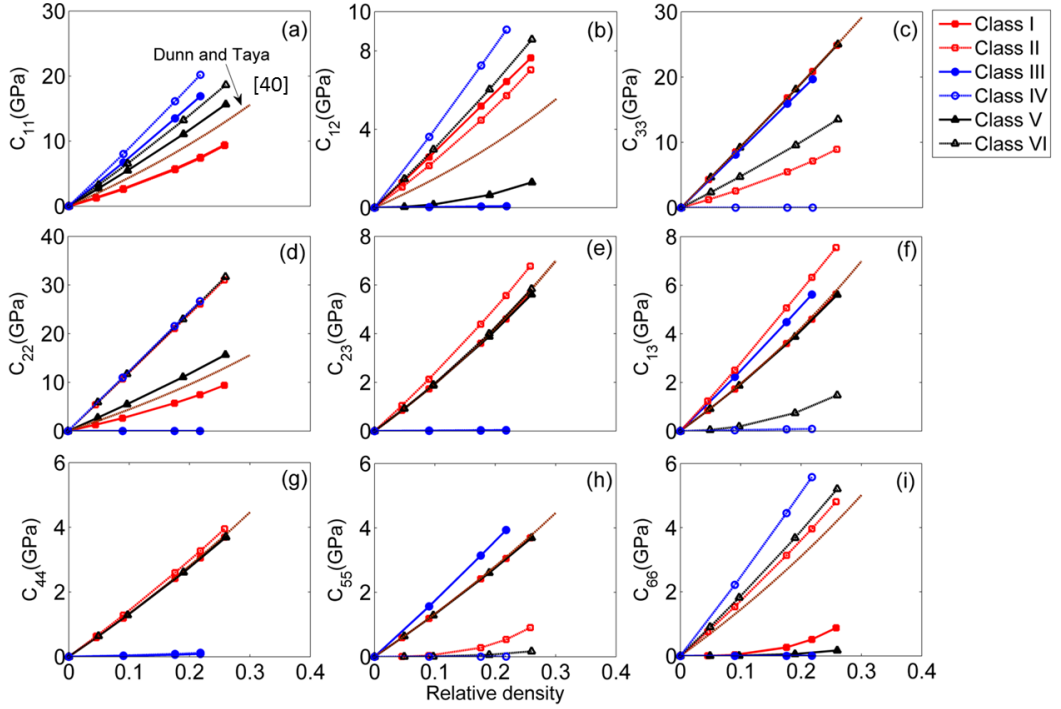
Figure 2.4: Variation of the overall elastic constants with relative density in several classes of piezoelectric honeycomb foam structures.

The results of the finite element model developed in the present study for bulk honeycomb structures are also compared to the predictions of an analytical model that was developed by Dunn and Taya [48] for a bulk piezoelectric

17

system with cylindrical porosity, as both the honeycomb structures and the cylindrically porous structures exhibit 3-1 type connectivity. As observed in Figs. 2.4 and 2.5, the principal material constants in the out-of-plane (i.e., 3) direction (i.e., C_{33}, κ_{33} and e_{33}), predicted by the finite element model for Class I type hexagonal-shaped honeycomb foams agree well with the predictions of the analytical model for cylindrically porous structures. This is expected as the out-of-plane properties of piezoelectric foams (and long-fiber composites) are not influenced significantly by the shape of the porosity (or fibers). However, the in-plane and other shear constants (such as C_{11}, C_{12} or C_{13}) are expected to demonstrate strong dependence on the microstructure and the shape of the foam structures. Hence, the finite element model is expected to capture the in-plane and shear properties more accurately than the analytical model [48].

2.5.2 Electromechanical properties of piezoelectric honeycomb foam structures

Figs. 2.4-2.5 present the elastic, dielectric and piezoelectric properties of longitudinally porous and transversely porous honeycomb structures over a range of relative densities.

2.5.2.1 Longitudinally porous honeycomb foam structures

Most of the elastic, dielectric and piezoelectric constants of the longitudinally porous honeycomb foams (with the exception of the in-plane elastic constants, C_{12} and C_{66}) exhibit linear dependence on the volume fraction (or relative density) of the material. However, it should be noted that this observation may not hold when the porosity is not aligned with the poling direction. Most of the electromechanical properties of the longitudinally porous honeycombs (with hexagonal shaped porosity) are similar to that of the reference foam structure with square-shape porosity. The piezoelectric honeycombs exhibit significantly enhanced in-plane elastic constants C_{12} and C_{66} as compared to the foams with square shaped porosity while the foams with the square shaped porosity exhibit significantly enhanced in-plane elastic properties such as C_{11}

and C_{22}.
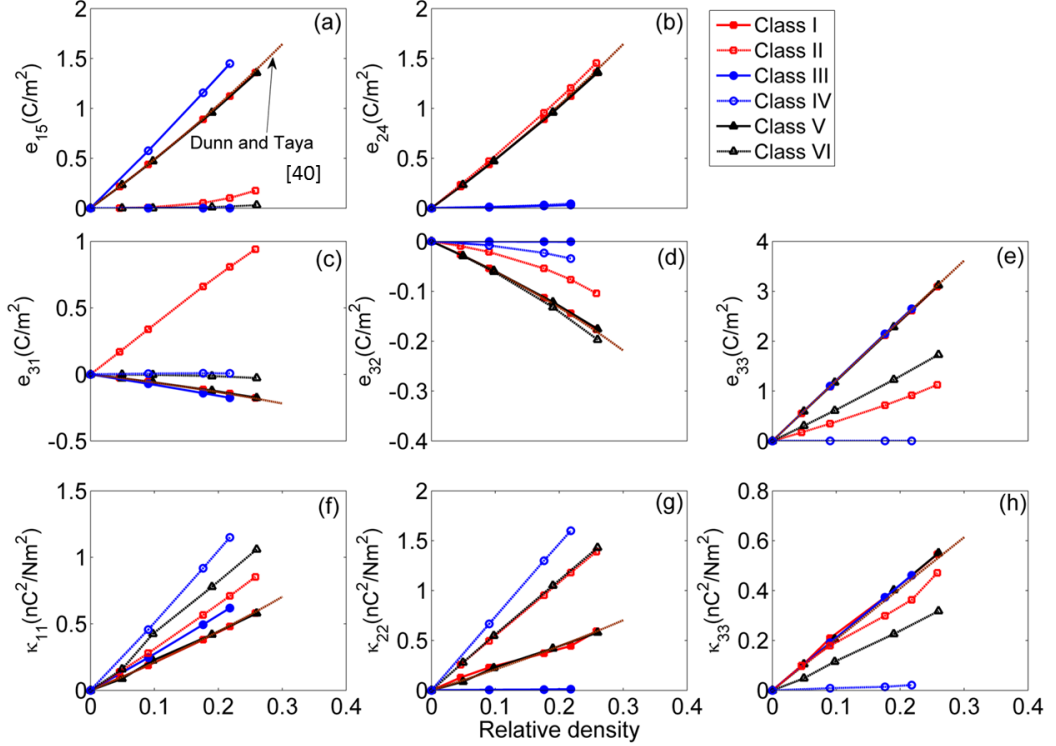
Figure 2.5: Variation of the overall piezoelectric and dielectric constants with relative density in several classes of piezoelectric honeycomb foam structures.

Amongst the normal material constants, the properties in the "longitudinal" direction (such as C_{33}, e_{33}, κ_{33}) of the honeycomb structures are generally observed to be higher than the in-plane constants (such as C_{11} or C_{22}). This observation can be explained on the basis that the dominant deformation mode in the out-of-plane (3-direction) is axial while the deformation mode in the in-plane directions (1 or 2-direction) is bending/hinging. However, amongst the elastic material constants, the properties in the out-of-plane "transverse" direction (i.e., C_{13}, C_{23}) are observed to show greater compliance than the in-plane constant C_{12}. This observation can be attributed to the fact that honeycomb architecture results in an out-of-plane Poisson's ratio that is at least an order of magnitude smaller than the in-plane Poisson's ratio. For example, for the case with a relative density of 15%, the in-plane Poisson's ratio

19

ν_{12} is 0.9 while the out-of-plane Poisson's ratios ν_{13} and ν_{23} are 0.02 and 0.006, respectively. Therefore, for example, the normal stress in the 1-direction due to normal strain in the 2- direction, which is governed by C_{12}, is larger than the normal stress in the 3-direction due to normal strain in the 2- direction, which is governed by C_{32}.

The shear constants involving the out of plane direction (i.e., C_{44}, C_{55}) show a linear dependence on increasing relative density of the foam material. This linear trend is mostly due to the dominance of the axial loading in the 3-direction which also makes the foam stiffer under out-of-plane shear loading condition. The corresponding in-plane shear constants, C_{66}, was observed to show a non-linear trend with respect to increasing volume fraction which is expected as the dominant mode of deformation is bending in the struts and ligaments of the foam structures along the 1- and 2-directions.
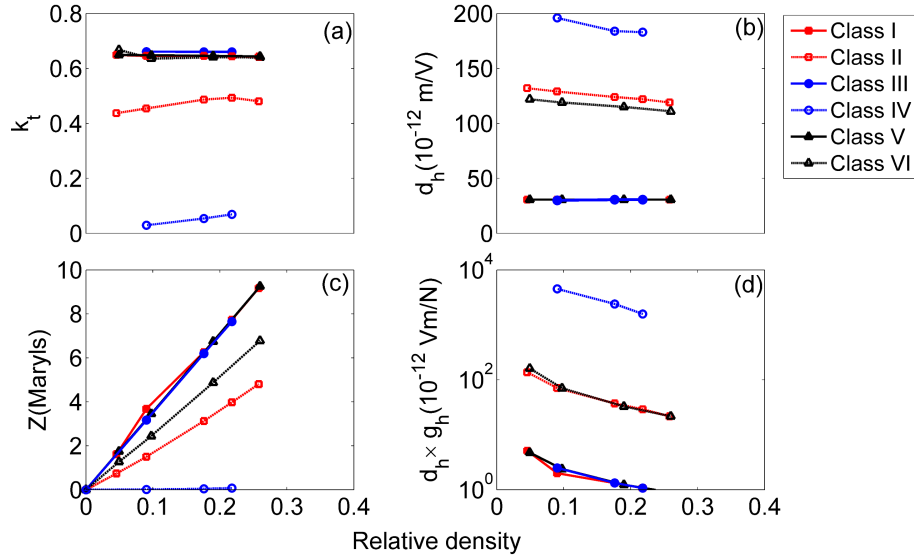
Figure 2.6: Variation of select figures of merit with relative density in several classes of honeycomb foam structures.

The piezoelectric figures of merit of the longitudinally porous foams do not exhibit significant dependence on the shape of the porosity with the piezo-electric coupling constant, acoustic impedance, hydrostatic strain coefficient and the hydrostatic figure of merit of the hexagonal honeycombs being similar

to that of the square foams (Fig. 2.6).

2.5.2.2 Transversely porous honeycomb foam structures

Unlike the trends observed in the case of longitudinally porous foam structures, the electromechanical properties of transversely porous foam structures (with the exception of C_{22} and κ_{22}) exhibit significant dependence on the shape of the porosity. Select elastic, dielectric and piezoelectric constants such as $C_{13}, C_{23}, C_{44}, C_{55}, \kappa_{33}, e_{15}$ and e_{31} of the honeycombs are higher than that of the square-shaped foams while select electroelastic moduli such as $C_{11}, C_{12}, C_{33}, C_{66}, \kappa_{11}, e_{32}$ and e_{33} are higher for the foams with square-shaped porosity (Fig. 2.5). Interestingly, the 'honeycomb architecture' results in the piezoelectric constant e_{31} being significantly enhanced for the honeycomb foam structure as compared to the foam structure with square-shaped porosity (Fig. 2.5).

The piezoelectric figures of merit of the transversely porous foams also exhibit a strong dependence on the shape of the porosity, with the hexagonal foams exhibiting enhanced hydrostatic strain coefficient and lower acoustic impedance while the square foams exhibiting enhanced piezoelectric coupling constant and hydrostatic figure of merit (Fig. 2.6).

In transversely porous anisotropic honeycomb structures (with aspect-ratio less than $\sqrt{3}$), the in-plane elastic properties such as C_{12} and C_{66} are increased significantly when compared to their isotropic counterparts. The piezoelectric coupling constant and the acoustic impedance are reduced, while the hydrostatic strain coefficient and the hydrostatic figure of merit are enhanced significantly. For example, in the PZT-7A transversely porous anisotropic honeycomb structures with 10% relative density, the hydrostatic figure of merit is 2485% greater than that observed for the transversely porous isotropic honeycomb structures. When compared to the reference foam structure (with 10% relative density) which is longitudinally poled with square porosity (i.e., Class V structure), C_{12}, C_{66}, and the hydrostatic figure of merit of the transversely poled anisotropic honeycomb structures (which belong to Class IV) are enhanced by, respectively, 800%, 1100% and 53000%. Thus, it is possible to
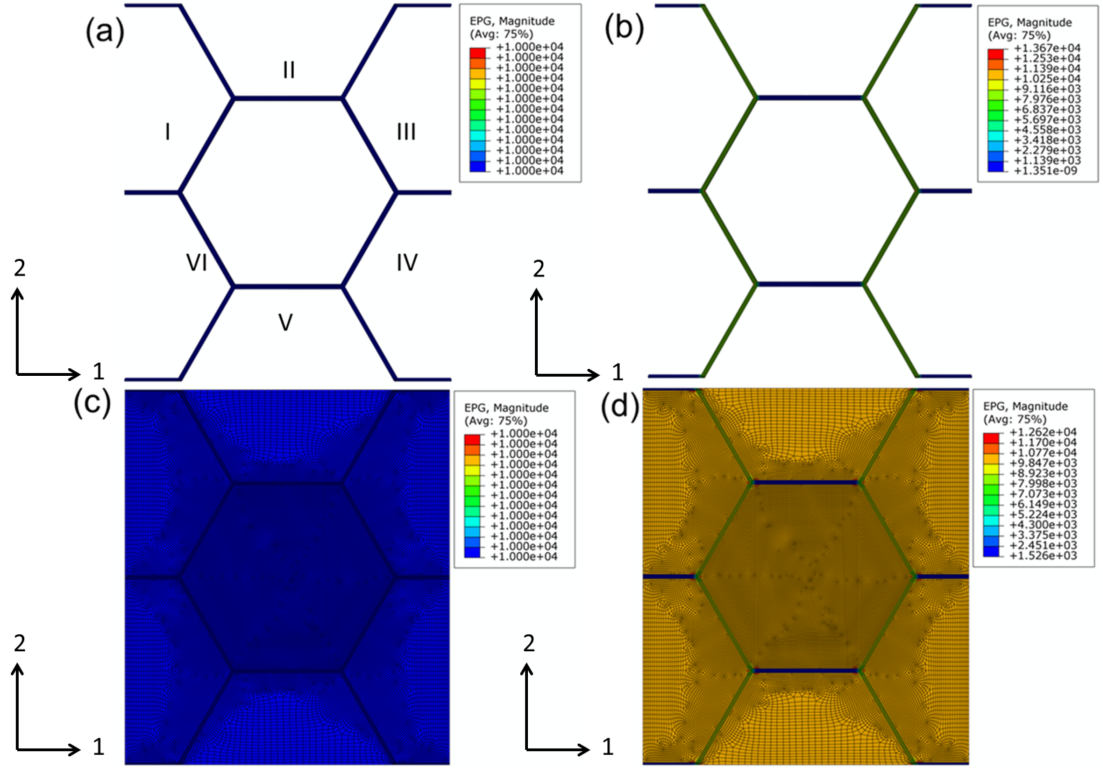
Figure 2.7: The spatial variation in electric fields developed in an unpoled piezoelectric honeycomb structure in response to an external electric field applied along the out-of-plane (i.e., three) direction (a) and in-plane (i.e., two) direction (b). The spatial variation in electric fields developed in an unpoled piezoelectric honeycomb structure filled with a second-phase material in response to an external electric field applied along the out of- plane (i.e., three) direction (c) and in-plane (i.e., two) direction (d).

create piezoelectric honeycomb structures with the desirable combination of mechanical properties and piezoelectric characteristics.

As the finite element model used in the study of porous piezoelectric composite enables the determination of 45 independent electromechanical constants, the crystal symmetry of the honeycomb foam structures can be identified as well. In the model system consisting of fully dense PZT-7A, higher order crystal symmetry (i.e., $6mm$) is observed. In the longitudinally porous isotropic honeycomb structures, the same higher order crystal symmetry is maintained. However, in the transversely porous honeycomb structures, the crystal symmetry is reduced to the group ($mm2$).

Overall, by tailoring the shape of the honeycomb foam structures the mechanical and piezoelectric properties of the piezoelectric materials can be optimized as required in practical applications.

In Fig. 2.7(a) and Fig. 2.7(c), the externally applied electric field along the three direction is 10 kV/mm and the internally developed electric fields are also 10 kV/mm. In Fig. 2.7(b) and Fig. 2.7(d), the externally applied electric field along the two directions is 10 kV/mm. In Fig. 2.7(b), the internally developed electric fields in regions I, III, IV, and VI are about 6 kV/mm, whereas regions II and V experience electric fields of about 0.15 kV/mm. In Fig. 2.7(d), the internally developed electric fields in regions I, III, IV, and VI are about 6 kV/mm, whereas regions II and V experience electric fields of about 2 kV/mm. The dielectric constant of the filler material in Fig. 2.7(b) and Fig. 2.7(d) is about 1/10th of that of the honeycomb material (i.e., PZT-7A). In the finite element models developed in this study, it is assumed that all regions in the piezoelectric foams are poled uniformly in one direction. From a practical point of view, such uniform poling can be readily realized in longitudinally porous honeycombs as uniform electric fields in the out-of-plane (i.e., 3) direction can be easily created in such honeycombs (Fig. 2.7(a)(c)). However, poling transversely porous piezoelectric honeycombs in a uniform manner could be challenging as finite element simulations of the poling process indicate that the electric fields developed in the in-plane direction, in un-poled honeycombs, are not uniform in all regions of the honeycombs. Thus, some regions may remain un-poled or be poled in a direction that is different from the direction that is originally intended in the poling process (Fig. 2.7(b)). However, if the porous regions were to be filled by a material with an elastic modulus and dielectric constant that is considerably lower than that of the honeycomb (e.g., a polymer), then significant improvements in the uniformity of the poling characteristics across a wider region of the foams could be achieved as uniform electric fields are created in most of the honeycombs during the poling process (Fig. 2.7(d)). (Alternately, a poled, solid piezoelectric material may, in principle, be selectively treated (i.e., laser machined or chemically etched) such that the inner regions of the honeycombs

are removed while retaining the honeycomb network to create a uniformly poled foam structure as well).

The important conclusions drawn from the present study of piezoelectric honeycombs are highlighted in the following section.

2.6   Conclusions

Passive honeycomb type foam structures with their unique and tailorable microstructural and topological features have already been proven to provide enhanced stiffness to out of plane shear deformations. Active piezoelectric foam materials (which have internal architectures that are different from the honeycombs) have been demonstrated to exhibit piezoelectric properties that are useful for several device applications. However, it is unclear whether active honeycomb foams with a desirable combination of mechanical properties and piezoelectric properties can be developed. Hence, the present study was focused on establishing the relationships between the microstructural features of the piezoelectric honeycomb structures and their effective properties over a range of relative densities, and the following principal conclusions were obtained.

1. A three-dimensional finite element model was developed to characterize the complete electromechanical properties of the most general form of elastically anisotropic piezoelectrically active foams with honeycomb structures.

2. Depending on the relative orientation of the poling direction with the porosity direction (Longitudinal and Transverse) and the geometry of the honeycombs (Isotropic and Anisotropic), four classes of piezoelectric honeycomb foam structures were identified.

3. Most of the elastic, dielectric and piezoelectric constants of the longitudinally porous honeycomb foams (with the exception of the in-plane elastic constants, C_{12} and C_{66}) exhibit linear dependence on the volume fraction (or relative density) of the material. Furthermore, most of the

electromechanical properties of the longitudinally porous honeycombs (with hexagonal shaped porosity) are similar to that of the reference foam structure with square-shape porosity.

4. Unlike the trends observed in the case of longitudinally porous foam structures, the electromechanical properties of transversely porous foam structures (with the exception of C_{22} and κ_{22}) exhibit significant dependence on the shape of the porosity.

5. The piezoelectric figures of merit of the longitudinally porous foams do not exhibit significant dependence on the shape of the porosity with the piezoelectric coupling constant, acoustic impedance, hydrostatic strain coefficient and the hydrostatic figure of merit of the hexagonal honeycombs being similar to that of the square foams.

6. The piezoelectric figures of merit of the transversely porous foams also exhibit a strong dependence on the shape of the porosity with the hexagonal foams exhibiting enhanced hydrostatic strain coefficient and lower acoustic impedance while the square foams exhibiting enhanced piezoelectric coupling constant and hydrostatic figure of merit.

7. In transversely porous anisotropic honeycomb structures (with aspect-ratio less than $\sqrt{3}$), the in-plane elastic properties such as C_{12} and C_{66} are increased significantly when compared to their isotropic counterparts. The piezoelectric coupling constant and the acoustic impedance are reduced, while the hydrostatic strain coefficient and the hydrostatic figure of merit are enhanced significantly. For example, in the PZT-7A transversely porous anisotropic honeycomb structures with 10% relative density, the hydrostatic figure of merit is 2485% greater than that observed for the transversely porous isotropic honeycomb structures. Thus, it is possible to create piezoelectric honeycomb structures with the desirable combination of enhanced mechanical properties and enhanced piezoelectric characteristics.

CHAPTER 3

On The Relationships Between Cellular Structure, Deformation Modes and Electromechanical Properties of Piezoelectric Cellular Solids

3.1 Outline of the chapter

Due to their underlying cellular architecture, all piezoelectric active foams are fundamentally similar to structural cellular solids, which have been extensively studied in both forms - stochastic [8, 9](i.e., foams) and periodic [10, 11, 12, 13] (e.g. honeycombs and lattice-based architectures), and have been adopted by a wide range of industries such as automotive (e.g. [14, 15, 16]), aerospace (e.g. [3]) and naval. The underlying similarities between active and structural foams render many of the observations and governing laws associated with structural foams, which preceded active foams by decades, readily applicable to active foams. Accordingly, based on the extensive research performed on the topology-property coupling in structural foams, it can be anticipated that the electromechanical properties of piezoelectric active foams are strongly coupled to their cellular topology and morphology. This coupling is recognized as a consequence of cellular ligaments acting as networks with preferred or admissible deformation modes and mechanisms [10, 11, 12, 13, 8].

Different cellular architectures exhibit different deformation modes and macroscopic properties. The existence of topology-property coupling on one hand highlights the need for reaching a better understanding of the effect of the different topological parameters on the electromechanical response of

piezoelectric foams. More importantly, understanding this coupling is instrumental to the development of optimized or application tailored piezoelectric cellular solids.

Understanding the topology-property coupling is also motivated by the forthcoming capabilities of the rapidly progressing additive manufacturing processes such as solid freeform fabrication, rapid prototyping and 3D printing. These techniques will open horizons for piezoelectric cellular solids as they will provide the possibility to fabricate parts of any arbitrary material composition and internal microarchitecture at the mesoscopic length scale. Hence, one can envision a stage at which piezoelectric cellular solids can be designed to provide a wide range of electromechanical properties that can be controlled by the cellular architecture.

The level of enhancement and the scaling laws governing the electromechanical properties for stretching dominated piezoelectric foams have not been established yet. This work aims to provide answers in this regard by quantifying the enhancement in the electromechanical properties and establishing the scaling laws associated with piezoelectric active foams that have a stretching dominated deformation mode.

In this paper, we utilize finite element analysis to characterize the effect of deformation modes (bending vs. stretching) on the complete electromechanical properties of piezoelectric active foams by studying piezoelectric foams with varying cellular architectures, representative of foams with bending and stretching dominant deformation modes. Also, this work explores the relationships between the microstructural features of piezoelectric foams and the dominant modes of deformation. The present work has been organized as follows. Section 3.2 illustrates the methodology utilized and discusses the details of the developed finite element models. Results are discussed in Section 3.3 and principal conclusions from the present study are highlighted in Section 3.4.

3.2 Methodology

3.2.1 Specimens: geometry, cellular features

Three classes of piezoelectric cellular solids are considered in Fig. (3.1). These have been selected to represent foams with low, moderate and high nodal connectivity, which can exhibit bending-dominated, mixed-mode, or stretching-dominated deformation characteristics, depending on the loading conditions. Nodal connectivity, α, is defined as the average number of ligaments connected at a node (or vertex). The low connectivity class is represented by a hexagonal honeycomb structure ($\alpha = 3$) while the moderate connectivity class is represented by tetragonal structure ($\alpha = 4$), and the high connectivity class is represented by triangular structure ($\alpha = 6$).

From literature for passive cellular solids, we infer that, low connectivity honeycombs generally deform in a bending mode under in-plane normal and shear loading conditions, while highly connected cellular structures, (with a connectivity of 6 in 2D), generally deform in a stretching mode under all loading conditions [53, 54, 59]. The tetragonal structures deform in a mixed-mode depending on the in-plane loading direction; when the load is aligned with ligaments it deforms in a stretching mode but when the load is not aligned with cellular ligaments (and for in-plane shear loading) tetragonal structures deform in a bending deformation mode. Therefore, one can consider the three selected classes as representatives of cellular solids that exhibit different deformation modes, which will permit the investigation of the effect of foam structure (topology) and deformation modes on the effective electromechanical properties of piezoelectric foams.

A model piezoelectric constituent material, PZT-7A, is chosen for the present study. The electromechanical properties of PZT-7A are presented in Table 3.1. The three cellular classes considered in the present work have relative densities ranging from 5% to 20%. In each of the three classes of cellular materials, longitudinally poled (i.e. poled along the porosity axis) and transversely poled (i.e. poled orthogonal to the porosity axis) systems are considered. The three cellular classes have the same relative density range (5%
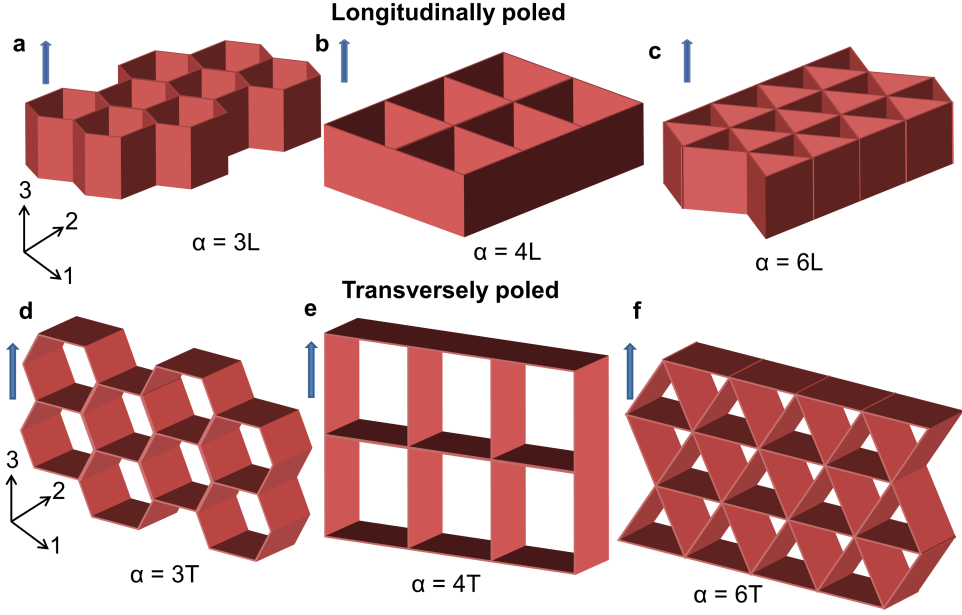
Figure 3.1: A schematic showing the structures studied in the present work. The structures represent a honeycomb, square and triangular unit-cell configurations with the relative direction of poling (blue arrow). The direction of the porosity being aligned with the 3-direction for the case of longitudinally poled structures and the 2-direction for transversely poled structures.

to 20%) and constituent material, which is PZT-7A. The electromechanical properties of PZT-7A are presented in Table 3.1. All specimens are poled in the transverse direction, perpendicular to the porosity direction.

3.2.2 Constitutive Behaviour of Piezoelectric Cellular Solids

The most general representation of the electromechanical coupled constitutive relationships for a piezoelectric material, in the linear regime, is given by:

$$\sigma_{ij} = \mathrm{C}^E_{ijkl}\varepsilon_{kl} - \mathrm{e}_{kij}E_k \tag{3.1}$$

$$D_k = \mathrm{e}_{kij}\varepsilon_{ij} + \kappa^\varepsilon_{ki}E_i \tag{3.2}$$

The terms have been previously explained in detail in Section 2.3 but for sake of completeness will be re-iterated here - $\boldsymbol{\sigma}$ is the stress tensor, $\boldsymbol{\varepsilon}$ is the

Table 3.1: The fundamental properties of the model piezoelectric system PZT-7A (poled in the 2-direction) chosen for the present study ($\rho = 7700\ kg/m^3$).

Properties	PZT-7A
$C_{11} = C_{22}(GPa)$	148
$C_{12}(GPa)$	74.2
$C_{13} = C_{23}(GPa)$	76.2
C_{33}	131
$C_{44} = C_{55}(GPa)$	25.3
$C_{66}(GPa)$	35.9
$e_{15} = e_{23}(C/m^2)$	9.31
$e_{31} = e_{32}(C/m^2)$	-2.324
$e_{33}(C/m^2)$	10.9
$\kappa_{11} = \kappa_{22}(nC/Vm)$	3.98
$\kappa_{33}(nC/Vm)$	2.081

strain tensor, $\boldsymbol{E}$ is the electric field vector, $\boldsymbol{D}$ is the electric displacement vector, $\boldsymbol{C^E}$ is the stiffness tensor with the superscript '$\boldsymbol{E}$' indicating that the measurement of the components have been carried out at zero/constant electric field, $\boldsymbol{\kappa^\varepsilon}$ is the permittivity tensor with the superscript '$\boldsymbol{\varepsilon}$' indicating that the components of $\boldsymbol{\kappa}$ have been measured at constant or zero strain, $\boldsymbol{e}$ is the piezoelectric coupling tensor.

3.2.3 Finite Element Modeling of Piezoelectric Cellular Solids

Unit-cell approach is utilized in this work; where in the complete electromechanical response of large periodic piezoelectric foam structure is characterized by modeling the electromechanical behavior of a representative volume element. The finite element analysis of the unit cell is carried out using commercially available software (ABAQUS). Eight-node linear piezoelectric brick (C3D8E) elements are used to mesh the unit cell. Each node is allowed a total of four degrees of freedom three translational degrees of freedom (i.e., 1, 2, 3) and one electric potential degree of freedom (i.e., 9 per ABAQUS convention). To ensure that the unit cell captures the response of the entire foam material, periodic boundary conditions are enforced. These conditions ensure that the deformation and electric potential of a unit cell are compatible across
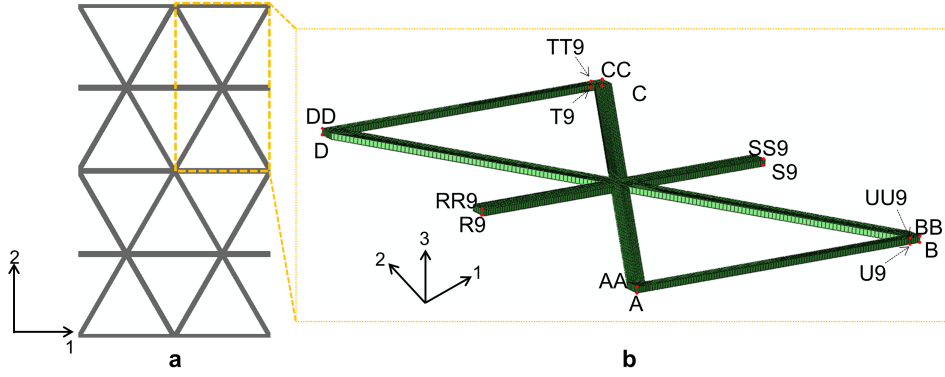
Figure 3.2: (a) A schematic showing the triangular structure studied in the present work. (b) Highlighted unit-cell showing the masters nodes and nodes from the sets R, RR, S, SS, T, TT, U, UU located along the boundaries of the unit-cell. .

its boundaries with that of the adjacent unit cells as explained in [25, 24]. Periodicity is ensured by forcing parallel faces of the unit cell to remain parallel during deformation. To facilitate applying the periodic conditions, the unit cell is modeled using a periodic mesh that is symmetric in the 1-2, 2-3 and 1-3 planes. The periodic boundary conditions are achieved by connecting each node on one side (e.g., left) with the corresponding node on the opposite side of the unit cell (e.g., right) using constraint equations that are defined with respect to master nodes. Master nodes are located on the vertices of the unit cell. They are shown in Fig. 3.2 and are referred to as $A, AA, B, BB, C, CC, D,$ and DD. Although Fig. 3.2 represents the triangular geometry the process followed to set up the period boundary conditions applies for all geometries. The constraint equations are designed such that they allow the master nodes to control the overall behavior of the unit cell. All loads (mechanical and electrical) are applied to the master nodes only. The master node A is fixed and electrically grounded for all simulations to prevent rigid body motion. The constraint equations used in the model are given in Eqs. (2.5) and (2.6).

3.2.4 Effective elastic properties

Using finite element analysis, for each of the three piezoelectric classes considered (see Fig. 3.1), the effective elastic constants represented by C_{ijkl}^{E} in Eqn.
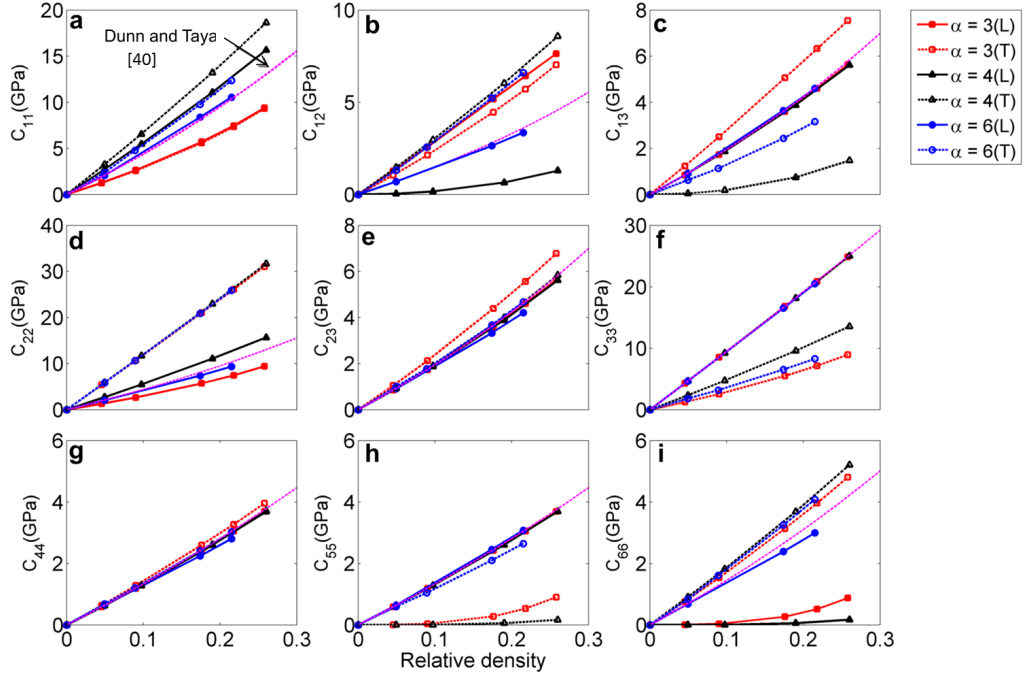
Figure 3.3: Variation of the overall stiffness elastic constants with relative density for the three model unit-cells used in the present study with $\alpha = 3, 4, 6$ denoting the triangular, square and honeycomb unit-cells respectively.

(3.1), the engineering elastic moduli (E) and Poissons ratios were obtained. Effective constants were obtained for a range of relative densities (Fig. 3.4,3.3) as well as for longitudinally poled and transversely poled systems.

The finite element results for the longitudinally poled hexagonal structures were first validated using an analytical model developed for longitudinally poled foams with circular porosity [40] (which structurally resemble the hexagonal-shaped foams considered in this work). For the longitudinally poled systems, it is demonstrated that all the three foam structures exhibit similar out-of-plane (i.e. 3-direction) behaviour. This outcome is anticipated as, regardless of foam structure (or topology), the three cellular architectures have the same projected area density, and in an out-of-plane loading scenario, the cell walls are loaded axially. However, Fig. 3.4 illustrates that the in-plane (i.e. 1-2 plane) behavior is highly sensitive to foam topology and connectivity. For instance, normal effective moduli (C_{11} and C_{22}) are the lowest for the honeycomb structure and the highest for the tetragonal structure (whose
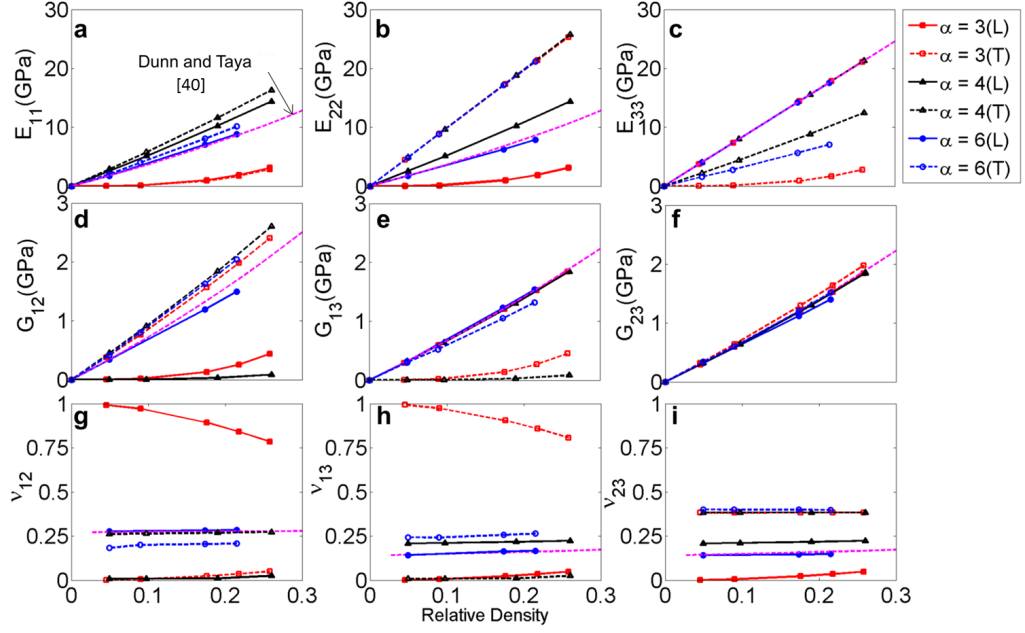
Figure 3.4: Variation of the overall engineering elastic constants with relative density for the three model unit-cells used in the present study with $\alpha = 3, 4, 6$ denoting the triangular, square and honeycomb unit-cells respectively.

ligaments, for the particular loading scenario used in this study, are aligned with loading direction). C_{11} and C_{22} for the triangular structure approach those of tetragonal structure. Coupling modulus C_{12} that defines developed stresses along the lateral direction (i.e. 2-direction) due to axial strain (i.e. 1-direction) is highest for the honeycomb structure and the lowest for the tetragonal structure. This modulus is related to the Poissons ratio which is sensitive to topology, particularly to inclined ligaments that couple the two material principal directions. The most sensitive elastic property to foam topology is the in-plane shear modulus (C_{66}), which is significantly higher for the triangular structures as compared to that of both hexagonal and tetragonal structures (Fig. 3.4).

3.3   Results

However, for the transversely poled systems, the normal elastic modulus along the 2-direction is the least sensitive to the foam topology as the three structures

have the same projected area density along the 2-direction and upon loading along the 2-direction the cell walls of all the three structures are loaded axially. On the other hand, the shear modulus in the 1-3 plane (i.e. C_{55}) is the most sensitive to the foam topology with the foam structure with the highest nodal connectivity (i.e. the triangular structure) exhibiting the highest C_{55} modulus.

Overall, Fig. 3.4 illustrates that the effective out-of-plane elastic properties (i.e. along 3-direction for longitudinally poled systems and along the 2-direction for transversely poled systems), for all the three foam structures, are insensitive to the geometry of the foam and depend linearly on relative density. On the other hand, the dependence of the in-plane effective elastic properties (i.e. in the 1-2 plane for longitudinally poled systems and in the 1-3 plane for transversely poled systems) on relative density exhibit dependence on the foam structure. Such that, this dependence is linear for triangular and tetragonal foam structures (where the deformation is stretching dominated) and generally non-linear for hexagonal honeycombs (where the deformation is bending dominated). This observation is consistent with passive cellular solids literature, which illustrates that for a stretching- or bending-dominated deformation, the corresponding elastic properties, respectively, vary linearly or non-linearly with relative density.

3.3.1   Effective piezoelectric properties

Using finite element models, the effective piezoelectric constants represented by e_{kij} in Eq. (3.1) were computed for the three classes of foam structures shown in Fig. 3.1, for a range of relative densities Fig. 3.5. For each of the three foam classes, the corresponding piezoelectric properties of longitudinally poled and transversely poled systems were also obtained. For the foams considered, the non-zero effective piezoelectric properties are $e_{15}, e_{24}, e_{33}, e_{31}$ and e_{32}. In general, the piezoelectric properties of longitudinally poled foam structures are independent of the foam structure or topology (Fig. 3.1). However, significant dependence of the piezoelectric properties on the foam topology is observed in the transversely poled foams.

34
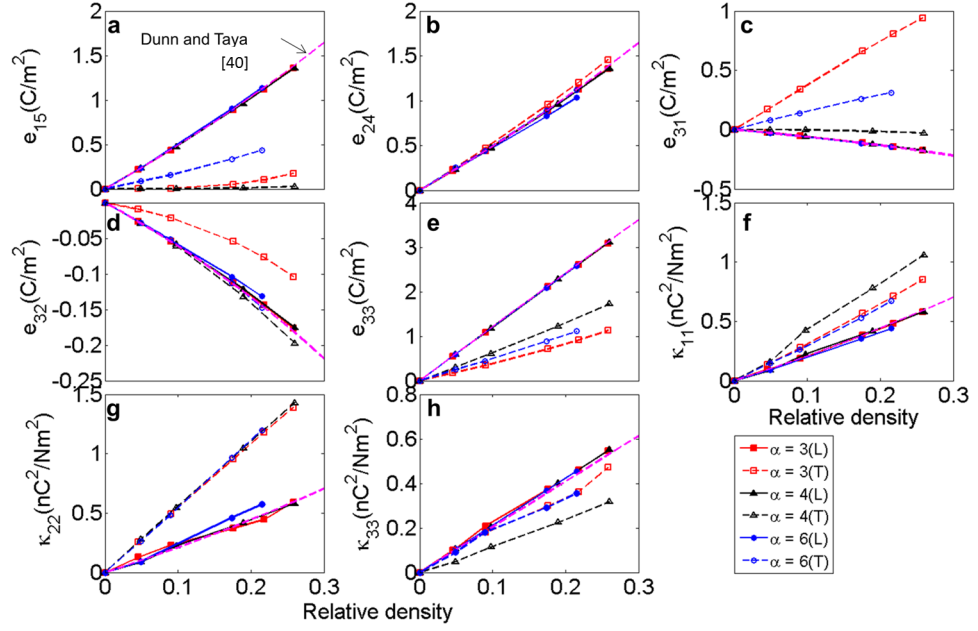
Figure 3.5: Variation of the overall piezoelectric constants with relative density for the three foam structures studied in the present work with $\alpha = 3, 4, 6$ denoting the triangular, square and honeycomb structures respectively.

With respect to the variation of effective piezo properties with relative density, the triangular and tetragonal topologies exhibit generally linear dependence, while the hexagonal topology exhibits non-linear dependence. This non-linear dependence is associated with shear/bending deformation related piezoelectric properties.

Amongst the transversely poled structures, the highest and the lowest e_{33} and e_{32} piezoelectric constants are observed, respectively, in the case of tetragonal and hexagonal foam structures. On the other hand, the piezoelectric constant e_{31} is highest for the hexagonal structure and lowest for the tetragonal structure while the piezoelectric constant e_{15} is highest for the triangular structure and lowest for the tetragonal structure. Thus, foam structure or topology can be tailored to optimize a set of piezoelectric constants that are desired for a particular application.

35

3.3.2 Effective dielectric properties

The effective piezoelectric constants represented by κ^ε_{ij} in Eqn. (3.2) were obtained for the three foams shown in Fig. 3.1 for a range of relative densities (Fig 3.5) for longitudinally poled and transversely poled systems. In general, the dielectric constants - κ_{11}, κ_{22}, and κ_{22}, of longitudinally poled foams and the dielectric constant κ_{22} of the transversely poled foam structures are independent of the foam structure or topology (Fig. 3.5). However, the dielectric constants - κ_{11} and κ_{33} of the transversely poled foam structures exhibit significant dependence on foam topology. Amongst the transversely poled structures, the tetragonal foams exhibit the highest κ_{11} and the lowest κ_{33} dielectric constants while the triangular and honeycomb foams exhibit relatively similar effective dielectric properties that are 10% off those exhibited by tetragonal foams.

3.3.3 Effective Figures of merits

The aforementioned fundamental materials constants are represented in this section via the industry adopted figures of merit. These figures are defined as combinations of the fundamental material constants and are used widely to assess the utility of piezoelectric materials for practical applications. Four figures of merit are of direct interest to piezoelectric foams and their potential applications (e.g., ultrasound images and energy harvesters), and they are: the piezoelectric charge coefficient (d_h), the hydrostatic figure of merit ($d_h g_h$), the acoustic impedance (Z), and the coupling constant (k_t) [75].

Piezoelectric charge coefficient: The piezoelectric charge coefficient ($d_h = d_{31} + d_{32} + d_{33}$), captures the effective strength of electro-mechanical coupling in a piezoelectric material, especially, in the conversion of mechanical loads to electrical signals.

Hydrostatic figure of merit: In general, an important design consideration for transducers is the signal-to-noise ratio which is determined by the spectral noise pressure. In order to enhance the signal-to-noise ratio, the spectral noise pressure must be minimized, for which the hydrostatic figure of merit ($d_h g_h$)
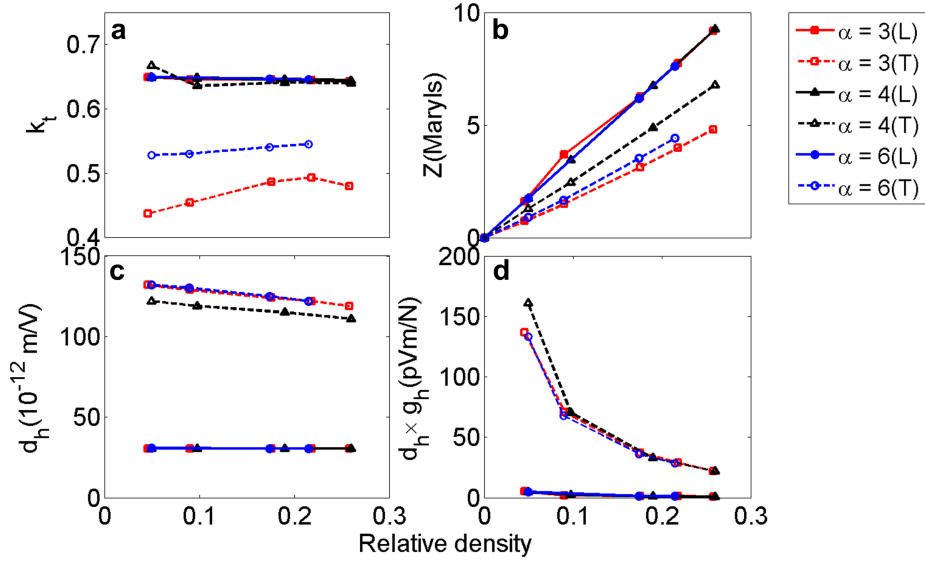
Figure 3.6: Variation of the overall piezoelectric figures of merit with relative density for the three foam structures studied in the present work with $\alpha = 3, 4, 6$ denoting the triangular, square and honeycomb unit-cells respectively.

should be maximized.

Acoustic impedance: The acoustic impedance, (defined as $Z = \sqrt{\rho C_{33}^D}$, when 3 is the poling direction), modulates the extent of signal transmission or reflection at the piezoelectric device/environment interface, where ρ is the density of the material.

Piezoelectric thickness coupling constant: The piezoelectric thickness coupling constant, which for a material poled along the 3-direction is defined as, $k_t = \sqrt{C_{33}^E/C_{33}^D}$. It represents the efficiency of energy conversion between the electrical and mechanical domains, with systems exhibiting larger coupling constants (ideally ~ 1) being more desirable [78].

The effective fundamental material constants (elastic, piezoelectric and dielectric) presented in Figs. 3.4 and 3.5 were used to compute the figures of merit defined above with the results plotted in Fig. 3.6 against relative density. In general, the figures of merit of longitudinally poled foam structures are independent of the foam structure or topology (Fig. 3.6). However, significant dependence of the figures of merit on the foam topology is observed in the transversely poled foams which is expected, as the figures of merit are

37

mostly dependent on the principal material elastic, piezoelectric and dielectric constants (i.e. C_{33}, e_{33} and κ_{33}) which have been shown to exhibit sensitivity to the foam topology (in the transversely poled foams). Amongst the longitudinally poled systems, the triangular structures with $\alpha = 6$, exhibit figures of merit which are similar to other foam structures as well as outstanding in-plane shear properties which are significantly better than those of the tetragonal or hexagonal foam structures.

Overall, the transversely poled systems exhibit better figures of merit (Z, d_h and $d_h g_h$) than the longitudinally poled systems. Amongst the transversely poled systems, the tetragonal structure with a moderate level of nodal connectivity of 4, exhibits the best overall combination of high piezoelectric coupling constant, piezoelectric charge coefficient and the hydrostatic figure of merit with marginally higher acoustic impedance as compared to that of the hexagonal or triangular foams. Thus, by modifying the foam structure and the poling characteristics of piezoelectric foams, their mechanical and functional properties can be application tailored and optimized.

3.3.4   Scaling Laws

Dependence of effective properties of cellular solids on relative density is often represented by scaling laws (e.g.,[3]) and generally follows,

$$\frac{\mathrm{E}^*}{\mathrm{E}^{\mathrm{s}}} = c\,(\overline{\rho})^n = c\left(\frac{\rho^*}{\rho_{\mathrm{s}}}\right)^n \qquad (3.3)$$

where c and n are fitting parameters, E^* and E^s represent the effective property of the foam and constituent material, respectively. In addition, $\overline{\rho}$ is the relative density which is defined as the ratio of the density of the foam (ρ^*) to the density to the constituent material (ρ_s). Scaling laws are useful from an application perspective as they: allow for predicting the effective properties of foams over a continuous range of relative densities based on few discrete data points, assist in approximating the effective properties of foams as long

Table 3.2: The variation with relative density of the effective electromechanical properties of transversely poled piezoelectric foams with honeycomb, tetragonal and triangular structures captured by the scaling laws, with the corresponding coefficients a and n as described by Gibson and Ashby [3]. (C^*, e^* and κ^* represent foam properties while C, e and κ represent the properties of the constituent solid material.)

Properties	Honeycomb		Square		Triangular	
	a	n	a	n	a	n
C_{11}^*/C_{11}	0.3286	1.231	0.5245	1.062	0.4445	1.091
C_{12}^*/C_{12}	0.4203	1.047	0.3602	2.152	0.2353	1.124
C_{13}^*/C_{13}	0.4223	1.129	0.4793	1.078	0.4522	1.079
C_{22}^*/C_{22}	0.3388	1.192	0.4339	1.068	0.3178	1.055
C_{23}^*/C_{23}	0.402	1.098	0.3628	1.139	0.321	1.067
C_{33}^*/C_{33}	0.8254	1.012	0.837	1.013	0.8248	1.009
C_{44}^*/C_{44}	0.6625	1.07	0.6225	1.076	0.5729	1.025
C_{55}^*/C_{55}	0.5779	1.084	0.6098	1.069	0.5887	1.07
C_{66}^*/C_{66}	2.219	3.052	0.5023	3.219	0.5031	1.029
e_{16}^*/e_{16}	1.236	3.091	0.2252	3.159	0.2645	1.134
e_{21}^*/e_{21}	-1.523	0.9733	0.2646	2.32	-0.5407	-0.9093
e_{22}^*/e_{22}	0.4677	1.123	0.6595	1.06	0.495	1.031
e_{23}^*/e_{23}	0.3637	1.56	0.4201	1.193	0.3648	1.154
e_{34}^*/e_{34}	0.6626	1.07	0.6225	1.076	0.5729	1.025
$\kappa_{11}^*/\kappa_{11}$	0.899	1.06	1.052	1.015	0.8381	1.048
$\kappa_{22}^*/\kappa_{22}$	0.7561	0.9269	0.6523	1.077	0.4135	0.5346
$\kappa_{33}^*/\kappa_{33}$	1.315	0.9787	1.347	0.981	1.482	1.035

as they are used across foams with fairly similar cellular architectures and constituent materials, and provide some insight into the deformation mechanisms. For instance, as illustrated in reference [3], as the power n increases, bending deformation is dominant and as it approaches unity, stretching deformation is dominant. For the piezoelectric cellular specimens considered in this work, all effective data presented in Figs. 3.4, 3.5 and 3.6, were fitted to the scaling law (Eqn. (3.3)). Resulting fitting constants are reported in Tables 3.2 and 3.3. The in-plane shear properties of the honeycomb structures (i.e., C_{66} in the longitudinally poled system and C_{55} in the transversely poled system) vary with relative density in a non-linear manner (i.e. $n = 3$) indicating that the in-plane shear behavior is bending dominated and hence, the in-plane moduli are expected to be less than that of tetragonal or triangular structures where the corresponding shear moduli vary with relative density in a linear manner (i.e. $n = 1$) indicating that the in-plane shear behavior is stretching dominated. The out-of-plane normal properties (i.e. C_{33} in the longitudinally systems and C_{22} in the transversely poled systems) for the three foam structures exhibit linear variation with relative density (i.e. $n = 1$) indicating that

Table 3.3: The variation with relative density of the effective electromechanical properties of longitudinally poled piezoelectric foams with honeycomb, tetragonal and triangular structures captured by the scaling laws, with the corresponding coefficients a and n as described by Gibson and Ashby [3]. (C^*, e^* and κ^* represent foam properties while C, e and κ represent the properties of the constituent solid material.)

Properties	Honeycomb		Square		Triangular	
	a	n	a	n	a	n
C_{11}^*/C_{11}	0.3212	1.207	0.4429	1.065	0.3915	1.107
C_{12}^*/C_{12}	0.4053	1.03	0.3097	2.156	0.2277	1.072
C_{13}^*/C_{13}	0.3442	1.121	0.3381	1.116	0.3354	1.098
C_{22}^*/C_{22}	0.3216	1.208	0.4429	1.065	0.3081	1.034
C_{23}^*/C_{23}	0.3444	1.121	0.3381	1.116	0.2806	1.044
C_{33}^*/C_{33}	0.7496	1.015	0.7515	1.017	0.7379	1.009
C_{44}^*/C_{44}	0.6229	1.075	0.6159	1.072	0.5248	1.014
C_{55}^*/C_{55}	0.6229	1.075	0.6159	1.072	0.6321	1.072
C_{66}^*/C_{66}	1.528	3.058	0.3597	3.212	0.3947	1.014
e_{15}^*/e_{15}	0.6229	1.075	0.6159	1.072	0.6321	1.072
e_{24}^*/e_{24}	0.6229	1.075	0.6159	1.072	0.5248	1.014
e_{31}^*/e_{31}	0.3442	1.121	0.3381	1.116	0.3354	1.098
e_{32}^*/e_{32}	0.3444	1.121	0.3381	1.116	0.2806	1.044
e_{33}^*/e_{33}	1.091	0.9944	1.099	0.9978	1.095	0.9968
$\kappa_{11}^*/\kappa_{11}$	0.6232	1.075	0.5903	1.036	0.565	1.061
$\kappa_{22}^*/\kappa_{22}$	0.481	0.9115	0.5903	1.036	0.2484	0.3903
$\kappa_{33}^*/\kappa_{33}$	0.9523	0.9552	1.02	1.001	1.008	0.9953

their out-of-plane normal behavior is stretching dominated.

3.4 Discussion and summary

The piezoelectric foams analyzed in this work represent three distinct classes of cellular solids. Hexagonal structures represent bending dominated foams while the triangular structures represent stretching dominated foams. Finally, tetragonal structures represent foams whose dominant deformation mode is dependent on the loading scenario. This classification is based on Maxwells stability criterion which, in the field of cellular solids, has been utilized to give insight into why passive foams are almost always bending dominated [79, 80, 81]. For this discussion it would be instructive to first provide a summary of Maxwells rule.

Maxwells rule as explained in Ref. [69] defines the condition for a pin-jointed frame made up of b struts and j frictionless joints, like those in Fig. 3.7, to be both statically and kinematically determinate. This condition in 2D
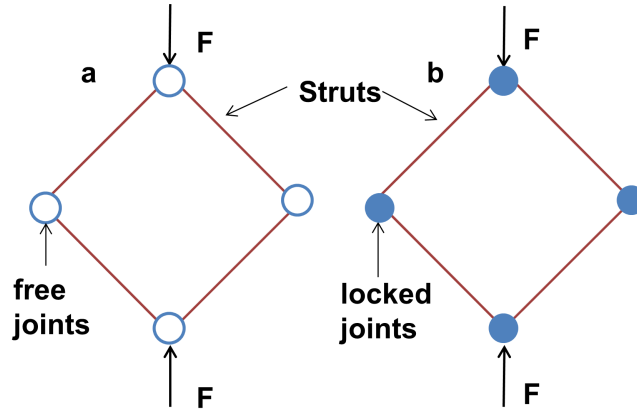
Figure 3.7: (a, b) Shows a schematic illustrating an example of bending and axially deforming structures

is written as,

$$M = b - 2j + 3 = s - m \qquad (3.4)$$

where s and m counts the number of states of self-stress and of mechanisms, respectively. Mathematically, mechanism means that the pin-jointed frame can deform at zero macroscopic force, while self-stress means that struts of a frame can exhibit stresses at zero macroscopic force. However, within the structural mechanics community, mechanism refers to frame with zero stiffness (can collapse under zero force), while self-stress refers to truss with redundant members. Each of s and m can be determined by finding the rank of the equilibrium matrix that describes the frame in a full structural analysis [82]. A rigid framework has $m = 0$. For a large periodic pin-jointed structure with b struts, j joints and an average connectivity α, one can define a relation between b, j and α. Deshpande et al. [69] defined this relation as:

$$b \cong \frac{j\alpha}{2} \qquad (3.5)$$

Using this relation in conjunction with Maxwells criterion, Deshpande et al. [69] analytically showed that the necessary and sufficient condition for rigidity of 2D and 3D periodic frames with similarly situated nodes is $\alpha = 6$ and $\alpha = 12$, respectively. If the connectivity α exceeds these values the frame is

redundant (has self-stress states). Accordingly, a pin-jointed triangular structure with a connectivity (α) of 6 is rigid, while pin-jointed tetragonal ($\alpha = 4$) and hexagonal ($\alpha = 3$) frames are mechanisms. Moreover, by using Maxwells criterion, one can find that the pin-jointed tetragonal and hexagonal frames have one ($m = 1$) and three ($m = 3$) mechanisms, respectively. Therefore, pin-jointed hexagonal frame will collapse under loading along the 1 and 2 directions as well as under shear. On the other hand, pin-jointed tetragonal frame can withstand loads along the 1 and 2 direction but collapses under shear (the single mechanism).

Now, one can imagine that the joints of the pin-jointed frames analyzed above (hexagonal, tetragonal and triangular) can be locked. That is, the joints are not allowed to rotate and can transmit moment. The effect of locking the joints can be anticipated. The pin-jointed triangular frame is a truss whose struts are two-point members and are subjected to axial forces. Therefore, locking the joints of the pin-jointed triangular frame will not have significant effects; at most it would give rise to negligible bending stresses in few struts. Conversely, locking the joints of the pin-jointed hexagonal frame has a significant effect; it will eliminate the three mechanisms and allow the frame to exhibit axial and shear stiffness. As the locked joints are responsible for the load carrying capacity of the hexagonal frame, and as the joints can transfer only moments, struts of the pin-jointed hexagonal frame with locked joints deform mostly by bending, regardless of the loading scenario.

Finally, locking the joints of the pin-jointed tetragonal structure would not affect its response under pure axial loading (along the 1 or 2 directions); however, it would eliminate its shear-type single mechanism and allow the tetragonal frame to provide shear stiffness by promoting bending deformations in the struts. Accordingly, the pin-jointed tetragonal structure with locked joints exhibits a response that depends on the loading scenario; its struts are loaded axially under macroscopic axial loading (in the 1 and 2 direction) and by bending under macroscopic shear loading (in the 1-2 plane).

Each of the piezoelectric cellular structures analyzed in this work can be derived from one of the idealized pin-jointed frames with locked joints discussed

above. Therefore, the analysis of rigidity in the idealized pin-jointed frames, as summarized above, can give valuable insight regarding the mechanical behavior of the piezoelectric cellular structures. The triangular piezoelectric structure is derived from a rigid pin-jointed frame and should deform predominantly by cell wall stretching. On the other hand, the hexagonal piezoelectric structure is derived from a pin-jointed frame with three mechanisms and should be bending dominated. Therefore, the triangular specimen should be mechanically stiffer in the in-plane (i.e. 1-2 plane), which agree with the finite element results.

Finally, the tetragonal piezoelectric foam is derived from the tetragonal pin-jointed frame; therefore it should exhibit axial deformation under uniaxial loading and bending deformation under shear loading. This agrees well with the finite element results which show that the tetragonal specimen has effective elastic and piezoelectric properties that approach those of the triangular specimen under uniaxial loading and approach those of the hexagonal specimen under shear loading (see Figs. 3.4, 3.5 and 3.6).

To confirm that the dominant deformation modes exhibited by the simulated piezoelectric specimens follow the preceding theoretical arguments, stresses developed in the struts of the piezoelectric specimens were extracted, analyzed and used to determine the dominant deformation mode as outlined in Ref. [83]. As the deformation is elastic and stiffness of the struts is uniform, stresses developed in struts can be decomposed using simple mechanics of materials approach into a uniform axial stress and a bending stress that varies linearly along the thickness of the struts. Subsequently, the level of axial and bending stresses are used to deduce the dominate deformation mode.

For the triangular foams, stress decomposition analysis and stress contours demonstrate that, for in-plane uniaxial loading conditions (i.e. 1-2 plane in longitudinally poled systems); the struts are loaded by mostly axial stresses. Under in-plane shear loading (i.e. 1-2 plane in longitudinally poled systems) two thirds of the struts (inclined struts) are observed to be loaded axially while the straight struts are dominated by bending. However, the maximum bending stress in the horizontal struts is less that 25% of the axial stress observed in the inclined struts. For the tetragonal specimens, stress contours

Table 3.4: Analysis of the bending and axial stresses developed across the foam struts at representative locations $L1$ and $L2$ in the honeycomb, tetragonal and triangular foams with 20% relative density when subjected to six (normal and shear) loading conditions. The N metric is evaluated using the formula, $N = 1-$ (Bending stress / Axial Stress).

	Honeycomb (L1)			Honeycomb (L2)		
Properties	Bending Stress (Pa)	Axial Stress (Pa)	N	Bending Stress (Pa)	Axial Stress (Pa)	N
C_{11}	2.35E+04	2.81E+06	0.992	1.36E+06	2.65E+06	0.487
C_{22}	1.35E+04	3.67E+04	0.631	1.15E+06	2.34E+06	0.508
C_{33}	1.80E+00	1.86E+04	1	5.01E+04	3.30E+06	0.985
C_{44}	1.30E-07	1.04E-03	1	1.68E-02	3.75E-01	0.955
C_{55}	8.50E-05	1.35E+00	1	1.58E-02	1.44E-01	0.89
C_{66}	1.83E+06	3.00E+01	-60900	2.33E+08	7.14E+07	-2.26
	Tetragonal (L1)			Tetragonal (L2)		
Properties	Bending Stress (Pa)	Axial Stress (Pa)	N	Bending Stress (Pa)	Axial Stress (Pa)	N
C_{11}	7.82E+04	4.61E+06	0.983	4.59E+04	2.26E+05	0.797
C_{22}	4.76E+04	2.58E+05	0.816	0.00E+00	3.90E+06	1
C_{33}	1.05E+05	5.26E+06	0.98	1.41E+04	3.40E+06	0.996
C_{44}	3.19E-05	1.33E-03	0.976	7.54E-02	4.38E+00	0.983
C_{55}	6.44E-03	1.27E+00	0.995	1.03E-02	1.01E-02	-0.0155
C_{66}	2.29E+04	2.50E-01	-91600	2.17E+06	7.16E+04	-2.93
	Triangular (L1)			Triangular (L2)		
Properties	Bending Stress (Pa)	Axial Stress (Pa)	N	Bending Stress (Pa)	Axial Stress (Pa)	N
C_{11}	5.14E+05	1.57E+07	0.967	1.40E+06	4.30E+06	0.675
C_{22}	1.76E+04	2.43E+05	0.928	7.48E+05	6.91E+06	0.892
C_{33}	5.78E+05	1.67E+07	0.965	5.90E+03	1.68E+07	1
C_{44}	1.23E-04	1.68E-03	0.927	3.28E-03	1.23E+00	0.997
C_{55}	3.18E-02	1.95E+00	0.984	2.96E-03	1.49E+00	0.998
C_{66}	1.06E+06	2.50E+03	-425.0	2.55E+05	4.17E+06	0.939

show that under axial loading the struts are under pure axial loading. On the other hand, for shear loading, the struts mostly exhibit bending-type deformation with the maximum bending occurring near the vertices where maximum bending stresses are more than three orders of magnitude more than the axial stresses.

Finally, for honeycombs, under all loading directions, stress contours showed significant bending deformation with the maximum occurring near vertices. Alkhader and Vural [83] showed using finite element analysis that around 20% of the elastic energy stored in a honeycomb is in the form of stretching energy. Furthermore, the difference in the axial and bending stresses normalized by the axial stress can be used as a metric to gauge the extent of axial vs. bending deformations and predict stiffness level (i.e. high vs. low) when the foams are subjected to fundamental macroscopic deformation modes
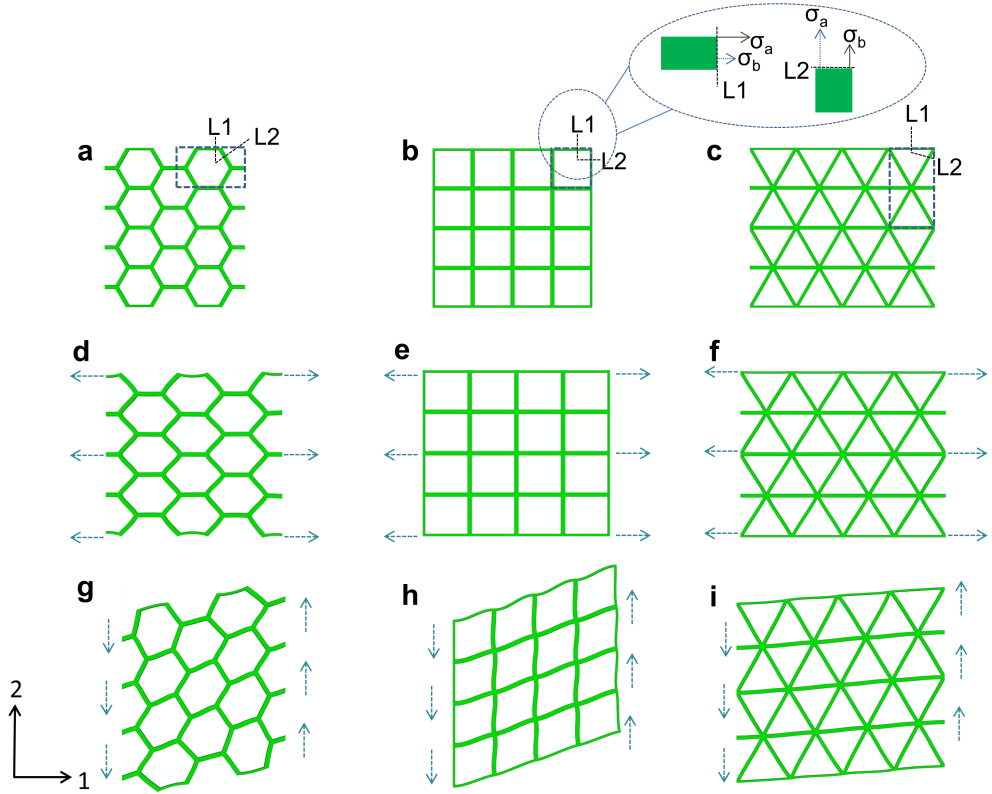
Figure 3.8: A schematic showing the cross-sections $L1$ and $L2$ used to study the effects of axial and bending stresses (in the struts). The cross-section represents regions within the unit-cell (highlighted) with maximum stress. Also shown are the local ($L1$ and $L2$) and global coordinates system to analyze the stress in the sections. (Inset) stresses on the top (σ_a - solid line) and bottom (σ_b - dashed line) are also shown.

(e.g. C_{11} from uniaxial strain, C_{66} from shear strain). When this metric is close to or equal to one, then predominant mode of deformation is expected to be stretching. As bending stresses increase, then proportionally this metric decreases as well (Table 3.4). In this table, axial and bending stresses were found at the force transition points under maximum stresses (referred to as $L1$ and $L2$ in Fig. 3.8). According to the metric (Table 3.4), we expect the four-noded tetragonal structure to deform mostly by stretching when loaded uniaxially in the in-plane direction (i.e. 1 and 2 direction in longitudinally poled systems) as the observed metric is the highest.

Consequently, we expect the corresponding elastic moduli (i.e. C_{11} or E_{11} and C_{22} or E_{22}) to be the highest for the four-noded foam structure.

Similarly, the six-noded triangular structure is expected to deform mostly by stretching under in-plane shear loading (i.e. 1-2 plane in longitudinally poled systems) as the corresponding metric is the highest. Consequently, we expect the corresponding in-plane shear modulus (i.e. C_{66} or G_{12}) to be the highest for the six-noded honeycomb structure as well. These predictions on the elastic moduli based on the analysis of bending and axial stresses are consistent with the trends observed in the finite element analysis (Fig. 3.4).

One should be careful in extending results from this work to other piezo-electrically active cellular solids, since the pin-jointed frame analysis performed, assumes that the pin-jointed structure is large, periodic and has self-situated nodes. Piezoelectric cellular solids with finite, random or non-periodic structures can still be derived from parent pin-jointed structures, but the necessary and sufficient condition of rigidity for these structures might not be 6 in 2D. Instead, the rigidity analysis can be used in a general perspective to provide insight into the mechanical behavior of these piezoelectric cellular solids.

To illustrate, the degree of rigidity of these structures can be related to the number of independent collapse mechanisms (m) in their parent pin-jointed frames through average connectivity α. Then, in general, as the average nodal connectivity increases, the number of collapse mechanisms in the parent structure decreases and the structure shifts toward being stretching dominated. This trend continues until the connectivity satisfies the rigidity condition, beyond which an increase in connectivity increases the number of states of self-stress (redundant members) and has little effect on the effective mechanical properties.

An interesting phenomenon that is worth highlighting is the ability of foam structures or topology to affect the crystal symmetry of a piezoelectric cellular solid. For instance, although the parent material used has negative e_{31}, the triangular piezoelectric specimen exhibited a positive effective e_{31} (see Fig. 3.5). This reversal in sign is caused mainly by the contribution of the inclined struts to the surface charge along the 2-direction due to a load along the 1-direction. To illustrate, Fig. 3.9 shows the surface charge distribution observed
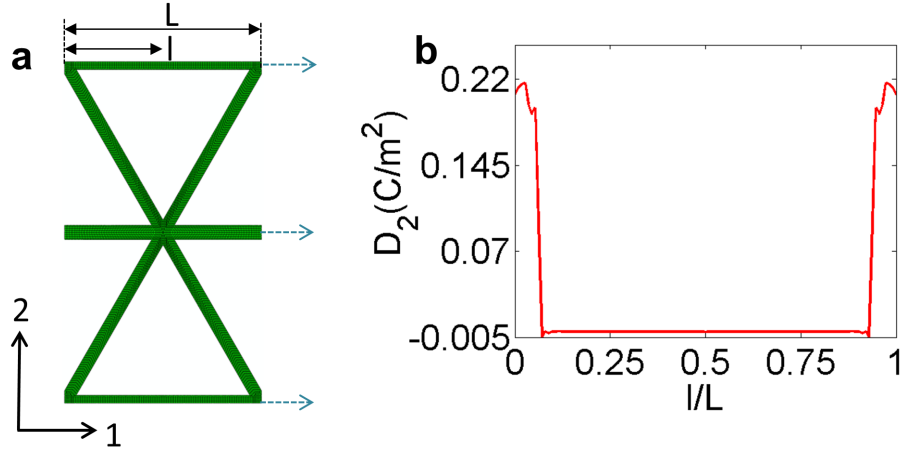
Figure 3.9: (a) A schematic showing the unit-cell under uniaxial strain along the 1-direction where l is the position of the nodes along the face in the 2-direction and L is the total length of the face perpendicular to the 2-direction. (b) A plot showing the variation of the electric displacement along the nodes on the face perpendicular to the 2-direction.

on the top of surface of the triangular specimen due to uniaxial strain along the 1-direction. This figure shows that near the vertices, where the inclined ligaments are contributing, the charge distribution is positive, while the rest of the top surface is exhibiting close to null distribution (very small positive value).

3.5   Conclusions

Active piezoelectric foams are a novel class of materials that have been recently proven to exhibit unique electromechanical properties. Within the context of piezoelectric foams one of the most significant issues related to structure-property coupling is the role of the dominant deformation mode (i.e., bending vs. stretching), which in turn is influenced by a number of factors such as nodal connectivity of the foams, the nature of stresses applied to the foam, the inherent elastic, dielectric and piezoelectric anisotropy of the foam constituent material, the sensitivity of the foam properties to the poling direction and its orientation with respect to the porosity of cellular solids, much of which are yet to be fully understood. Hence, finite element models were developed to characterize the effect of deformation modes (bending vs. stretching) on the

complete electromechanical properties of piezoelectric active foams by studying piezoelectric foams with varying cellular architectures, representative of foams with bending and stretching dominant deformation modes and the following principal conclusions were obtained.

1. The principal elastic, dielectric and piezoelectric properties (such as C_{33}, κ_{33} and e_{33}) of piezoelectric foams are insensitive to foam structure or topology in the longitudinally poled systems. However, the principal electromechanical properties (i.e. C_{33}, κ_{33} and e_{33}) are strongly influenced by the foam structure in the transversely poled systems.

2. The in-plane (i.e. 1-2 plane for longitudinally poled systems and the 1-3 for transversely poled systems) behavior is very sensitive to foam structure and connectivity. The highest in-plane elastic moduli (C_{11} and C_{22} in the longitudinally poled systems and C_{11} and C_{33} in the transversely poled systems) are obtained in the four-noded tetragonal foams while the highest in-plane shear moduli (i.e. C_{66} for the longitudinally poled system and C_{55} for the transversely poled system) are obtained in the six-noded triangular foam structures.

3. The effective out-of-plane elastic properties (i.e. along 3-direction for longitudinally poled systems and along the 2-direction for transversely poled systems), for all the three foam structures depend linearly on relative density. On the other hand, the dependence of the in-plane effective elastic properties (i.e. in the 1-2 plane for longitudinally poled systems and in the 1-3 plane for transversely poled systems) is linear for triangular and tetragonal foam structures and generally non-linear for hexagonal honeycombs.

4. The linear variation of electromechanical properties of piezoelectric foams with relative density is generally associated with a stretching mode of deformation while the non-linear variation is associated with relatively more bending mode of deformation. Thus, the piezoelectric foams can exhibit enhanced stiffness or enhanced compliance in different directions

depending on the deformation mode (respectively, stretching or bending) which in-turn is influenced by nodal connectivity and the nature of stress that is applied. For example, the six-noded triangular foams exhibit outstanding in-plane shear modulus as the dominant mode of deformation under in-plane shear loading is stretching.

5. Appropriate scaling laws that can be assist in predicting the effective electromechanical properties of piezoelectric cellular solids have been identified. The coefficients of the scaling laws that were obtained further indicate that the triangular structures deform predominantly by axial stretching.

6. Amongst the longitudinally poled systems, the triangular structures with the highest nodal connectivity of six exhibit figures of merit (acoustic impedance, piezoelectric charge coefficient, hydrostatic figure of merit and piezoelectric coupling constant) which are similar to other foam structures as well as outstanding in-plane shear properties which are significantly better than those of the tetragonal or hexagonal foam structures.

7. Overall, the transversely poled systems exhibit better figures of merit (acoustic impedance, piezoelectric charge coefficient and hydrostatic figure of merit) than the longitudinally poled systems. Amongst the transversely poled systems, the tetragonal structure with a moderate level of nodal connectivity of four exhibits the best overall combination of high piezoelectric coupling constant, piezoelectric charge coefficient and the hydrostatic figure of merit with a marginally higher acoustic impedance as compared to that of the hexagonal or triangular foams.

8. Results confirm that foam structure or topology can be tailored to optimize a set of piezoelectric constants that are desired for a particular application.

Electromechanical Response of (3-0, 3-1) Particulate, Fibrous, and Porous Piezoelectric Composites with Anisotropic Constituents: An Analytical Model based on the Homogenization Method

4.1 Outline of the chapter

Amongst the models that were developed following the Eshelby-type approach, early work was focused on extending the Eshelby's solution [84] for anisotropic piezoelectric inclusions in the elastic domain [85, 86, 87, 88]. However, a closed-form solution for the components of the Eshelby tensor was not obtained. Consequently, a numerical scheme was employed to solve for the components of the Eshelby tensor for an anisotropic system [89]. Prior work done by Deeg [90] and Wang [91] was extended by Dunn and Taya [48] to obtain a solution for the piezoelectric inclusion problem. An alternate solution to the inclusion problem was presented by Beneveniste [92] and Chen [93] who extended the generalized solution of Hill and Walpole. Dunn and Taya [48] and Beneveniste [92] and Chen [93] obtained the four tensors that comprise the equivalent of the Eshelby tensor in the piezoelectric domain. However, they did not provide explicit closed-form expressions for them. Dunn et al. [94, 49] gave the explicit forms for the equivalent Eshelby tensor in terms of a surface integral over a unit sphere, which had to be evaluated numerically. Mikata [51] derived explicit solutions for the components of the Eshelby tensor by solving a special bi-cubic

equation [52] which was specialized for the case of spheroidal inclusions.

Several analytical models that predict the electromechanical properties of piezoelectric composites by invoking homogenization techniques have also been developed. Challagulla and Venkatesh [44] formulated an asymptotic homogenization method to obtain the complete electromechanical properties of 2-2 type layered composites with anisotropic constituents. They studied two classes of layered piezoelectric composites (i.e., longitudinally layered and transversely layered) to obtain the effective properties in the limits of both large-volume (i.e., bulk) and small-volume (i.e., thin-film) systems. An extension of the asymptotic homogenization method to obtain the properties of 1-3 type long-fiber piezoelectric composites with transversely isotropic constituents was presented in the works of Bravo-Castillero,et al. [2]. Bisegna and Luciano [45, 46] provided variational bounds to estimate the homogenized properties of piezoelectric composites as well. Hori and Nemat-Nasser [47] have obtained Hashin-Shtrikman type exact bounds for electroactive composites. The bounds presented by them are general and apply to non-linear constituent phases although exact solutions are not provided for the fully anisotropic matrix-particle material property tensors. However, an analytical model that provides explicit closed-form solutions to the most general problem of a piezoelectric composite with anisotropic particulate constituents is not yet available.

Hence, the objectives of the present study are: (i) To develop an analytical framework for predicting the complete elastic, dielectric and piezoelectric properties of piezoelectric composites with anisotropic constituents; (ii) To validate the analytical model with a finite element model for a range of piezoelectric composites that exhibit varying degrees of elastic anisotropy and piezoelectric activity.

In the present study, the homogenization method introduced by Suquet et al. [95] is invoked to predict the electromechanical properties of piezoelectric composites with anisotropic constituents. This method has been successfully used to predict the homogenized properties of fiber-reinforced elastomers with periodic microstructures by Brun et al. [96]

51

The present work is outlined as follows, Section 4.2 presents the mathematical formulation of the piezoelectric problem, the constitutive equations, and the periodic fields. Section 4.3 highlights the concepts that have been invoked to solve the equilibrium equations with the approximation of piecewise constant polarization fields that are introduced to simplify the equations for the strain and the electric field and expressions for the effective electromechanical properties are provided in terms of the concentrations tensors. The details of the three-dimensional finite-element model invoked in the present study to predict the effective properties of periodic piezoelectric composites, are provided in Section 4.4. The results of the analytical model developed in the present study are compared to those of the finite element model for four piezoelectric composite systems that exhibit varying degrees of anisotropy in Section 4.5. Key conclusions from the present study are presented in Section 4.6.

4.2 Preliminaries on piezoelectric composites with periodic microstructure

Consider an infinitely large composite made up of aligned long cylindrical fibers/pores distributed periodically in a piezoelectric matrix phase (Fig. 4.1). It is assumed here when discussing 'effective properties' that there is a separation of length-scales within the problem. The local or microscopic scale is one where the heterogeneities can be identified separately. The macroscopic or overall scale is one where the heterogeneities can be 'averaged-out'. A given sample of this material is assumed to occupy a volume Ω, with boundary $\partial\Omega$. The effective properties at the macroscopic scale are determined using geometric and material data of an appropriate representative volume element or unit cell. The infinitely large composite can be generated by adding contiguously the unit cell in all three directions.

In the remainder of the paper, symbolic and Einstein index notation is used to represent field variables (scalars, vectors, and tensors). In symbolic notation, a vector or tensor is represented by a bold face letter. In index

notation, partial differentiation is denoted by a 'comma', e.g., the divergence of stress using symbolic and indicial notation would be given, respectively, by, $\boldsymbol{\nabla} \cdot \boldsymbol{\sigma} = \sigma_{ij,j}$ where repeating indices imply a summation.
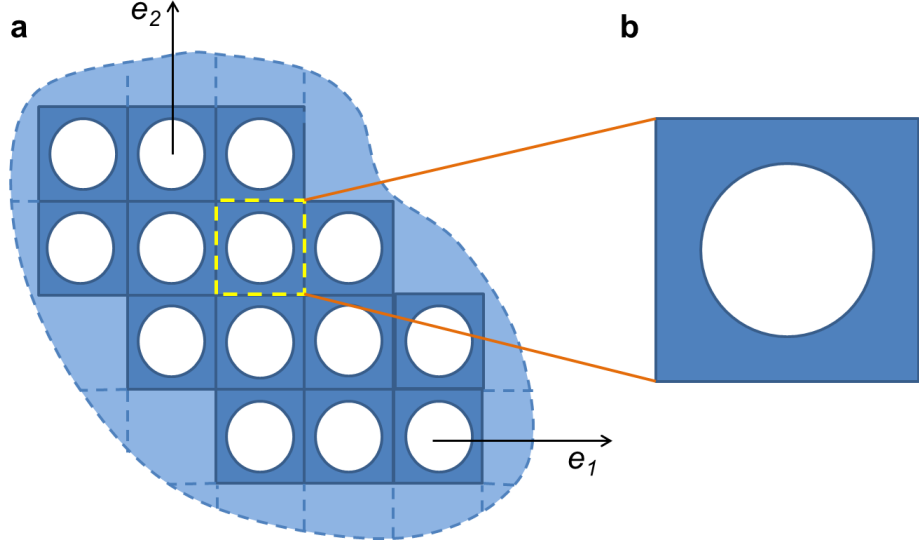
Figure 4.1: Schematic illustration showing: (a) an infinite piezoelectric body with periodic distribution of long cylindrical fibers and (b) a square unit-cell occupying volume Ω.

A material point within the given specimen is denoted by $\mathbf{x}$ (at the microscopic level). The infinitesimal strain tensor, $\boldsymbol{\varepsilon}$, at $\mathbf{x}$ for a displacement field, $\mathbf{u}$ and the electric field, $\mathbf{E}$, in terms of a scalar electric potential ϕ are defined as:

$$\varepsilon_{ij} = \frac{1}{2}(u_{i,j} + u_{j,i}), \qquad E_n = -\phi_{,n} \tag{4.1}$$

The constitutive behaviour of the matrix and the cylindrical fibers is assumed to be linear elastic and characterized by the stored-energy functions, $W^{(1)}$ and $W^{(2)}$, respectively. The two functions are taken to be convex functions of the strain($\boldsymbol{\varepsilon}$) and electric field ($\mathbf{E}$), so that the local energy function of the composite may be written as:

$$W(\mathbf{x}; \boldsymbol{\varepsilon}, \mathbf{E}) = (1 - \chi(\mathbf{x}))W^{(1)}(\mathbf{x}; \boldsymbol{\varepsilon}, \mathbf{E}) + \chi(\mathbf{x})W^{(2)}(\mathbf{x}; \boldsymbol{\varepsilon}, \mathbf{E}) \tag{4.2}$$

where χ is known as the characteristic function, equal to 1 if the position vector $\mathbf{x}$ is inside phase r and zero otherwise and describes the distribution of the phases (i.e., the microstructure). Taking piezoelectricity as a linear phenomenon, the work function, $W^{(r)}(r = 1, 2)$, is assumed to be a convex function. The local constitutive behaviour for the constituent phases in the piezoelectric composite can be derived from the convex work energy function, $W^{(r)}(\boldsymbol{\varepsilon}, \mathbf{E}) = \frac{1}{2}\mathrm{L}_{ijkl}^{(r)}\varepsilon_{ij}^{(r)}\varepsilon_{kl}^{(r)} - e_{kij}^{(r)}\mathrm{E}_k^{(r)}\varepsilon_{ij}^{(r)} - \frac{1}{2}\kappa_{ij}^{(r)}\mathrm{E}_i^{(r)}\mathrm{E}_j^{(r)}$ as:

$$\boldsymbol{\sigma} = \frac{\partial W}{\partial \boldsymbol{\varepsilon}}(\mathbf{x}; \boldsymbol{\varepsilon}, \mathbf{E}) \qquad \text{and} \qquad \mathbf{D} = \frac{\partial \mathbf{W}}{\partial \mathbf{E}}(\mathbf{x}; \boldsymbol{\varepsilon}, \mathbf{E}) \qquad (4.3)$$

where, $\boldsymbol{\sigma}$ is the Cauchy stress tensor and $\mathbf{D}$ is the electric displacement vector. The effective stored energy function, $\widetilde{W}$, of the two-phase piezoelectric composite under the separation of length-scales hypothesis is given by,

$$\widetilde{W}(\mathbf{x}; \overline{\boldsymbol{\varepsilon}}, \overline{\mathbf{E}}) = \min_{\boldsymbol{\varepsilon} \in \mathcal{K}(\overline{\boldsymbol{\varepsilon}})} \max_{\mathbf{E} \in \mathcal{J}(\overline{\mathbf{E}})} \sum_{r=1}^{2} c^{(r)} \left\langle W^{(r)}(\mathbf{x}; \boldsymbol{\varepsilon}, \mathbf{E}) \right\rangle^{(r)} \qquad (4.4)$$

and defined over the set of all kinematically admissible strain and electric fields given by $\mathcal{K}$ and $\mathcal{J}$, such that:

$$\mathcal{K}(\overline{\boldsymbol{\varepsilon}}) = \{\boldsymbol{\varepsilon}| \text{ with } \boldsymbol{\varepsilon} = \frac{1}{2}\left(\boldsymbol{\nabla}\boldsymbol{u} + \boldsymbol{\nabla}\boldsymbol{u}^{\boldsymbol{T}}\right) \text{ in } \Omega, \ \boldsymbol{u} = \overline{\boldsymbol{\varepsilon}}\mathbf{x} \text{ on } \partial\Omega\} \qquad (4.5)$$

and

$$\mathcal{J}(\overline{\mathbf{E}}) = \{\mathbf{E}| \text{ with } \mathbf{E} = -\nabla\phi \text{ in } \Omega, \ \phi = -\overline{\mathbf{E}} \cdot \mathbf{x} \text{ on } \partial\Omega\} \qquad (4.6)$$

In all the expressions presented above, the triangular brackets $\langle\cdot\rangle$ and $\langle\cdot\rangle^{(r)}$ denote, respectively, the volume averages over the specimen,(Ω), and the phase r ($\Omega^{(r)}$). The scalars, $c^{(1)}$ and $c^{(2)}$ denote the volume fractions of the two constituent phases of the periodic composite. It is also important to note that the average electroelastic energy, $\widetilde{W}$, stored in the fiber-reinforced composite when subjected to an affine strain and electric field (Hill-type boundary data [97]) is consistent with the condition $\langle\boldsymbol{\varepsilon}\rangle = \overline{\boldsymbol{\varepsilon}}$ and $\langle\mathbf{E}\rangle = \overline{\mathbf{E}}$. The following is the equivalent statement of Hill's lemma for the case of piezoelectric constituent

phases,

$$\langle \boldsymbol{\sigma} : \boldsymbol{\varepsilon} \rangle = \langle \boldsymbol{\sigma} \rangle : \langle \boldsymbol{\varepsilon} \rangle \qquad \text{and} \qquad \langle \mathbf{D} \cdot \mathbf{E} \rangle = \langle \mathbf{D} \rangle \cdot \langle \mathbf{E} \rangle \qquad (4.7)$$

From the arguments presented above we can then say that the macroscopic constitutive behaviour for composite can then be expressed by:

$$\overline{\boldsymbol{\sigma}} = \frac{\partial \widetilde{W}}{\partial \overline{\boldsymbol{\varepsilon}}} (\mathbf{x}; \overline{\boldsymbol{\varepsilon}}, \overline{\mathbf{E}}) \qquad \text{and} \qquad \overline{\mathbf{D}} = \frac{\partial \widetilde{W}}{\partial \overline{\mathbf{E}}} (\mathbf{x}; \overline{\boldsymbol{\varepsilon}}, \overline{\mathbf{E}}) \qquad (4.8)$$

where $\overline{\boldsymbol{\sigma}} = \langle \boldsymbol{\sigma} \rangle$ and $\overline{\mathbf{D}} = \langle \mathbf{D} \rangle$ are the average stress and the average electric displacement in the fiber-reinforced composite, respectively. The variational problem for electroelastic composites in the linear elastic domain (4.4) with periodic microstructure can be expressed explicitly as follows:

$$\widetilde{W}(\mathbf{x}; \overline{\boldsymbol{\varepsilon}}, \overline{\mathbf{E}}) = \min_{\boldsymbol{\varepsilon} \in \mathcal{K}(\overline{\boldsymbol{\varepsilon}})} \max_{\mathbf{E} \in \mathcal{J}(\overline{\mathbf{E}})} \frac{1}{|\Omega|} \int_{\Omega} W(\mathbf{x}; \boldsymbol{\varepsilon}, \mathbf{E}) \mathrm{d}\mathbf{x} \qquad (4.9)$$

4.3 Suquet estimates for linear piezoelectric constituents

Based on the framework presented in the previous section, the main objective of the current study is to provide explicit homogenization estimates for the electromechanical properties of a periodic distribution of particulate inclusions/exclusions of arbitrary geometrical shape in a general piezoelectric matrix phase of anisotropic material symmetry. This is accomplished by extending Suquet's homogenization estimates [95] to the domain of periodic piezoelectric composites. This method has already been applied to elastic materials and provides good estimates for the effective properties of composite materials with periodic microstructure. This section outlines the basic framework of how the Suquet estimates have been used to derive estimates for effective electromechanical constants. Making use of the results provided by Suquet for two-phase composites with periodic microstructure (Fig. 4.2), an estimate for the overall stored-energy function, $\widetilde{W}$, is provided using the volume fraction of the fibres, $c^{(2)}$, with stored-energy function, $W^{(2)}$, distributed periodically

55
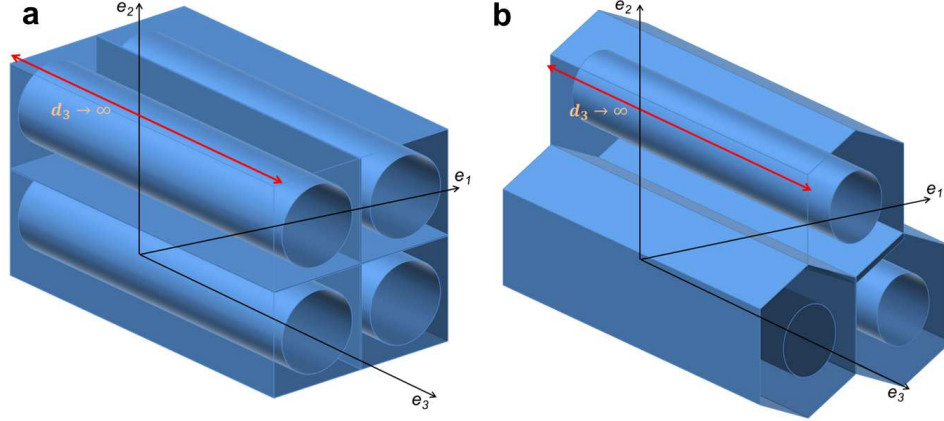
Figure 4.2: Schematic representation of the microstructures showing: (a) a square distribution of long cylindrical pores, and (b) hexagonal distribution of long cylindrical pores.

in a piezoelectric matrix with stored-energy function, $W^{(1)}$.

The linear constitutive equations can be derived from (4.3) and are written as:

$$\sigma_{ij} = \mathrm{L}_{ijkl}\varepsilon_{kl} + \mathrm{e}_{kij}\phi_{,k} \tag{4.10}$$

$$D_k = \mathrm{e}_{kij}\varepsilon_{ij} - \kappa_{ki}\phi_{,i} \tag{4.11}$$

The above relations (4.10) and (4.11) characterize the complete electromechanical response of a piezoelectric composite. The tensors, **L**, **e**, and $\boldsymbol{\kappa}$, respectively, denote the fourth-rank elastic modulus tensor with major and minor symmetry, the piezoelectric constant tensor with minor symmetry in i and j, and the dielectric constants tensor with major symmetry. Latin indices have been employed in the derivation of the present model with all indices ranging from 1 to 3. The piezoelectric composite has to satisfy the following equilibrium equations:

$$\frac{\partial \sigma_{ij}}{\partial x_j} = \sigma_{ij,j} = 0 \qquad \text{and} \qquad \frac{\partial D_k}{\partial x_k} = D_{k,k} = 0 \tag{4.12}$$

which, respectively, ensure mechanical equilibrium and the absence of free charge. In addition to the equilibrium equation, the jump conditions for stress and electric displacement across the boundary interface $\partial\Omega$, given by: $[\boldsymbol{\sigma} \cdot \mathbf{n}]$

$= 0$ and $[\mathbf{D} \cdot \mathbf{n}] = 0$, on the opposite sides of $\partial \Omega$ must be satisfied.

Substituting the constitutive Eqs. (4.10) and (4.11) for stress and electric displacement into Eq. (4.12) and using the definition for infinitesimal strain and electric field, the equilibrium and charge-free condition can be written in terms of the material property tensors as,

$$[\mathrm{L}_{ijkl}(\mathbf{x})\varepsilon_{kl}]_{,j} + [\mathrm{e}_{kij}(\mathbf{x})\phi_{,k}]_{,j} = 0 \qquad (4.13)$$

$$[\mathrm{e}_{ikl}(\mathbf{x})\varepsilon_{kl}]_{,i} - [\kappa_{ik}(\mathbf{x})\phi_{,k}]_{,i} = 0 \qquad (4.14)$$

Note the argument $\mathbf{x}$ in the above equations denotes the dependence of the fundamental material constants on the position vector in the representative volume element.

At this point it is useful to introduce a homogeneous reference medium with constant properties $(\mathbf{L}^{(0)}, \mathbf{e}^{(0)}, \boldsymbol{\kappa}^{(0)})$ and polarization fields defined by, $\boldsymbol{\tau}^{(L)} = [\mathbf{L}^{(\mathbf{r})} - \mathbf{L}^{(\mathbf{0})}]\boldsymbol{\varepsilon}$, $\boldsymbol{\tau}^{(CE)} = [\mathbf{e}^{(\mathbf{r})} - \mathbf{e}^{(\mathbf{0})}]\mathbf{E}$, $\boldsymbol{\tau}^{(C\varepsilon)} = [\mathbf{e}^{(\mathbf{r})} - \mathbf{e}^{(\mathbf{0})}]\boldsymbol{\varepsilon}$, $\boldsymbol{\tau}^{(\kappa)} = [\boldsymbol{\kappa}^{(\mathbf{r})} - \boldsymbol{\kappa}^{(\mathbf{0})}]\mathbf{E}$. The superscripts (CE) and $(C\varepsilon)$ denote the coupling of the piezoelectric constant in Eqs. (4.13) and (4.14) with the electric field and strain, respectively. The form of the equilibrium equations for stress and the Maxwell equation for electric displacement, on the introduction of the reference medium and the polarization fields are given by:

$$\mathrm{L}_{ijmn}^{(0)}u_{m,nj} + \mathrm{e}_{kij}^{(0)}\phi_{,kj} + \left[\tau_{ij}^{(L)} + \tau_{ij}^{(CE)}\right]_{,j} = 0 \qquad (4.15)$$

and

$$\mathrm{e}_{ikl}^{(0)}u_{k,li} - \kappa_{ik}^{(0)}\phi_{,ki} + \left[\tau_i^{(C\varepsilon)} - \tau_i^{(\kappa)}\right]_{,i} = 0 \qquad (4.16)$$

The local problem for the displacement and electric potential can be split into its overall and periodic parts such that $\boldsymbol{u} = \boldsymbol{u^0} + \boldsymbol{u^*}$ and $\phi = \phi^0 + \phi^*$, where the quantities with superscript $(\cdot)^0$ and $(\cdot)^*$ denote the average and periodic components of the overall fields, respectively. Here, we have used the periodicity of the micro-structure in order to be able to re-write the equilibrium equations for the stress and electric displacement as a super-position of the two

57

strain states, the periodic strain at the microscopic level and the overall strain at the boundary of the infinite medium. It is important to note that the volume average of the periodic strain and electric field is zero, i.e., the periodic strain and electric field are anti-symmetric across the boundaries of the representative volume element (RVE) [95]. Re-writing the stress equilibrium equation by decomposing the overall strain and electric field, we note that the far-field strain and electric field (which are constants) satisfy the following equation,

$$L^0_{ijmn}u^0_{m,nj} + e^0_{nij}\phi^0_{,nj} = 0 \qquad \text{and} \qquad e^{(0)}_{imn}u^0_{m,ni} - \kappa^{(0)}_{in}\phi^0_{,ni} = 0 \quad (4.17)$$

The solution for the periodic strain and electric field are outlined in the following sub-section.

4.3.1 Periodic Green's operators

To simplify the above equations we introduce, respectively, the stress and electric displacement polarization fields $\boldsymbol{\tau}$ and $\mathbf{t}$ such that: $\tau_{ij} = \tau^{(L)}_{ij} + \tau^{(CE)}_{ij}$ and $t_i = \tau^{(C\varepsilon)}_i + \tau^{(\kappa)}_i$ which in terms of the material property tensors is given by,

$$\tau_{ij} = \Delta L_{ijkl}\varepsilon_{kl} + \Delta e_{ijk}\phi_{,k} \qquad (4.18)$$

$$t_i = \Delta e_{ijk}\varepsilon_{jk} + \Delta\kappa_{ik}\phi_{,k}. \qquad (4.19)$$

Eqs. (4.15) and (4.16) should be solved for the periodic strain and electric field such that the stress equilibrium and Maxwell's equation for a representative volume element are satisfied. The divergence of the stress and electric displacement in the form given by Eq. (4.15) and Eq. (4.16) can be solved for the strain and electric field by taking the Fourier transform and solving for the periodic Green's operators [98, 96, 99]. Note that the method of Fourier transform to pass the above equations to Fourier space is made possible by the introduction of the reference medium with constant electromechanical properties. Substituting Eqs.(4.18)and(4.19) using the newly defined polarizations fields $\boldsymbol{\tau}$ and $\boldsymbol{t}$ in Eq.(4.15) and Eq. (4.16) give the following relations (in

Fourier space):

$$-K_{ik}\widehat{u_k^*} - q_i\widehat{\phi^*} + i\xi_j\widehat{\tau_{ij}} = 0 \qquad (4.20)$$

$$-q_i\widehat{u_k^*} + p\widehat{\phi^*} + i\xi_i\widehat{t_i} = 0 \qquad (4.21)$$

where the terms $\mathbf{K}$, $\mathbf{q}$, and p are given by, $K_{ik} = L_{ijkl}^{(0)}\xi_j\xi_l$; $q_i = e_{kij}^{(0)}\xi_j\xi_k$ and $p = \kappa_{ik}^{(0)}\xi_i\xi_k$, the explicit forms of which have been given for a periodic square, hexagonal and cubic distribution of fibers/pores in Appendix C. The Eqs. (4.20) and (4.21) can then be used to solve for the components of the periodic displacement and electric potential in Fourier space which are given by:

$$\widehat{u_m^*} = iN_{mi}\xi_j\widehat{\tau_{ij}} + \frac{i}{p}N_{mi}q_i\widehat{t_k}\xi_k \qquad (4.22)$$

and

$$\widehat{\phi^*} = \frac{i}{p}q_kN_{ki}\xi_j\widehat{\tau_{ij}} + \frac{i}{p}\left(\frac{1}{p}q_kN_{ki}q_i - 1\right)\xi_l\widehat{t_l} \qquad (4.23)$$

where $\mathbf{K}$ and $\mathbf{N}$ represent the acoustic tensor of the homogeneous reference medium and its inverse, respectively. The $(\widehat{\cdot})$ denotes the Fourier transform of the corresponding field within the parenthesis (for e.g., $\widehat{\mathbf{u}}$ is the Fourier transform of displacement). To solve for the periodic strains and electric fields in the Fourier space we take the gradients of the displacement and electric potential. The final expressions for strain and electric field are in the form of the periodic Lippmann-Schwinger integral equation (in Fourier space) [98] given by:

$$\widehat{u_{m,n}^*} = -N_{mi}\xi_j\xi_n\widehat{\tau_{ij}} - \frac{1}{p}N_{mi}q_i\xi_n\xi_k\widehat{t_k} \qquad (4.24)$$

and

$$\widehat{\phi_{,p}^*} = -\frac{1}{p}q_kN_{ki}\xi_j\xi_p\widehat{\tau_{ij}} - \frac{1}{p}\left(\frac{1}{p}q_kN_{ki}q_i - 1\right)\xi_p\xi_l\widehat{t_l} \qquad (4.25)$$

The above equations can be further simplified by identifying the 3 period Green's operators associated with the elastic, piezoelectric, and dielectric constants, respectively. The expressions for the Green's operators are given by:

$$H_{mnji} = N_{mi}\xi_j\xi_n \tag{4.26}$$

$$\beta_{kmn} = \frac{1}{p}N_{mi}q_i\xi_n\xi_k \tag{4.27}$$

$$\gamma_{pl} = \frac{1}{p}\left(\frac{1}{p}q_kN_{ki}q_i - 1\right)\xi_p\xi_l \tag{4.28}$$

4.3.2 Equations for strain and electric field

The periodic strains derived in the previous section can be combined with the applied strain, ε^0, on the boundary of the unit cell assemblage to yield an expression for the overall strain in the unit cell. The equations for the gradient of displacement and the electric field in the unit cell are given by:

$$u_{m,n} = \varepsilon_{mn}^0 - \sum_{\boldsymbol{\xi}\in\mathcal{R}^*-\{0\}} H_{mnij}\widehat{\tau}_{ij}e^{i\boldsymbol{\xi}\cdot\mathbf{x}} - \sum_{\boldsymbol{\xi}\in\mathcal{R}^*-\{0\}} \beta_{kmn}\widehat{t}_k e^{i\boldsymbol{\xi}\cdot\mathbf{x}} \tag{4.29}$$

and

$$\phi_{,p} = \phi_{,p}^0 - \sum_{\boldsymbol{\xi}\in\mathcal{R}^*-\{0\}} \beta_{pij}\widehat{\tau}_{ij}e^{i\boldsymbol{\xi}\cdot\mathbf{x}} - \sum_{\boldsymbol{\xi}\in\mathcal{R}^*-\{0\}} \gamma_{pl}\widehat{t}_l e^{i\boldsymbol{\xi}\cdot\mathbf{x}} \tag{4.30}$$

The polarizations in the stress and electric field are constant in the phase (matrix/particle) but are overall non-homogeneous in the representative volume element. When solving the above set of equations it is common to assume piece-wise constant polarization fields. This provides a good approximation when computing the overall properties of the periodic piezoelectric composite and gives us bounds for the electromechanical properties as shall be seen with the comparisons with finite-element analysis results. For constant polarization fields it can be shown the bounds obtained are those of Voigt and Reuss depending on the chosen field, i.e., by assuming constant strain we obtain Voigt bounds and by assuming constant stress polarization we obtain Reuss

bounds. The polarization fields are not required to satisfy the compatibility equation because they are trial fields for stress and electric displacement. From the definition of the Fourier transform of the polarization fields we have, $\widehat{\tau}_{ij} = \langle \tau_{ij}(\mathbf{x}) \, e^{-i\boldsymbol{\xi} \cdot \mathbf{x}} \rangle$ and $\widehat{t}_l = \langle t_l(\mathbf{x}) \, e^{-i\boldsymbol{\xi} \cdot \mathbf{x}} \rangle$. Using the property of the polarizations to be constant in the phases, we can use a first-order (piece-wise constant) approximation to define the polarization field in terms of a characteristic function, in real space as,

$$\tau_{ij}(\mathbf{x}) = \sum_{r=1}^{n} \chi^{(r)}(\mathbf{x}) \, \tau_{ij}, \qquad t_i(\mathbf{x}) = \sum_{r=1}^{n} \chi^{(r)}(\mathbf{x}) \, t_i \tag{4.31}$$

where $\chi^{(r)}$ is the characteristic function, the value of which is equal to 1 when $\mathbf{x} \in r$ and zero otherwise. After evaluating the volume integrals (from the definition of the Fourier transform) we obtain,

$$\widehat{\tau}_{ij} = \sum_{r=1}^{n} c^{(r)} \overline{\tau}_{ij}^{(r)} \left\langle e^{-i\boldsymbol{\xi} \cdot \mathbf{x}} \right\rangle^{(r)}, \qquad \widehat{t}_i = \sum_{r=1}^{n} c^{(r)} \overline{t}_i^{(r)} \left\langle e^{-i\boldsymbol{\xi} \cdot \mathbf{x}} \right\rangle^{(r)} \tag{4.32}$$

where the $\langle \cdot \rangle$ operator denotes the volume average given by, $\frac{1}{|V|} \int_V e^{-i\boldsymbol{\xi} \cdot \mathbf{x}} d\mathbf{x}$. For a two-phase composite we choose the properties of the reference medium such that the polarization in the matrix phase is zero. This is achieved by making $\left[\mathbf{L}^{(0)}, \mathbf{e}^{(0)}, \boldsymbol{\kappa}^{(0)}\right] = \left[\mathbf{L}^{(1)}, \mathbf{e}^{(1)}, \boldsymbol{\kappa}^{(1)}\right]$. Eq. (4.32) can then be further simplified by making use of the fact that the polarization in the matrix is zero, to obtain the expression for $\widehat{\tau}_{ij}$ given by,

$$\widehat{\tau}_{ij} = c^{(2)} \left(\Delta L_{ijmn}^{(2)} \overline{\varepsilon}_{mn}^{(2)} + \Delta e_{kij} \overline{\phi}_{,k}^{(2)} \right) \left\langle e^{-i\boldsymbol{\xi} \cdot \mathbf{x}} \right\rangle^{(2)} \tag{4.33}$$

and the polarization $\widehat{t}_l$ as,

$$\widehat{t}_l = c^{(2)} \left(\Delta e_{lmn}^{(2)} \overline{\varepsilon}_{mn}^{(2)} - \Delta \kappa_{lm}^{(2)} \overline{\phi}_{,m}^{(2)} \right) \left\langle e^{-i\boldsymbol{\xi} \cdot \mathbf{x}} \right\rangle^{(2)} \tag{4.34}$$

We can determine the average strains in the particle phase by substituting the above defined equations for polarizations in stress and electric displacement

in Eq. (4.29) and Eq. (4.30) to obtain,

$$\overline{\varepsilon}_{mn}^{(2)} = \varepsilon_{mn}^0 -$$
$$\sum_{\boldsymbol{\xi} \in \mathcal{R}^* - \{0\}} c^{(2)} \mathrm{H}_{mnij}^s \left\langle \mathrm{e}^{-\mathrm{i}\boldsymbol{\xi} \cdot \mathbf{x}} \right\rangle^{(2)} \left\langle \mathrm{e}^{\mathrm{i}\boldsymbol{\xi} \cdot \mathbf{x}} \right\rangle^{(2)} \left(\Delta L_{ijpq}^{(2)} \overline{\varepsilon}_{pq}^{(2)} + \Delta e_{kij} \overline{\phi}_{,k}^{(2)} \right)$$
$$- \sum_{\boldsymbol{\xi} \in \mathcal{R}^* - \{0\}} c^{(2)} \beta_{kmn}^s \left\langle \mathrm{e}^{-\mathrm{i}\boldsymbol{\xi} \cdot \mathbf{x}} \right\rangle^{(2)} \left\langle \mathrm{e}^{\mathrm{i}\boldsymbol{\xi} \cdot \mathbf{x}} \right\rangle^{(2)} \left(\Delta e_{lmn}^{(2)} \overline{\varepsilon}_{mn}^{(2)} - \Delta \kappa_{lm} \overline{\phi}_{,m}^{(2)} \right)$$

$$(4.35)$$

and

$$\overline{\phi}_{,p}^{(2)} = \phi_{,p}^0 -$$
$$\sum_{\boldsymbol{\xi} \in \mathcal{R}^* - \{0\}} c^{(2)} \beta_{pij}^s \left\langle \mathrm{e}^{-\mathrm{i}\boldsymbol{\xi} \cdot \mathbf{x}} \right\rangle^{(2)} \left\langle \mathrm{e}^{\mathrm{i}\boldsymbol{\xi} \cdot \mathbf{x}} \right\rangle^{(2)} \left(\Delta L_{ijmn}^{(2)} \overline{\varepsilon}_{mn}^{(2)} + \Delta e_{kij} \overline{\phi}_{,k}^{(2)} \right)$$
$$- \sum_{\boldsymbol{\xi} \in \mathcal{R}^* - \{0\}} c^{(2)} \gamma_{pl}^s \left\langle \mathrm{e}^{-\mathrm{i}\boldsymbol{\xi} \cdot \mathbf{x}} \right\rangle^{(2)} \left\langle \mathrm{e}^{\mathrm{i}\boldsymbol{\xi} \cdot \mathbf{x}} \right\rangle^{(2)} \left(\Delta e_{lmn}^{(2)} \overline{\varepsilon}_{mn}^{(2)} - \Delta \kappa_{lm} \overline{\phi}_{,m}^{(2)} \right)$$

$$(4.36)$$

The superscript 's' implies that the tensor has been symmetrized in order to obtain the symmetric part of the gradient of displacement. The symmetrization is carried out as follows, $\mathrm{H}_{ijmn}^s = \frac{1}{4} \left(\mathrm{H}_{ijmn} + \mathrm{H}_{jimn} + \mathrm{H}_{ijnm} + \mathrm{H}_{mnij} \right)$, $\beta_{imn}^s = \frac{1}{2} \left(\beta_{imn} + \beta_{inm} \right)$, and $\gamma_{mn}^s = \frac{1}{2} \left(\gamma_{mn} + \gamma_{nm} \right)$.

We define the three microstructural tensors, $\mathbf{P}$, $\mathbf{Q}$, and $\mathbf{R}$, the components of which depend on the fundamental property tensors of the matrix (elastic, piezoelectric and dielectric), the shape of the inclusion/exclusion as well as its distribution in the matrix phase. From the above Eqs. (4.35) and (4.36) we can write the strain and electric field in the particle phase in terms of the microstructural tensors as:

$$\overline{\varepsilon}_{mn}^{(2)} = \varepsilon_{mn}^0 \quad - \quad \left[\mathrm{P}_{ijmn}^{(22)} \Delta L_{ijpq}^{(2)} + \mathrm{Q}_{kmn}^{(22)} \Delta e_{kpq}^{(2)} \right] \overline{\varepsilon}_{pq}^{(2)}$$
$$- \quad \left[\mathrm{P}_{ijmn}^{(22)} \Delta e_{pij}^{(2)} - \mathrm{Q}_{kmn}^{(22)} \Delta \kappa_{kp}^{(2)} \right] \overline{\phi}_{,p}^{(2)} \qquad (4.37)$$

and

$$\overline{\phi}_{,p}^{(2)} = \phi_{,p}^0 - \left[Q_{pij}^{(22)} \Delta L_{ijmn}^{(2)} + R_{pl}^{(22)} \Delta e_{lmn}^{(2)} \right] \overline{\varepsilon}_{mn}^{(2)}$$
$$- \left[Q_{pij}^{(22)} \Delta e_{kij}^{(2)} - R_{pl}^{(22)} \Delta \kappa_{lk}^{(2)} \right] \overline{\phi}_{,k}^{(2)} \tag{4.38}$$

where the microstructural tensors can be expressed in terms of the periodic Green's operators by,

$$P_{ijmn}^{(22)} = \sum_{\boldsymbol{\xi} \in \mathcal{R}^* - \{0\}} c^{(2)} H_{mnij}^s \left\langle e^{-i\boldsymbol{\xi} \cdot \mathbf{x}} \right\rangle^{(2)} \left\langle e^{i\boldsymbol{\xi} \cdot \mathbf{x}} \right\rangle^{(2)}, \tag{4.39}$$

$$Q_{kmn}^{(22)} = \sum_{\boldsymbol{\xi} \in \mathcal{R}^* - \{0\}} c^{(2)} \beta_{kmn}^s \left\langle e^{-i\boldsymbol{\xi} \cdot \mathbf{x}} \right\rangle^{(2)} \left\langle e^{i\boldsymbol{\xi} \cdot \mathbf{x}} \right\rangle^{(2)}, \tag{4.40}$$

$$R_{pl}^{(22)} = \sum_{\boldsymbol{\xi} \in \mathcal{R}^* - \{0\}} c^{(2)} \gamma_{pl}^s \left\langle e^{-i\boldsymbol{\xi} \cdot \mathbf{x}} \right\rangle^{(2)} \left\langle e^{i\boldsymbol{\xi} \cdot \mathbf{x}} \right\rangle^{(2)}. \tag{4.41}$$

Following are the equations for the effective elastic, piezoelectric and dielectric moduli for a general n-phase composite. The expressions for the effective moduli tensors for a two-phase composite can be found in the Appendix A of this paper. The above defined microstructural tensors are also termed as the equivalent Eshelby tensors for a periodic piezoelectric composite. The overall effective electromechanical material constants can be derived from the average strain and electric fields and are given by,

$$\widetilde{L}_{ijkl} = L_{ijkl}^{(n)} + \sum_{r=1}^{n-1} c^{(r)} (L_{ijmn}^{(r)} - L_{ijmn}^{(n)}) A_{mnkl}^{(r)} + \sum_{r=1}^{n-1} c^{(r)} (e_{pij}^{(r)} - e_{pij}^{(n)}) B_{pkl}^{(r)} \tag{4.42}$$

$$\widetilde{e}_{imn} = e_{imn}^{(n)} + \sum_{r=1}^{n-1} c^{(r)} (e_{ikl}^{(r)} - e_{ikl}^{(n)}) A_{klmn}^{(r)} - \sum_{r=1}^{n-1} c^{(r)} (\kappa_{ik}^{(r)} - \kappa_{ik}^{(n)}) B_{kmn}^{(r)} \tag{4.43}$$

$$\widetilde{\kappa}_{in} = \kappa_{in}^{(n)} + \sum_{r=1}^{n-1} c^{(r)} (\kappa_{ik}^{(r)} - \kappa_{ik}^{(n)}) b_{kn}^{(r)} - \sum_{r=1}^{n-1} c^{(r)} (e_{ikl}^{(r)} - e_{ikl}^{(n)}) a_{kln}^{(r)} \tag{4.44}$$

where $\mathbf{A}$ and $\mathbf{B}$ are the strain concentration tensors and $\mathbf{a}$ and $\mathbf{b}$ are the electric field concentration tensors. The explicit forms of the concentration

tensors are presented in Appendix A.

4.3.3 Calculating the vectors in Fourier space

To calculate the the properties of the effective electromechanical tensors, $\widetilde{\mathbf{L}}$, $\widetilde{\mathbf{e}}$, and $\widehat{\boldsymbol{\kappa}}$, we need to evaluate the equivalent vectors in Fourier space describing the microstructure of the given unit cell configuration. In the equations used to compute the microstructural tensors $\mathbf{P}$, $\mathbf{Q}$, and $\mathbf{R}$ (see Appendix B), we define the Fourier vectors in the reciprocal lattice as,
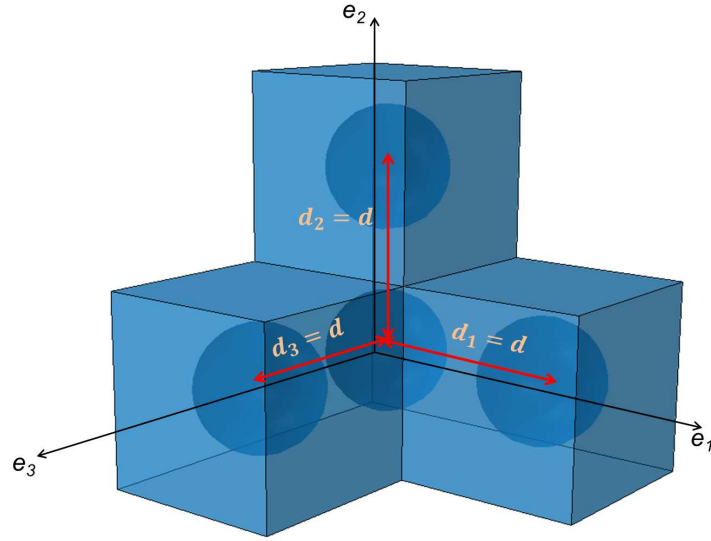
Figure 4.3: Schematic representation of the microstructure showing a cubic distribution of spherical pores.

$$\mathcal{R}^* = \{\boldsymbol{\xi} \,|\, \boldsymbol{\xi} = n_1\mathbf{G}_1 + n_2\mathbf{G}_2 + n_3\mathbf{G}_3,\, n_i \in \mathbb{Z}\} \tag{4.45}$$

with

$$\mathbf{G}_1 = 2\pi\frac{\mathbf{Y}_2 \wedge \mathbf{Y}_3}{\mathbf{Y}_1 \cdot (\mathbf{Y}_2 \wedge \mathbf{Y}_3)}, \ \mathbf{G}_2 = 2\pi\frac{\mathbf{Y}_3 \wedge \mathbf{Y}_1}{\mathbf{Y}_1 \cdot (\mathbf{Y}_2 \wedge \mathbf{Y}_3)}, \ \mathbf{G}_3 = 2\pi\frac{\mathbf{Y}_1 \wedge \mathbf{Y}_2}{\mathbf{Y}_1 \cdot (\mathbf{Y}_2 \wedge \mathbf{Y}_3)} \tag{4.46}$$

Here, the base vectors $\mathbf{Y}_i$ ($i = 1, 2, 3$) characterize the periodic distribution of the fibers in the real space (i.e., in $\mathbb{R}^3$). The expressions for the cubic and

64

square distribution of the pores as shown in Figs. 4.3 and 4.4 are given by;

$$\mathbf{Y_1} = d(1,0,0); \ \mathbf{Y_2} = d(0,1,0); \ \mathbf{Y_3} = d(1,0,0) \quad (4.47)$$

$$\mathbf{Y_1} = d(1,0,0); \ \mathbf{Y_2} = d(0,1,0); \ \mathbf{Y_3} = \infty \quad (4.48)$$

where, the rectangular Cartesian basis $\{\mathbf{e}_i\}$ denotes the frame of reference in the real space, $d_3 \to \infty$, d_1, and d_2, serving to describe the in-plane distribution of the long cylindrical pores, as depicted by Fig. 4.4(a). For the case of the spherical pores in a cubic distribution, we have $d_1 = d_2 = d_3 = d$, which describes the distribution of the pores in the three Cartesian coordinates (see Fig. 4.3). The specialization of expressions (4.47) and (4.48) to the case of square distribution of cylindrical pores, hexagonal distribution of cylindrical pores and cubic distribution of spherical pores is provided in Appendix B.
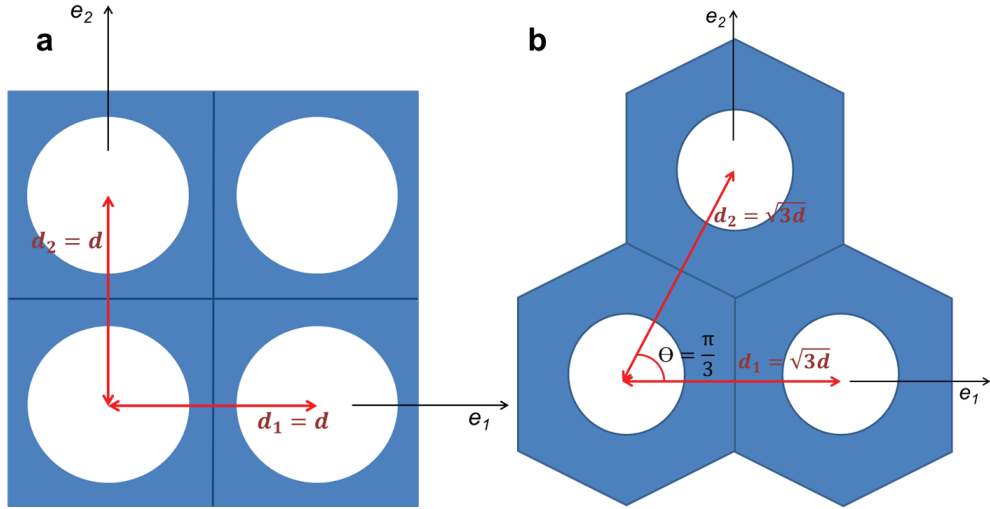
Figure 4.4: Schematic representation showing the in-plane fiber distribution and geometrical parameters of: (a) a square distribution of long cylindrical pores, and (b) a hexagonal distribution of cylindrical pores.

4.4 Three-dimensional finite-element model for predicting the fundamental properties and figures of merit of piezoelectric composite materials

4.4.1 Aspects of the three-dimensional finite-element model

A unit cell based three-dimensional finite element model is invoked in the present study where in the complete electromechanical response of an infinitely large periodic piezoelectric composite material is captured by characterizing the electromechanical behaviour of a unit cell. Since the unit cell is designed to capture the response of the entire composite material certain boundary conditions must be enforced to make sure that the deformation and electric potential of a unit cell are compatible across its boundaries with the adjacent unit cells [60]. In the present study, two types of three-dimensional unit cells were constructed in order to characterize the electromechanical response of piezoelectric materials with long cylindrical pores (1-3 type) and with closed spherical pores (3-0 type). In order to maintain the periodicity of the electromechanical loading across the boundary of the unit cell the following boundary conditions are imposed:

(i) Periodicity in the $1-\text{direction}$ is given by $: P^R - P^A = P^S - P^B$; $P^{RR} - P^{AA} = P^{SS} - P^{BB}$; $P^V - P^A = P^W - P^B$; $P^{VV} - P^{DD} = P^{WW} - P^{CC}$; $P^{XM} - P^A = P^{XP} - P^B$.

(ii) Periodicity in the $2-\text{direction}$ is given by $: P^T - P^D = P^U - P^A$; $P^{TT} - P^{DD} = P^{UU} - P^{AA}$; $P^{WW} - P^C = P^W - P^B$; $P^{YP} - P^C = P^{YM} - P^B$; $P^{XM} - P^A = P^{XP} - P^B$.

(iii) Periodicity in the $3-\text{direction}$ is given by $: P^{UU} - P^{AA} = P^U - P^A$; $P^{SS} - P^{AA} = P^S - P^A$; $P^{ZP} - P^{AA} = P^{ZM} - P^A$.

By subjecting a particular unit cell to a set of controlled mechanical and

electrical loading conditions and characterizing its response, all 45 material constants of a piezoelectric composite can be determined. The main feature of this three-dimensional finite-element model is that both types of unit cells are subject to a common set of electrical and mechanical loading conditions in order to determine the components of the electroelastic moduli of a given composite.
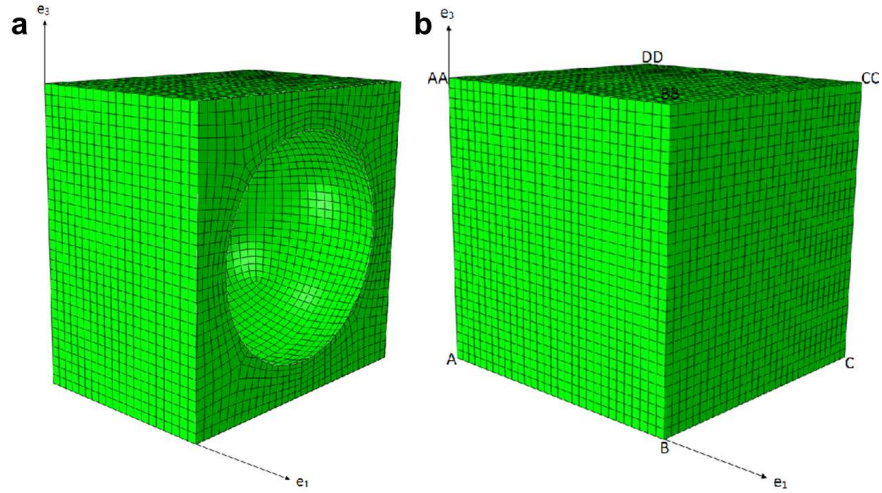
Figure 4.5: The finite element mesh used to model the properties of a (3-0) type porous piezoelectric system with spherical porosity - (a) a cross-section of unit cell showing the details of the mesh on the boundary of the spherical pore, and (b) the mesh on the surface of the unit cell showing the location of the masters nodes on the vertices of the unit cell.

The finite-element analysis for the unit cell is carried out using commercially available software (ABAQUS). Eight-node linear piezoelectric brick (C3D8E) elements are used to mesh the unit cell. Each node is allowed a total of four degrees of freedom (i.e., 1, 2, 3) and one electric potential degree of freedom (i.e., 9). The nodes located on the vertices of the unit cell, $A(AA), B(BB), C(CC), D(DD)$, are designated as master nodes, and P refers to all the four degrees of freedom (i.e., $P = 1, 2, 3, 9$). The constraint equations are such that they allow the master nodes to control the overall behaviour of the unit cell. All loads (mechanical and electrical) are applied to the master nodes only. The master node A is fixed and electrically grounded for all simulations to prevent rigid body motion ($P^A = 0$ for $P = 1, 2, 3, 9$).

67

A detailed description of the constraint equations and the method used to determine all 45 (21 elastic, 15 piezoelectric, and 6 dielectric) independent electroelastic constants has been given in the Appendix of Ref. [60]. Details of the finite element mesh created for modeling a piezoelectric material with spherical porosity are presented in Fig. 4.5

4.4.2 Piezoelectric figures of merit

In order to assess the performance characteristics of devices made from piezoelectric composites, several figures of merit are generally identified. In order to assess the suitability of porous piezoelectric materials for applications such as in hydrophones, the following four figures of merit are typically considered: the piezoelectric coupling constant (k_t), the acoustic impedance (Z), the piezoelectric charge coefficient (d_h), and the hydrostatic figure of merit $(d_h \cdot g_h)$.

In the following subsections, the Voigt contracted notation is used to express the four figures of merit identified in the present study. According to this notation the indices, $11 = 1$, $22 = 2$, $33 = 3$, $23 = 4$, $13 = 5$, $12 = 6$. Therefore $L_{1111} = C_{11}$, $L_{3333} = C_{33}$, $L_{2323} = C_{44}$, etc.

4.4.2.1 Piezoelectric coupling constant

The thickness-mode piezoelectric coupling constant, $k_t = \sqrt{1 - C_{33}^E/C_{33}^D}$ (in the longitudinal extension mode) describes the efficiency of conversion between the electrical and mechanical energy by the piezoelectric material. The ratio of the stored converted energy of one kind (mechanical or electrical) to the input energy of the second kind (electrical or mechanical) is defined as the square of the coupling coefficient. Materials with larger coupling constants (~ 1) are typically more desired.

4.4.2.2 Acoustic impedance

The acoustic impedance (Z) given by $Z = \sqrt{C_{33}^D \rho}$, represents the overall acoustic load at the interface between the hydrophone/device and the environment, where ρ is the effective density of the material. Good impedance matching between the device and the surrounding media is essential to enhance the performance of the hydrophone. Since porous piezoelectric materials have lower densities than pore-free materials they are targeted for use in hydrophone applications. The effective density is calculated using the formula, $\rho = c^{(1)} \rho^{(1)} + c^{(2)} \rho^{(2)}$, where $c^{(1)}$, $c^{(2)}$ are the volume fractions of the two phases and $\rho^{(1)}$, $\rho^{(2)}$, are their respective densities.

4.4.2.3 Hydrostatic strain coefficient

The hydrostatic (or piezoelectric) strain coefficient, $d_h = d_{31} + d_{32} + d_{33}$, is the measure of the effective strength of electromechanical coupling in a piezoelectric material. It is especially important in the conversion of mechanical loads (under hydrostatic loading) to electrical signals (in a given direction, e.g., 3). It describes the polarization that results from a change in hydrostatic stress. To enhance the sensitivity of the hydrophone to the detection of sound, a large value for the piezoelectric charge coefficient is desired. The piezoelectric strain coefficient ($\mathbf{d}$) can be evaluated from the piezoelectric stress coefficient ($\mathbf{e}$) as, $d_{ijk} = e_{imn} S_{mnjk}^E$, where $\mathbf{S^E}$ is the elastic compliance tensor.

4.4.2.4 Hydrostatic figure of merit

The hydrostatic figure of merit, $d_h \cdot g_h$ defines the hydrophones' sensing and actuating capability. The sensitivity of a hydrophone depends primarily on the voltage that is produced by a hydrostatic pressure wave. The hydrostatic voltage coefficient, g_h, relates the electric field across a transducer to the applied hydrostatic stress, and is therefore an important parameter for evaluating piezoelectric materials for use in hydrophones. The g_h coefficient is related to the d_h coefficient by the permittivity constant (κ_{33}) as $g_h = d_h / \kappa_{33}$. Porous piezoelectric materials usually demonstrate higher values for the hydrostatic

figure of merit than fully dense monolithic piezoelectric materials or pore-free piezo-ceramic composites.

The results obtained from the analytical model and their relationship to the results obtained from the finite element models are discussed in the following section 4.5.

4.5   Results and discussion

The analytical model developed in the present study is invoked to predict the complete set of elastic, dielectric and piezoelectric properties of two solid (3-1 type) fiber composite systems and three porous ((3-0 type) and (3-1 type)) piezoelectric material systems (that exhibit varying degrees of anisotropy) over a wide range of volume fractions. The predictions of the analytical model developed in the present study are compared to that of an analytical model developed earlier for piezoelectric composites with transversely isotropic constituents and a three-dimensional finite element model developed in the present study for piezoelectric composites with anisotropic constituents. The properties of the piezoelectric materials considered in the present work are given in Table A.1.

4.5.1   Comparison of the fundamental electromechanical properties predicted by the analytical model with an existing analytical model for piezoelectric composites with transversely isotropic constituents

The electro-elastic moduli predicted by the analytical model developed in the present study are compared to that of the asymptotic homogenization-based analytical model developed by Bravo-Castillero et al. [2], which provides explicit expressions for the electromechanical properties of $3-1$ type piezoelectric fiber composites with transversely isotropic consituents. (The model developed by Bravo-Castillero et al. is applicable to fiber composites with a square distribution of fibers.) Two material systems, i.e., a ceramic-ceramic (Barium

Titanate(matrix) - PZT-7A (fiber)) and a polymer-ceramic (PVDF (matrix) - PZT-7A (fiber)) were chosen for the analysis.
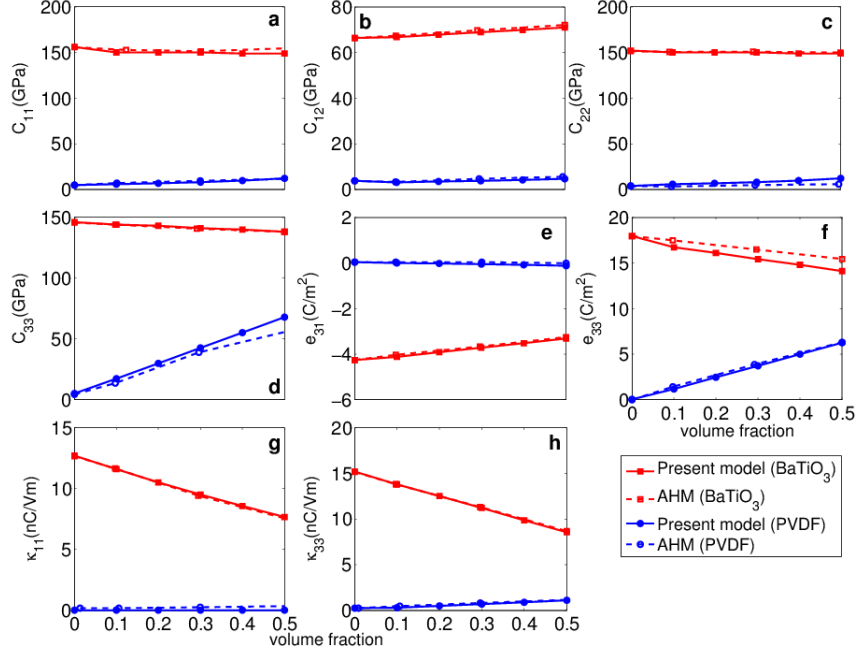
Figure 4.6: The variation of the electromechanical properties of a (3-1) type piezoelectric composite with fibers aligned in the direction of poling with volume fraction predicted by the analytical model developed in the present study and the asymptotic homogenization-based model (AHM) [2] in model Barium Titanate - PZT-7A and PVDF - PZT-7A systems.

The two material systems were chosen to represent a range of material systems where the constituent phases have relatively similar electromechanical properties (i.e., Barium Titanate - PZT-7A) as well as systems where one phase is considerable stiffer than the other phase (i.e., PVDF - PZT-7A). Overall the electromechanical properties predicted by the analytical model developed in the present study compare well with those predicted by the model presented by Bravo-Castillero et al. [2] (Fig. 4.6) for both the composite material systems. The largest difference between the predicted properties from the two models was observed for the longitudinal stiffness constant C_{33} in the PVDF - PZT-7A system and found to be about 17% at 50% fiber volume fraction. The elastic properties in the "transverse" direction C_{11} and C_{22} show only a 3% difference at 50% fiber volume fraction.

71

4.5.2 Comparison of the fundamental electromechanical properties predicted by the analytical model and the finite element model

While prior studies have been successful in estimating the overall properties of composites with transversely isotropic particle and matrix phases, the model developed in the present study can predict the components of the effective moduli for any anisotropic periodic piezoelectric composite. For e.g., Dunn and Taya [49] and Mikata [52] have presented models that give explicit solutions for the components of equivalent Eshelby tensor for transversely isotropic phases but do not give closed-form solutions for anisotropic inclusions. Also their works specifically dealt with single inclusions in infinite media, which is the equivalent Eshelby problem for piezoelectric materials. An external scheme (in their case the Mori-Tanaka mean field approach) has to then be applied to the solution for a single inclusion to predict the effective properties across finite volume fractions. On the other hand, our analytical model (based on Suquet estimates [95]) take into account the distribution of the particle in the matrix phase and give solutions for effective moduli at finite volume fractions as well. That the analytical model developed in the present study yields accurate predictions for all the effective electromechanical constants for a periodic piezoelectric composite is demonstrated in the following sections. However, we note that this model does not take into account any interactions between particles in adjacent unit cells and the accuracy of the model predictions at the percolation limit has not been assessed.

Fig. 4.7 presents a comparison of the elastic constants predicted by the analytical model and the finite element model developed in the present study and their variation with volume fraction of porosity for a model anisotropic piezoelectric system (i.e., barium sodium niobate single crystal which exhibits mm2 crystal symmetry). It is evident that the analytical model works well in predicting all the independent constants with the difference between the analytical model predictions and the finite-element model predictions being less than 4% for all constants. This demonstrates the utility of the analytical
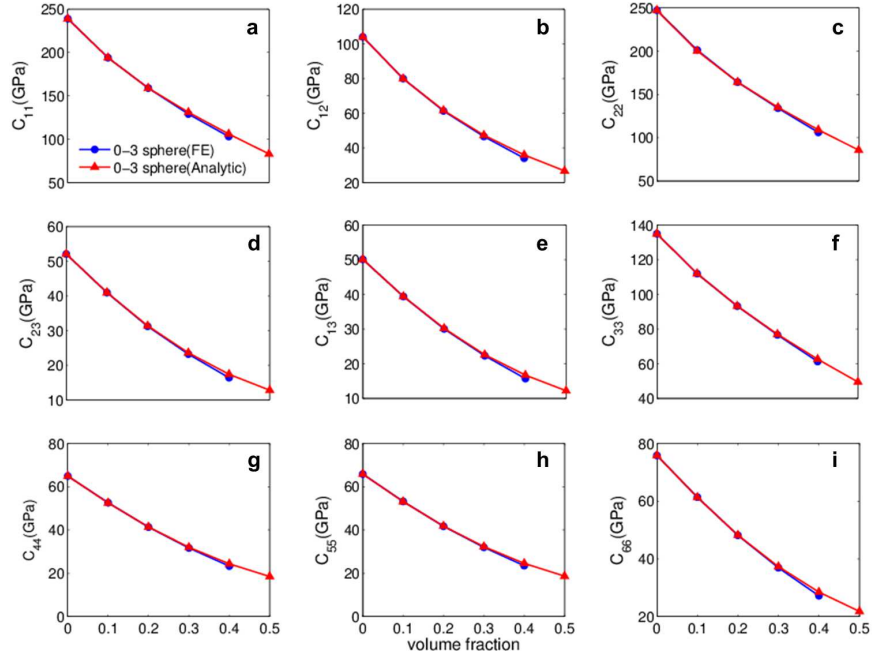
Figure 4.7: The variation of the elastic properties of a (3-0) type porous piezoelectric material with porosity volume fraction predicted by the analytical model and the finite element model in a model barium sodium niobate single crystal piezoelectric system.

model developed in the present study where even a linear approximation for the stress and electric field polarizations yields fairly accurate results for predicting the elastic properties of the piezoelectric composite.

A comparison between the overall piezoelectric and dielectric constants obtained from the analytical and finite-element model is presented in Fig. 4.8. Here again it is observed that the there is very good agreement between the predictions given by the two models. As expected, the piezoelectric constants (e_{15}, e_{24}, e_{31} and e_{32}) and the dielectric constants (κ_{11}, κ_{22}, and κ_{33}) show decreasing trends with increase in porosity volume fraction.

4.5.3 Comparison of the figures of merit predicted by the analytical model and the finite element model

To demonstrate the applicability of the current analytical model in predicting the properties of piezoelectric composite materials that belong to several
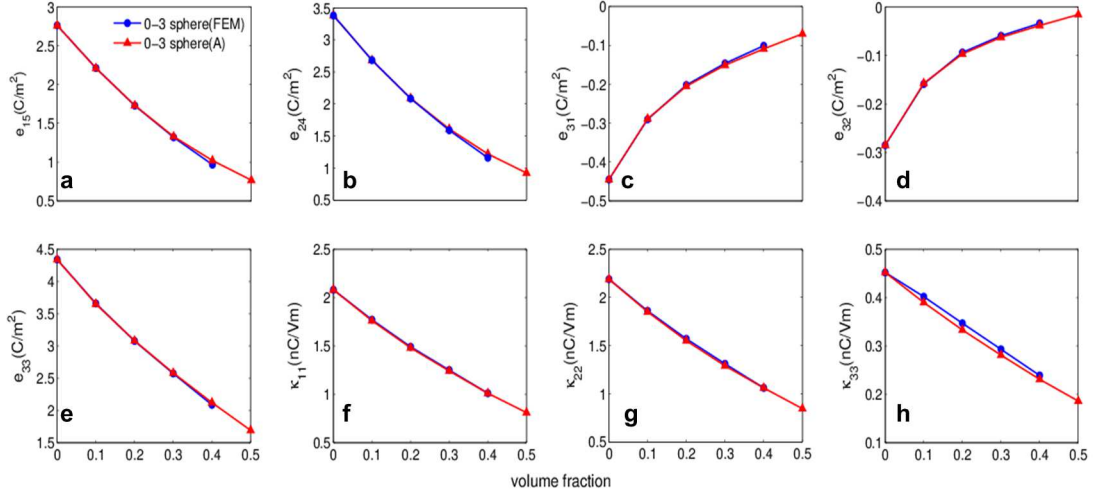
Figure 4.8: The variation of the piezoelectric and dielectric properties of a (3-0) type porous piezoelectric material with porosity volume fraction predicted by the analytical model and the finite element model in a model barium sodium niobate single crystal piezoelectric system.

crystal symmetry classes, the analytical model was invoked for three model piezoelectric single crystal material systems, each with spherical and cylindrical porosity. Subsequently, four figures of merit that are important for practical applications of porous piezoelectric materials were also identified for a range of porosity volume fractions. In general, all the four figures of merit are well-predicted by the analytical model and showed a high degree of correspondence when compared with the results of the finite-element model (with the maximum differences between the predictions of the analytical model and the final element model being less than 2%). Of particular interest to note are the values for the piezoelectric strain coefficient(d_h) and the hydrostatic figure of merit ($d_h \cdot g_h$) for the case of piezoelectric materials with spherical porosity in all three materials (Fig. 4.9). The steep increase in the values of these figures of merit with increasing porosity had been observed earlier by Iyer and Venkatesh [64, 63], making piezoelectric ceramics with spherical porosity useful for hydrophone sensing applications.
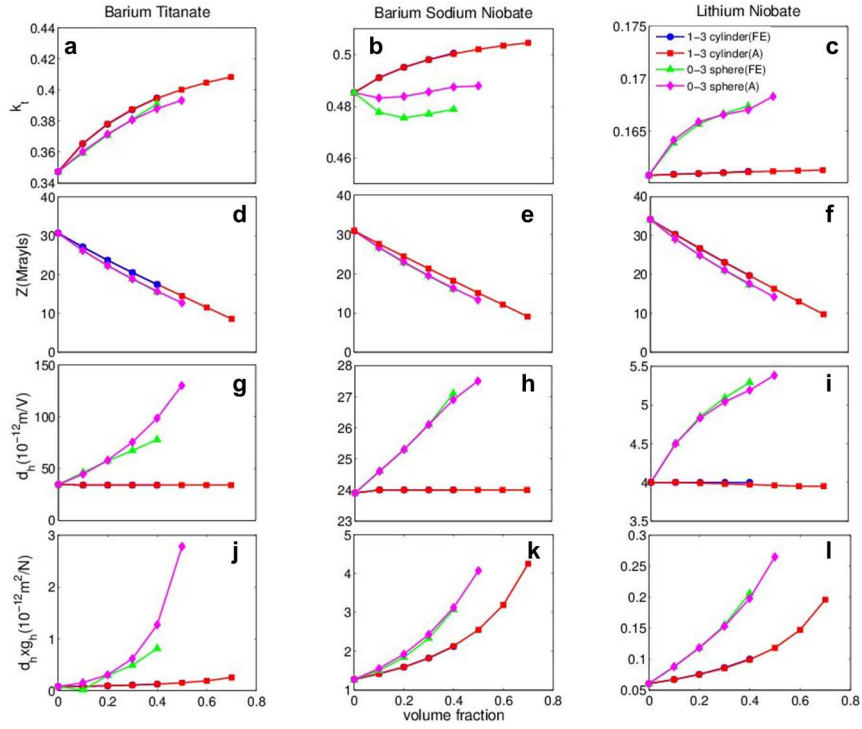
Figure 4.9: The variation of select figures of merit in (3-0) type and (3-1) type porous piezoelectric materials with porosity volume fraction predicted by the analytical model and the finite element model in three model single crystal piezoelectric systems.

4.6 Conclusions

Several analytical models have been developed to predict the fundamental properties of select classes of piezoelectric composite materials such as those that exhibit transverse isotropy. Furthermore, finite element based numerical models have been developed to predict the electromechanical properties of piezoelectric composites with anisotropic constituents. However, an analytical model that provides explicit closed-form solutions to the most general problem of a piezoelectric composite with anisotropic particulate constituents is not yet available.

In the present study, an analytical framework, based on the homogenization methods developed by Suquet [95], has been developed to predict the effective properties of periodic anisotropic particulate composites. Expressions have been provided for the effective moduli tensors of n-phase composites

based on the respective strain and electric field concentration tensors. Previous analytical models developed by Dunn and Taya [49] and Mikata [51] provide closed-form expressions for the electromechanical properties of single inclusions in infinite transversely isotropic media. Hence, the analytical model presented in this study takes their work forward by examining the microstructure of the periodic composite and incorporating a scheme that results in the prediction of the overall electromechanical constants of piezoelectric composites for finite volume fractions. Furthermore, in the present study, no dependence on material symmetry is assumed when deriving the equivalent Eshelby tensors for the periodic composite.

By taking into account the shape and distribution of the inclusion and by invoking a simple numerical procedure, solutions for the electromechanical properties of a general anisotropic inclusion in an anisotropic matrix are obtained. While analytical expressions are provided for composites with spherical and cylindrical inclusions, numerical evaluation of integrals over the composite microstructure is required in order to obtain the expressions for a general ellipsoidal particle in a piezoelectric matrix. It can also be shown that the approximation that the polarization fields be piece-wise continuous yield Hashin-Shtrikman type bounds for the effective moduli tensors.

The predictions of the analytical model developed in the present study for the electroelastic moduli of piezoelectric composites demonstrate excellent agreement with the results obtained from three-dimensional finite-element models for several piezoelectric systems that exhibit varying degrees of elastic anisotropy.

However, the analytical model developed in this study has some limitations. The interactions between particles at high volume fractions are not taken into consideration. Furthermore, this model is not applicable to composites with a random distribution of particles in the matrix phase. Nevertheless, the theory is general in terms of predicting the overall electromechanical properties for periodic piezoelectric composites with n-phases and anisotropic fundamental property tensors.

Band Gaps in Bravais Lattices Inspired Periodic Cellular Materials and The Effect of Relative Density and Strain Fields

5.1 Introduction

Topology-optimized periodic cellular materials have a promising potential in active sound attenuation and filtering devices due to their unique frequency- and topology-dependent sound wave dispersion and transmission characteristics. Lattice (periodic cellular) materials, as a result of their periodic architecture, give rise to geometric impedance mismatch which, in turn, causes complex destructive wave interference phenomena over specified frequency bands (i.e. band-gaps or stop-bands) [100, 73]. At these bands or frequencies wave transmissibility is diminished and its propagation is blocked. *Phononic band-gap* (PBG) materials, due to their ability to control the propagation of mechanical waves, are increasingly being considered as potential candidates to perform as low frequency phononic crystals and metamaterials in radar, sonar, wave guiding, wave modulation and isolation applications. In addition, this phenomenon of barriers (band-gaps) in the frequency spectrum has been especially targeted for its potential towards being used in sound filtering in the audible range particularly in today's environment of ever increasing sound pollution.

The interest in cellular based PBG materials is further amplified as they can be engineered at the micro- or meso-scales to exhibit novel and unique mechanical properties, not readily exhibited by monolithic existing materials.

Multiple efforts have been exerted to understand and subsequently engineer PBG cellular materials.

In general, these efforts often aimed to highlight the relationship between cellular topological features in terms of fundamental building blocks of periodic lattice structures (i.e., unit cells) and observed band-gaps (e.g. in order to design lattices with specific vibration isolation characteristics [101]) under out-of-plane and in-plane wave propagation.

For out-of-plane elastic wave propagation, band gaps and directional characteristics have been investigated in hexagonal [102] and grid-like lattices [103], while for in-plane elastic waves, Kagome, hexagonal, triangular, and grid-like lattice structures were studied [104, 105]. These efforts highlighted that band-gaps and directionality vary widely among the different lattices, are dependent on topological features and speed of sound in constitutive materials, and can be potentially tuned by composing cellular lattice materials from constituents with contrasting properties (densities or speed of sounds) or by altering the lattice topology. Accordingly in this study, the wave dispersion characteristics have been studied in honeycomb, triangular and tetragonal structures Fig. 5.1.

More recent efforts have focused on optimizing and tuning the response of PBG lattice materials. In this regard, Sigmund and Jensen [101] showed that the band-gaps in a given periodic structure comprised of two-phase composites materials, can be optimized to exhibit enhanced band-gap properties. Kushwaha et al. [72] presented full band-gap structure calculations for elastic composites tuned to applications where a vibrationless environment was desired. Bertoldi and Boyce [106, 107] studied the potential for using instabilities in tuning the wave propagation and band gaps in periodic structures. Bertoldi and Boyce [106, 107] subjected periodic elastomers to large strain deformations and studied the shift in the band-gap as a result of the induced buckling modes. Their results show that deformation patterns due to buckling can drastically shift the band-gaps in a sudden but controlled manner. Khelif et al. [108, 109] obtained numerical results showing PBG's in quartz cylinders embedded in an epoxy matrix and found that band-gaps can be tuned by
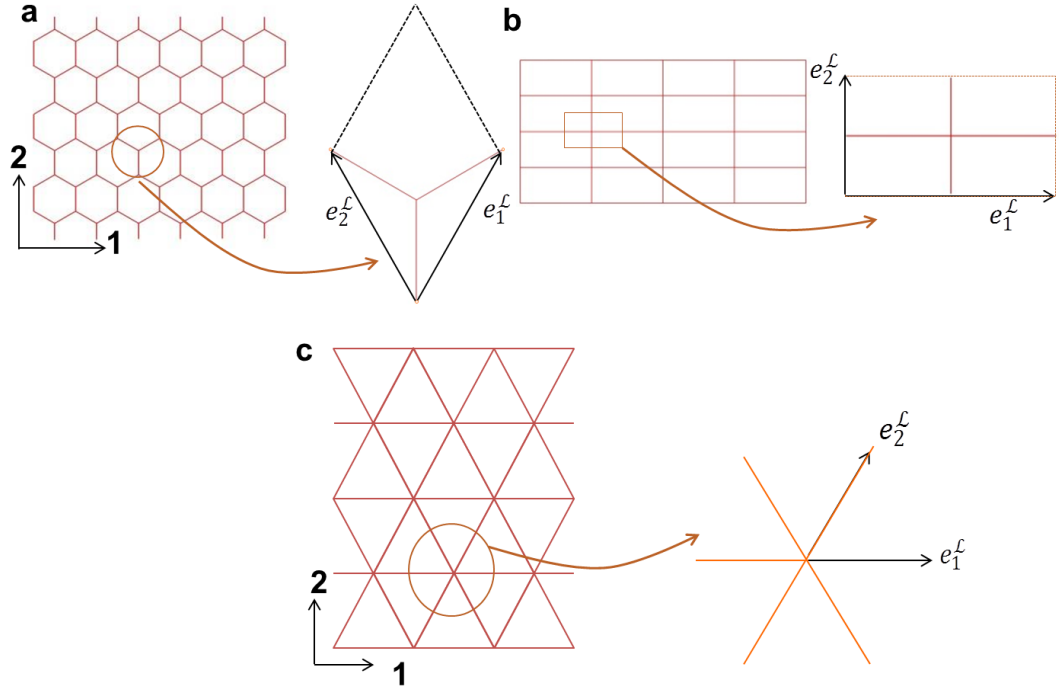
Figure 5.1: Schematic illustration of a hexagonal lattice - (a) Highlights the unit-cell within the hexagonal lattice system and its corresponding unit vectors (b) Highlights the unit-cell within the tetragonal lattice system and its corresponding unit vectors (c) Highlights the unit-cell within the triangular lattice system and its corresponding unit vectors.

controlling the spacing between the quartz cylinders.

From the above mentioned literature review it can be established that architectured periodic lattice materials, by virtue of their periodic spatial architecture, exhibit wave dispersion characteristics, direction dependent wave propagation behavior, frequency dependent phononic band-gaps [100, 73, 110], and therefore, can guide, steer, transmit or block sound and elastic waves [102, 111, 112]. Moreover, lattice based metamaterials/phononic crystals can provide characteristics and operate at frequencies not always achievable with monolithic metamaterials; in particular lattice based metamaterials can operate at very low frequencies (sub Hz to KHz), which are particularly important for radar and sonar applications and in situations where long range wave penetrability is essential.

In order to capitalize on the potential of architectured materials and to

use them in the aforementioned applications, they need to be designed to deliver, precise and tunable pass-gap frequency characteristics, wave dispersion and directionality characteristics suited to the requirement of the given device. However, the extent to which microstructural features such as solid relative density influences the fundamental acoustic properties of such phononic materials is at present not fully understood. Accordingly, this work aims to provide,

1. A better understanding of the effects of relative density on the band gaps and directional wave characteristics in three chosen lattice configurations.

2. Establish the knowledge base necessary to realize application-tailored band-gaps and wave characteristics through tuning the lattice topology and relative density of architectured lattice materials.

The remainder of this study has been organized as follows; Section 5.2 elaborates on the theoretical background necessary to study the evolution of the frequency band gaps in cellular solids. The founding work of Brillouin is explained in context of Bloch's wave theory, specialized to the case of cellular composites. Section 5.3 discusses the results and discussions from the study of Bloch wave analysis of cellular solids. Finally the conclusions and the path to future advancements in the area of Bloch wave analysis of cellular solids, is discussed in the Section 5.4.

5.2 Technical Approach and Theoretical Background: Characterizations of Dispersion, Band Gaps and Directionality in Lattices

Frequency dependent band-gap phenomenon in PBG materials is fundamentally similar to electron propagation and electron band-gaps in solid state physics. Therefore the techniques of Brillouin zones and Bloch waves [71] which stem from the realm of solid state physics have been extensively utilized to investigate wave propagation in architectured (lattice) phononic crystals (e.g.[73, 113]).

Similarly, in this work, wave propagation in lattice-based systems is studied and characterized using the well-established Bloch's wave theorem in conjunction with finite element computations. Bloch's wave theorem is implemented in this work following the work outlined in Refs. [73, 102, 71, 114]. The implementation of which is described in the following subsections.

5.2.1 Unit cell and lattice vectors identification

A unit cell, by definition, is the smallest representative element of a large periodically repeating lattice system through translations along the lattice base vectors. To illustrate, a periodic hexagonal lattice and its corresponding unit cell are shown in Fig. 5.2. In this example, the lattice base vectors are described as $\boldsymbol{e_1^L}$ and $\boldsymbol{e_2^L}$ such that the superscript L refers to lattice space. Here, bold letters are used to represent vector quantities. Using the lattice space vectors any point in the lattice structure can be located. For instance, the location of point p in cell n_1, n_2 can be defined as,

$$\boldsymbol{\rho_p(n_1, n_2)} = \mathbf{r_p} + n_1 \boldsymbol{e_1^L} + n_2 \boldsymbol{e_2^L} \tag{5.1}$$

where $\mathbf{r_p}$ represents the location of point p with reference to the unit cell whose n_1 and n_2 components are equal to zero.

5.2.2 Bloch's wave theorem and its application to the unit-cell

Without any loss of generality, the hexagonal lattice is used to illustrate the process of implementing Bloch's wave theorem. Bloch's theorem states that the displacement of a point p in the reference unit cell due to a wave propagating through it at a frequency ω can be stated as,

$$\mathbf{u(r_p)} = \mathbf{u_{p_o}} e^{(i\omega t - \mathbf{k} \cdot \mathbf{r_p})} \tag{5.2}$$
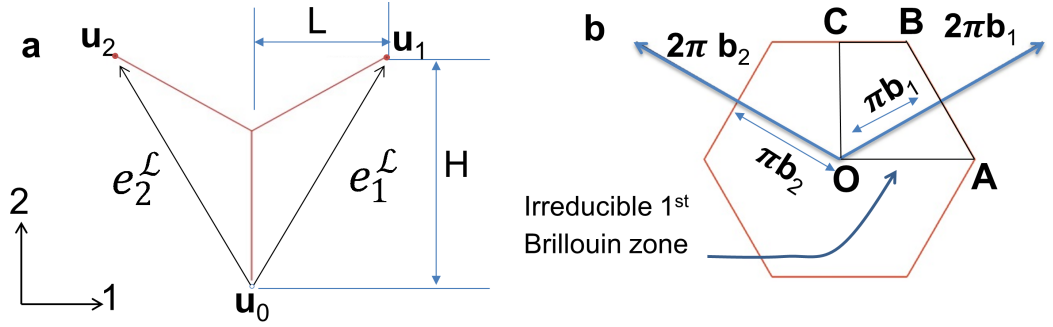
Figure 5.2: Schematic showing the lattice space, reciprocal space and Brillouin zone for a honeycomb lattice with (a) representation of the lattice space and unit cell, (b) reciprocal space and 1st Brillouin zone in the physical space.

such that p_o is the origin of the reference cell, $\mathbf{u_{p_o}}$ is the amplitude of the propagating wave and $\mathbf{k}$ is the wave vector. Based on Bloch's theory, the displacement of a point p in the cell n_1, n_2 whose location is $\rho_p(n_1, n_2)$ can be expressed as,

$$\mathbf{u_{r_p}} = \mathbf{u(r_p)}e^{\mathbf{k} \cdot (\rho_p - r_p)} = \mathbf{u(r_p)}e^{(k_1 n_1 + k_2 n_2)} \tag{5.3}$$

where the right most term is a result of the relations $\mathbf{k} \cdot \boldsymbol{e_1^L} = k_1$ and $\mathbf{k} \cdot \boldsymbol{e_2^L} = k_1$, since the wave vector is defined in the lattice reciprocal space as is shown below (Eq. (5.3)). This equation accounts for wave dispersion and attenuation in the lattice structure through the wave vector $\mathbf{k}$. This assumption satisfies Bloch's theorem since it inherently assumes that a proportionate change in wave amplitude due to dispersion and attenuation from cell to cell does not depend on the location of the cell within the periodic system [73].

5.2.3 Dispersion relations and free wave motion

The aforementioned subsections provided the foundation for determining the periodic boundary conditions that accommodate dispersive behavior across a cell. These boundary conditions are implemented into the elastodynamic equilibrium equations to result in the dispersion governing equations that implicitly relate the wave frequency to the wave vector $\mathbf{k}$. The elastodynamic equilibrium equations are solved using finite element computations in ABAQUS, for

82
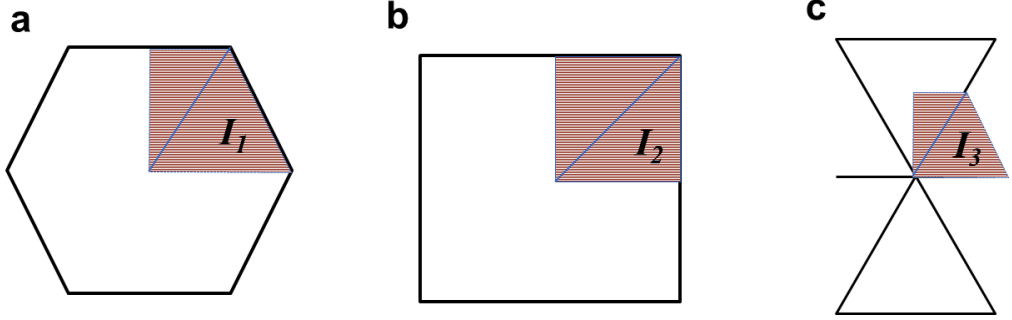
Figure 5.3: Schematic showing the first Brillouin zones and irreducible first Brillouin zones for (a) Hexagonal unit cell with irreducible first Brillouin zone represented by I_1, (b) Tetragonal unit cell with irreducible first Brillouin zone represented by I_2 and (c) Triangular unit cell with irreducible first Brillouin zone represented by I_3

an isotropic material (steel, E = 200 GPa, ν = 0.33) where damping is assumed to be negligible. Accordingly, the elastodynamic equilibrium equations are written as,

$$\left(\mathbf{K} - \omega^2 \mathbf{M}\right) \mathbf{u} = \mathbf{f} \tag{5.4}$$

where $\mathbf{u} = [\mathbf{u_0}, \mathbf{u_1}, \mathbf{u_2}, \mathbf{u_i}]^{\mathrm{T}}$ and $\mathbf{f} = [\mathbf{f_0}, \mathbf{f_1}, \mathbf{f_2}, \mathbf{f_i}]^{\mathrm{T}}$ are the nodal displacements and forces vectors, respectively. $\mathbf{K}$ and $\mathbf{M}$ are the element stiffness and mass matrices for the unit cell, respectively. ω represents the natural frequencies of the system which are equal to the number of degrees of freedom. Force and displacement vectors are expressed in terms of boundary and non-boundary degrees of freedom to facilitate applying the Bloch's theorem boundary conditions. Substituting the force and displacement vectors in Eq. (5.4) results in,

$$\left(\mathbf{K_r} - \omega^2 \mathbf{M_r}\right) \mathbf{u_r} = 0. \tag{5.5}$$

In Eq. (5.5), $\mathbf{K_r}$ and $\mathbf{M_r}$ are the reduced element stiffness and mass matrices for the unit cell and are functions of (k_1, k_2) and $\mathbf{u_r}$ is the reduced displacement vector $\mathbf{u_r} = [\mathbf{u_0}, \mathbf{u_i}]^{\mathrm{T}}$. Symmetry of the first Brillouin zone can be exploited such that only the irreducible part of the first Brillouin (Fig. 5.3) zone needs to be probed. To demonstrate, the first eigenmode surface $\omega_1(k_1, k_2)$ for the unit cell shown in Fig. 5.3(a) is obtained and presented in Fig. 3(a) in terms of the (ξ_1, ξ_2) representation of (k_1, k_2) (i.e. in the physical space following Eq.

(5.4)). This figure has two planes of symmetry along the 1 and 2 axes which are the planes of symmetry of the irreducible first Brillouin zone. Surfaces defined by $\boldsymbol{\omega} = \boldsymbol{\omega}(k_1, k_2)$ are the phase constant surfaces or dispersion surfaces. Each dispersion surface defines the dispersion characteristics and frequency-wave number relations for a particular mode. The following subsection describes the implementation of Bloch's wave theorem using a finite-element code to determine band-gaps in cellular solids. In the present study the first 10 eigen-frequencies have been obtained for each phase constant or dispersion surface.

5.2.4   Implementation of Bloch's wave theorem

The eigenvalue problem, Eq. (5.5), is used to define the band gap structure of periodic architectured lattices by varying k_1 and k_2 along the perimeter of the irreducible 1st Brillouin zone and solving Eq. (5.5). In order to imple-ment the periodic constraint equations in the commercially available software, ABAQUS, we start with modeling the honeycombs as an assembly of rigidly connected beams with three degrees of freedom (1, 2 and 6 in ABAQUS con-vention).

In accordance with Bloch's theorem, periodicity constraint equations that connect the unit-cell's generalized displacements, in addition to equilibrium conditions can then be written as (Fig. 5.2):

$$\mathbf{u_1} = \mathrm{e}^{k_1}\mathbf{u_0}$$
$$\mathbf{u_2} = \mathrm{e}^{k_2}\mathbf{u_0} \tag{5.6}$$

and

$$\mathbf{f_1} = -\mathrm{e}^{k_1}\mathbf{f_0}$$
$$\mathbf{f_2} = -\mathrm{e}^{k_2}\mathbf{f_0} \tag{5.7}$$

The solutions to Eq. (5.5) are the eigenfrequencies of the periodic cellular lattices and correspond to the resonant frequencies of the structure. In order to obtain the complete dispersion characteristics of the lattice, two out of the
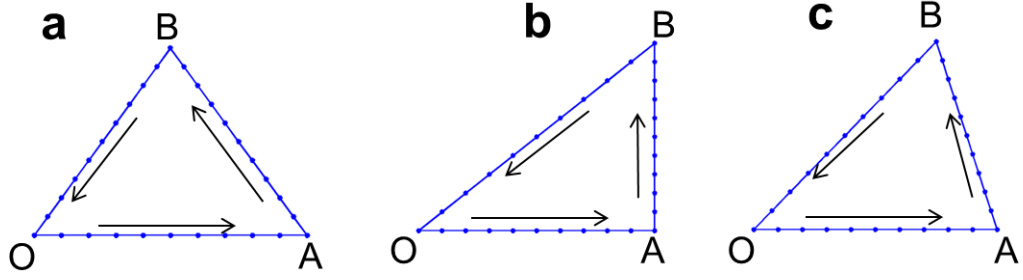
Figure 5.4: Schematic showing the contours along the perimeter of the irreducible first Brillouin zones for (a) Hexagonal unit cell , (b) Tetragonal unit cell and (c) Triangular unit cell.

three unknowns, k_1, k_2, ω have to be defined. In our case we define k_1, k_2 and solve for ω. For the purpose of obtaining the frequency band-gaps in our analyses we further assume that wave motion occurs without attenuation. For this purpose we then assign k_1, k_2 as pairs of imaginary numbers ($k_1 = i\varepsilon_1$, $k_2 = i\varepsilon_2$). The complete solution is thus obtained by varying k_1 and k_2 within the cellular structure to obtain, $\omega = \omega(k_1, k_2)$ as illustrated in Fig. 5.3. For the purpose of saving computational costs, the evaluation of the dispersion diagrams can be significantly reduced by exploiting the symmetry of the first Brillouin zone (FBZ) (Fig. 5.3), which is determined based on the symmetry of the cellular solid. A smaller zone within the FBZ can further be exploited to study phase constant surfaces such that variation of the **k**-vector is only examined along the outer perimeter of the irreducible first Brillouin zone (IR-FBZ) (Fig. 5.4). Note that limiting the variation of the wave vector along the contour of the irreducible first Brillouin zone is practised extensively in almost all the literature relating to wave propagation in composite structures, although a rigorous mathematical proof of its validity is still awaited.

5.2.5 Determining the directional characteristics

Wave directional characteristics of periodic lattices which are inherently defined by the dispersion surfaces are represented in this work in terms of their phase velocity and group velocity as well as their dependence on frequency and

wave direction. Phase and group velocity provide a better application-tailored perspective and also better illustrate both the dispersive characteristics of lattices and their acoustic anisotropy. Phase velocity and group velocity are determined from the dispersion surfaces using,

$$\mathbf{c_p} = \frac{\omega}{\mathrm{k}}\widehat{\mathbf{u}} \quad \text{and} \quad \mathbf{c_g} = \left(\frac{\partial \omega}{\partial k_1}, \frac{\partial \omega}{\partial k_2}\right)^{\mathrm{T}} \tag{5.8}$$

where $\mathrm{k} = |\mathbf{k}|$. $\widehat{\mathbf{u}}$ is the unit vector pointing in the direction of the wave vector, $\left(\frac{\mathbf{k}}{\mathrm{k}}\right)$, and ω is the frequency. Thus, the aforementioned theoretical-computational based approach, based on integrating Bloch's theory with finite element computations, will be used to characterize the dispersion and directional characteristics in all lattices considered in this work. Results for each lattice will provide its wave band structure, dispersion surfaces, phase velocity and group velocity for multiple modes.

5.3   Results and Discussions

The Bloch wave-FE based methodology was used to obtain the dispersion surfaces for the first 10 eigenmodes for the relative densities 5%, 10%, 15%, 20%, 25%, 30%. The obtained dispersion surfaces are presented in Fig. 5.5. This figure shows that increased relative density increases the frequencies of the modes and shifts the dispersion surfaces upward, which is what would be expected in general as increased density increases wave propagation speed and increases the systems natural frequencies. However, based on Fig. 5.5, the effect of increased relative density on both natural frequencies and dispersion surfaces is not always linear. This is best illustrated by the nonlinear dependence of the spacing between the dispersion surfaces for the first 10 modes on relative density. Such behavior can be rationalized as eigenmodes have their own dominant deformation mechanisms, and therefore, different eigenmodes (wave propagation modes) depend differently on relative density. For each of the 6 relative densities analyzed, the first Brillouin zone was obtained and used to determine the band gap structure based on the first 10 modes. The
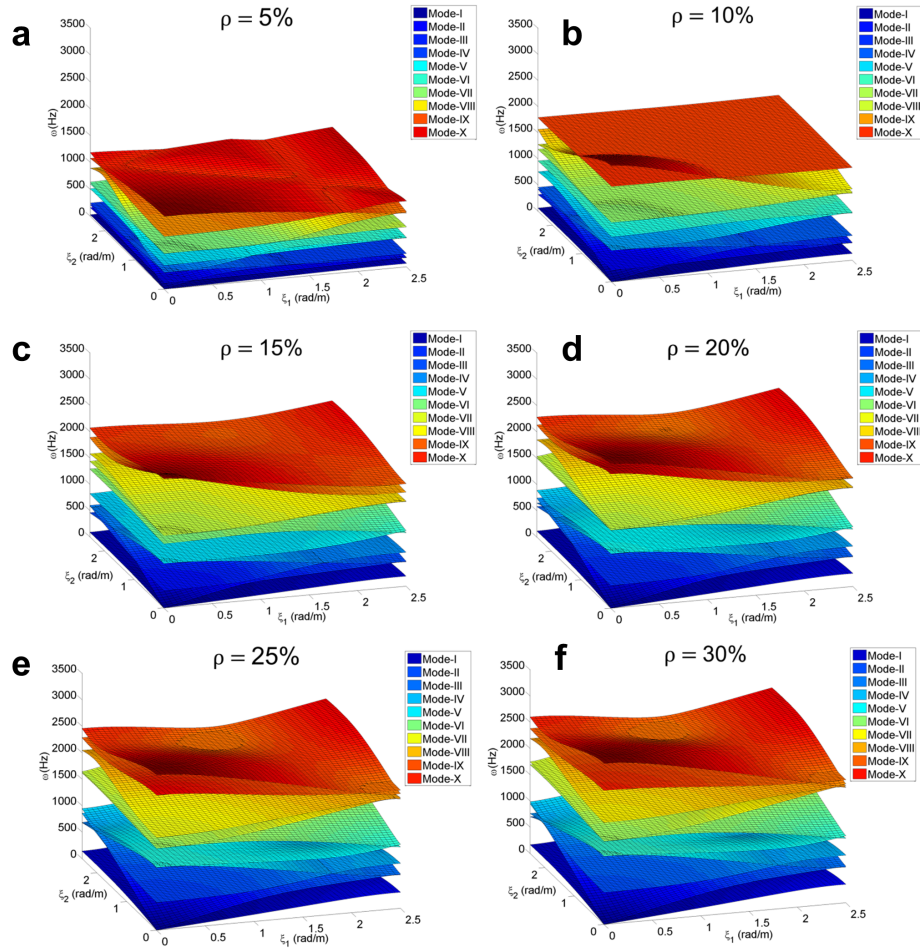
Figure 5.5: Iso-frequency surfaces for the hexagonal honeycomb, showing the first 10 eigenmodes for the relative densities of 5%, 10%, 15%, 20%, 525%, 30%.

band gap structures for the hexagonal specimen with relative densities of 5%, 10%, 15%, 20%, 25%, and 30% are presented in Fig. 5.5. This figure shows that gaps in the frequency spectrum were seen only at relative densities of 10%, 15%, 20% and 25%, whereas no band gaps were observed at 30% or 5% relative density.

87
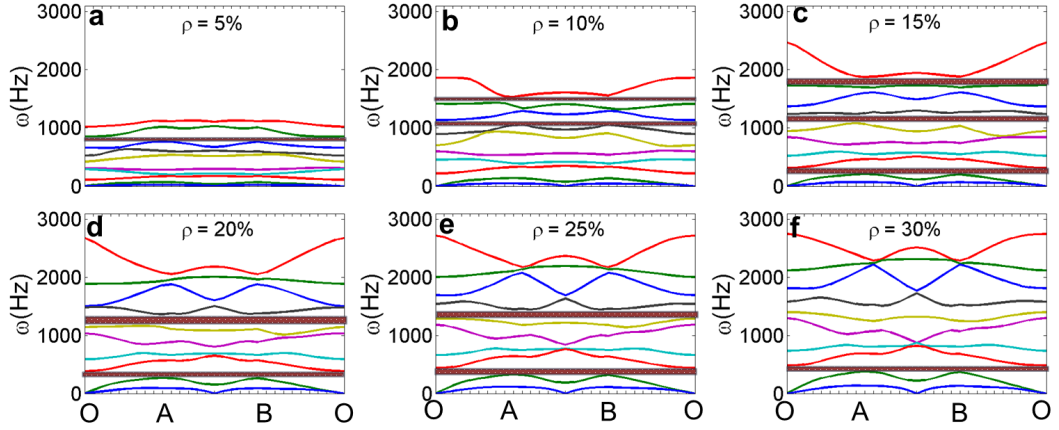
Figure 5.6: Frequency dispersion plots for the first 10 eigenmodes for the hexagonal lattice system for the relative densities of 5%, 10%, 15%, 20%, 525%, 30%. The band gaps have been highlighted (where present) shaded dark red.

5.3.1 Band-gap dispersion diagrams

In order to study the band-gap characteristics in cellular lattice architectures, the frequency band-gap dispersion diagrams were plotted for the hexagonal, tetragonal and triangular lattice configurations.

5.3.1.1 Hexagonal lattice architectures

The band gaps at 10%, 20% and 25% relative densities were around 1000 HZ, 2000 HZ, and 2100 HZ, respectively. Two bands (1300 HZ and 1700 HZ) were observed at 15% relative density. The effect of relative density on the band gap structure is not very intuitive. Clearly with increased density, the frequency and band structure is scaled upwardly but nonlinearly. Increased density affects higher modes more than lower modes; therefore, when increased relative density results in band gaps, these gaps will be exist at the higher frequencies (i.e. between higher order eigenmodes). A linear dependence on relative density would translate in widening bang gaps with increased relative density. However, based on Fig. 5.6 it can be observed that the band gaps were closed at 30% relative density instead of widening as the relative density was increased from 25% to 30%. This highlights the nonlinear dependence
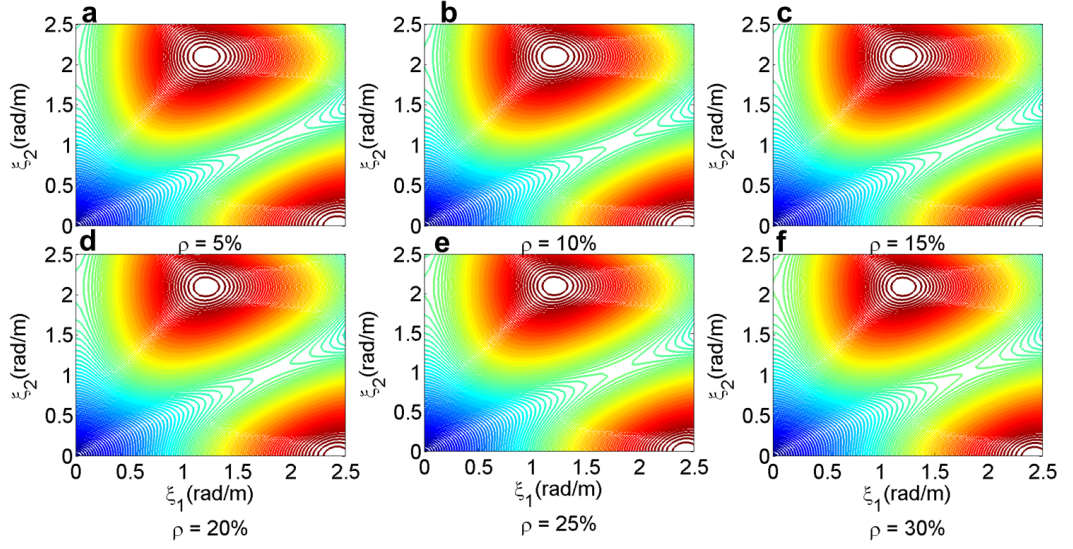
Figure 5.7: Mode I dispersion surfaces for the hexagonal honeycomb, showing the first 10 eigenmodes for the relative densities of 5%, 10%, 15%, 20%, 25%, 30%.

of the band gap structure on relative density. This behavior points to two important results. First, the band gap structure can vary significantly by changing relative density. Second, relative density can be used to obtain a tuned band gap structure. Moreover, by considering relative density as an additional tuning parameter along with topological features, the potential for designing application tailored band gap structures is greatly amplified.

To investigate the wave propagation characteristics and the effects of relative density on the wave phase speed and its direction, the dispersion surfaces for the first modes were extracted and plotted as isolines in Fig. 5.7. Each line in these plots implicitly represents the frequency dependent dispersion relation in terms of the direction dependent dispersion parameters at certain wave propagation mode. Near the origin of Fig. 5.7, the dispersion relations follow a circular profile which means that these dispersion relations are direction independent (i.e. wave propagating at the frequency of the particular isoline frequency would disperse in the same manner irrespective to the propagation direction). On the other hand, at higher frequencies, dispersion relations become more anisotropic (i.e. direction dependent). The aforementioned behavior is, to a great extent, visible at all relative densities. However,
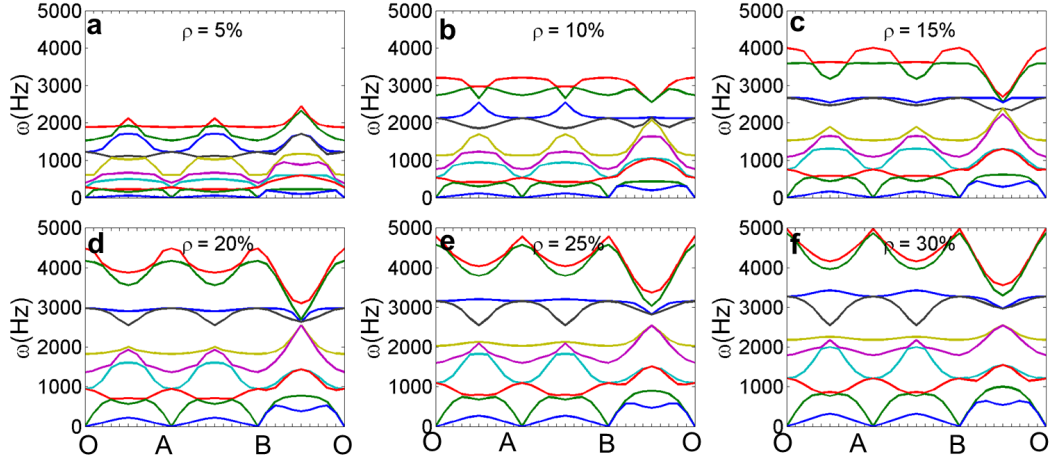
Figure 5.8: Frequency dispersion plots for the first 10 eigenmodes for the tetragonal lattice system for the relative densities of 5%, 10%, 15%, 20%, 525%, 30%. Note that no band gaps were observed for the tetragonal lattice configuration.

at higher densities the gradient between the isolines changes and tends to increase. Although in the neighbourhood of the first two modes, no band gaps were observed, interest here is focused on the first two modes as they represent the more basic and pure deformation modes (i.e. shear and longitudinal modes of in-plane wave propagation). At higher eigenmodes, wave propagates through complex mixed deformation modes.

5.3.1.2 Tetragonal lattice architectures

From the dispersion diagrams depicting the frequency band gaps, it was observed that no frequency band gaps existed for 5% - 30% relative densities (Fig. 5.8). A phenomenon known was *veering* was observed between between resonant frequency modes for all the relative densities plotted in the dispersion diagrams. coupled systems *Veering* is said to be observed when, for multiple eigenmodes, solutions to the elastodynamic equilibrium equations come infinitesimally close but do not become equal in value. This is a degenerate of the solutions to the elastodynamic equilibrium equations and is a common phenomenon found in the solution of eigenvalue problems containing weakly coupled systems.

Figure 5.9: Mode I dispersion surfaces for the tetragonal lattice, showing the first 10 eigenmodes for the relative densities of 5%, 10%, 15%, 20%, 25%, 30%.

This observation can be understood in light of the frequency contour plots for tetragonal structures, as shown in Fig. 5.9. By studying the configuration of the unit cell, we can say that the struts are axial and perpendicular to the direction of wave propagation.

This implies that the relative density has a linear relationship with strut thickness and therefore proportionately affects the area of material interacting with the incoming wave. In the iso-frequency plots we observe that there is no discontinuity in the spread within the frequency spectrum in the irreducible first Brillouin zone. This observation can be compared to the honeycomb case where a nonlinear dependence was reported for the relationship between relative density and the frequency band gaps.

5.3.1.3 Triangular lattice architectures

The band gaps at 15% and 20% relative densities were found to be between 2000 HZ and 3000 HZ, respectively and are shown in Fig. 5.10. Two bands (2100 HZ and 2800 HZ) were observed at 15% relative density. The effect of relative density on the band gap structure is nonlinear and non-intuitive.
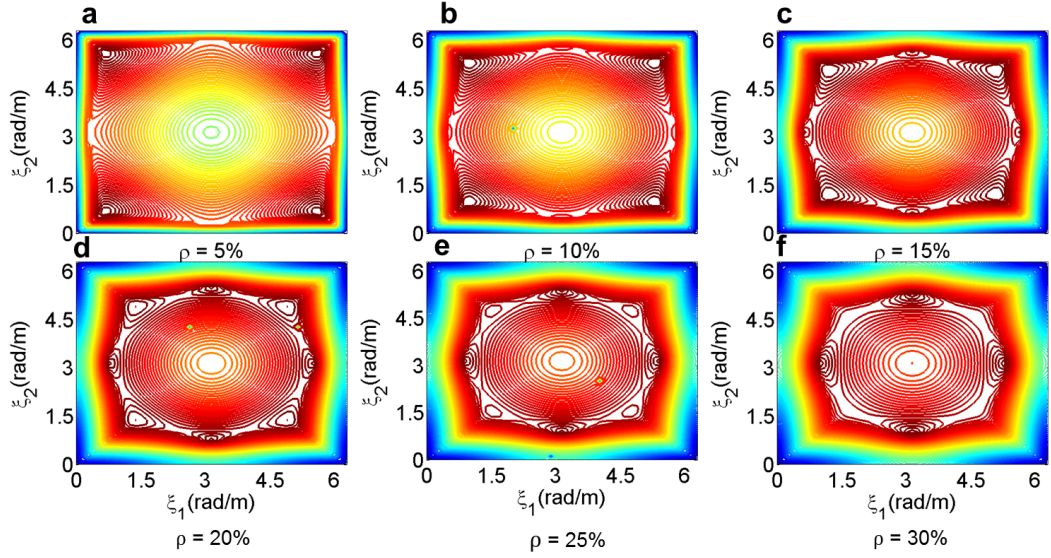
Figure 5.10: Frequency dispersion plots for the first 10 eigenmodes for the triangular lattice system for the relative densities of 5%, 10%, 15%, 20%, 525%, 30%. The band gaps have been highlighted (where present) shaded dark red.

Unlike the honeycomb lattice structure, the triangular lattice does not show a large variation in the frequency range of the the band gaps. This can be accounted by the structure of the triangular lattice which is more isotropic when compared to the honeycomb lattice. It must also be noted that, in the frequency dispersion plots (Fig. 5.10), the lower branch remains nearly invariant to the in relative density. This branch corresponds to the shear mode of a homogeneous medium with this slope defining the corresponding equivalent shear modulus and density of the homogenized medium. This can be further established by studying the frequency contours in the first Brillouin zone as given in Fig. 5.11.

5.3.2 Phase velocity diagrams

In order to study the band-gap characteristics in cellular lattice architectures, the frequency band-gap dispersion diagrams were plotted for the hexagonal, tetragonal and triangular lattice configurations.

Dispersion surfaces from Fig. 5.7 were used in conjunction with Eq. (6) to compute the direction and frequency dependent propagation phase velocity for the first two modes. Computed phase velocity plots are presented in Fig. 5.12, for the first and second eigenmodes, respectively. Phase velocity for the
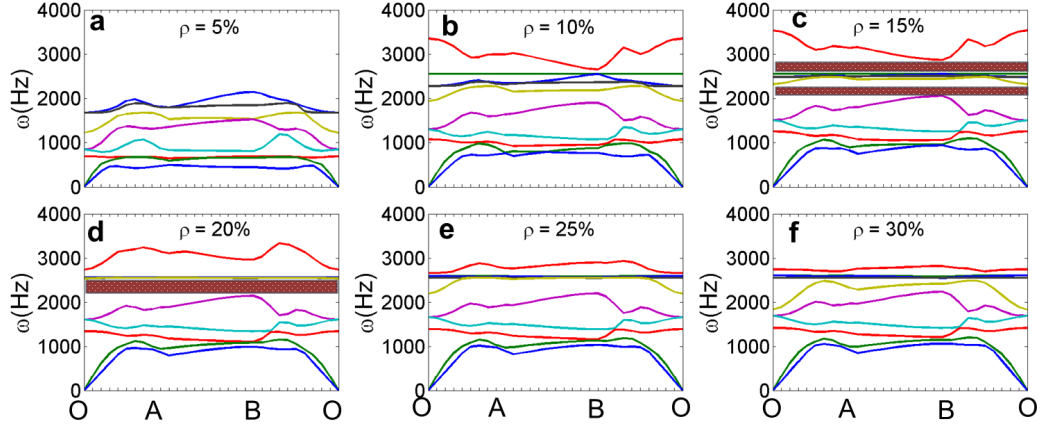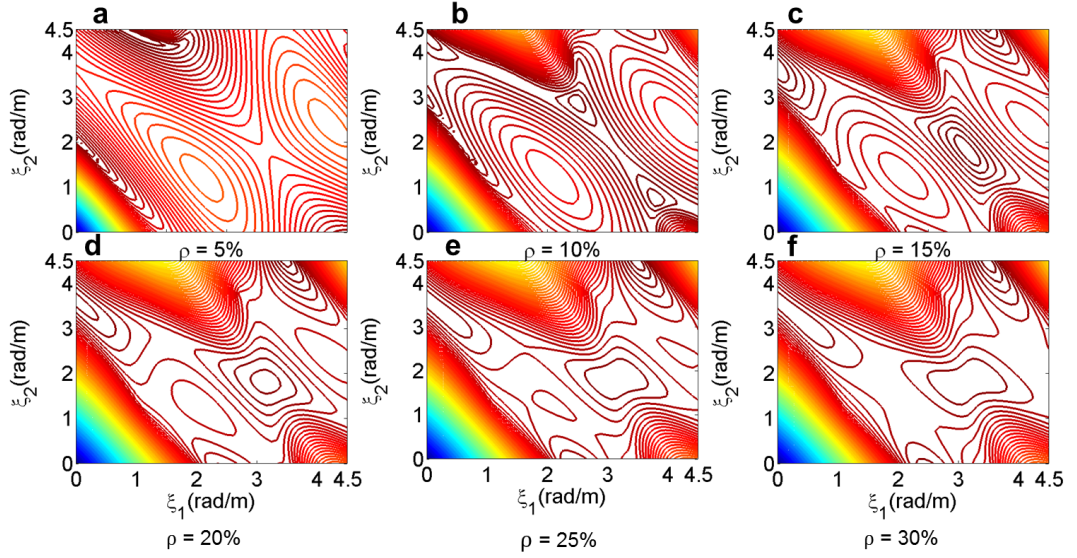
Figure 5.11: Mode I dispersion surfaces for the triangular lattice, showing the first 10 eigenmodes for the relative densities of 5%, 10%, 15%, 20%, 25%, 30%.

first mode (Fig. 5.12) shows that the velocity is highly dependent on direction due to the hexagonal cellular topology.

In addition, the figure shows that phase velocity increases with increasing relative density which is expected as the stiffness of the structure increases substantially with increased relative density. Here increased relative density translates to an increase in the ligament thickness which increases the stiffness of the structure. More importantly, as the structure is bending dominated (i.e. its ligaments are mostly loaded by bending moments), its stiffness dependence on relative density (i.e. thickness) is nonlinear. The observed change in phase velocity was about 5 folds when the relative density was increased from 5% to 30%. Phase velocity plots were also evaluated to analyse the role of the non-isotropic behaviour of the lattice and their dispersive characteristics. On comparing the phase velocities of the triangular structure with the corresponding phase velocity diagrams of the honeycomb structure (Fig. 5.13). The regular honeycomb as well as the triangular structures behave as regular isotropic solids at low frequencies. However on comparing Figs. 5.12 and 5.13, we observe that only the honeycomb is non-dispersive. At higher frequencies
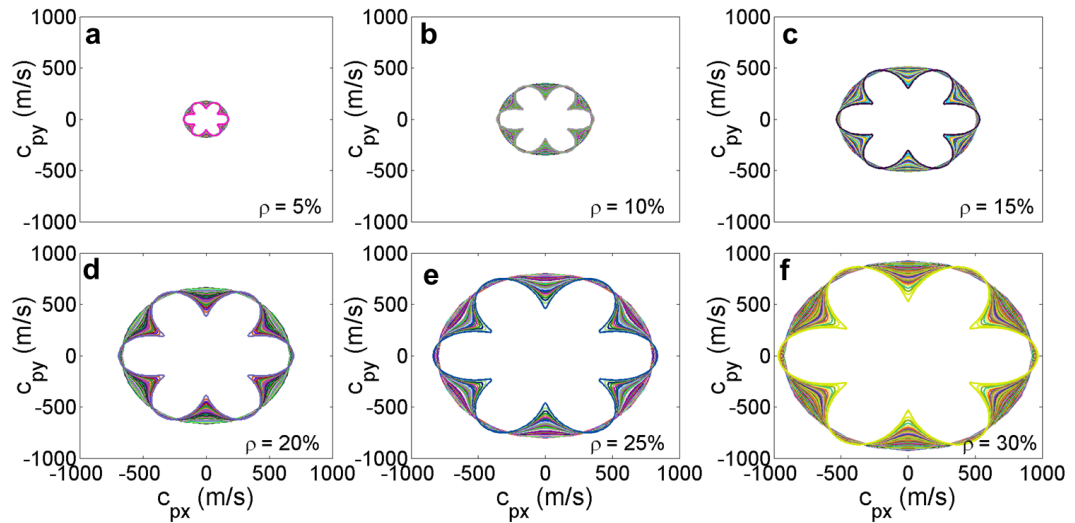
Figure 5.12: Phase velocity diagrams obtained from the first 20 mode I isofrequency lines for hexagonal honeycomb, showing the first 10 eigenmodes for the relative densities of 5%, 10%, 15%, 20%, 525%, 30%.

the phase velocity diagrams for the triangular lattice suggest that there is a shift from four-lobed to six-symmetry.

As intuitively can be predicted, the anisotropic phase velocity characteristics with its four planes of symmetry remain unchanged irrespective to relative density. This is true as the whole system was scaled uniformly. It should be noted that the phase velocity plots are for the first 10 dispersion isolines (i.e. lowest frequencies) seen in Fig. 5.7. At higher frequencies dispersion characteristics change and become more anisotropic.

As compared to the first mode, the phase velocity for the second mode exhibits very different characteristics. The velocity for the lowest 10 frequencies are isotropic and frequency independent. The phase velocity for the second mode exhibits interesting and not quite explicable or predicted behavior as the phase velocity seems to be insensitive to relative density. This might stem from a deformation pattern specific to the second eigenmode at the low frequencies that excite mostly axial deformation in the ligaments. In such cases, stiffness and mass of the hexagonal specimen scales linearly with relative density and therefore the speed of sound remains constant irrespective of relative density. However, this rationalization is qualitative and the observed unique behavior
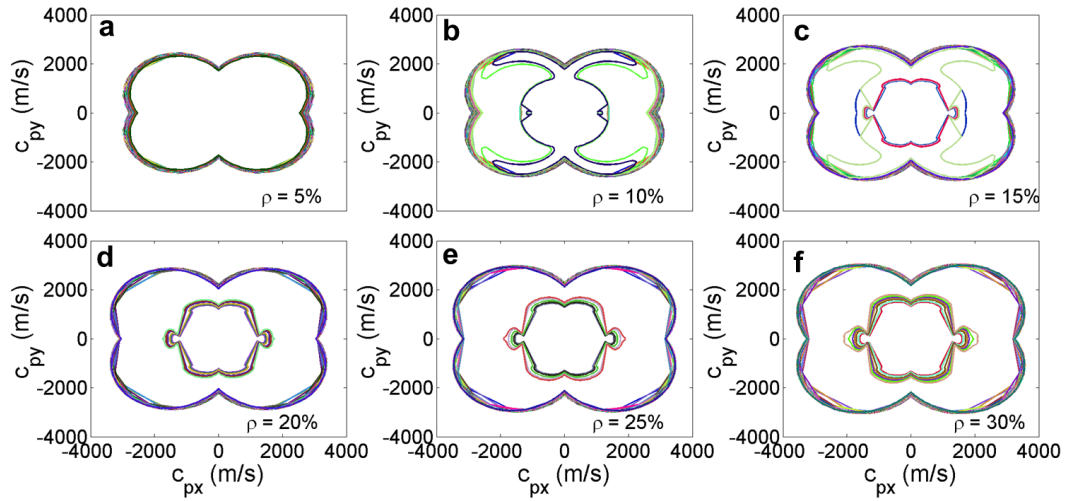
Figure 5.13: Phase velocity diagrams obtained from the first 20 mode I isofrequency lines for triangular lattice, showing the first 10 eigenmodes for the relative densities of 5%, 10%, 15%, 20%, 525%, 30%.

requires more analysis and scrutiny.

5.4   Conclusions

Bloch's theorem in conjunction with finite element analysis was used to investigate the relationships between relative density and constituent material anisotropy on the acoustic properties, wave dispersion, band gaps, and acoustic anisotropy of hexagonal lattice materials. Results illustrate that band structure and phononic properties are highly sensitive to relative density and can scale non-uniformly with relative density as eigenmodes are associated with relative density dependent deformation mechanisms. Moreover, results show that band gaps can potentially be activated and deactivated using macroscopic strain fields. The latter opens horizons for realizing cellular based phononic crystals with tunable properties. The potential for manipulating band gaps using simple uniform tensile strain fields was assessed by computing the band structure and band gaps before and after deformation. It is widely expected that very large strains can dramatically change the band gap structure of cellular architectures. However, here the focus on using relatively small strains
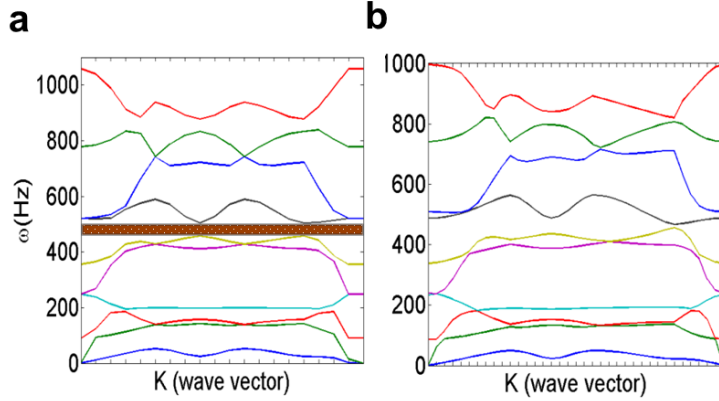
Figure 5.14: Phononic crystals, showing the band gaps structure exhibited by (a) regular honeycomb specimen (based on the 1st 10 modes), (b) Stretching the phononic honeycomb crystal eliminates the two band gaps exhibited by unstretched honeycombs. The band gaps have been highlighted (where present) shaded dark red.

(up to 5%) to manipulate and tune band gaps. Accordingly, anisotropic constituent material was used to build a hexagonal specimen whose geometric features are identical to the specimens used in this work so far. This path was pursued as the combination of anisotropic material and strain field can provide the required significant effect on band structure. For the anisotropic hexagonal specimen, the Bloch wave-FE approach was used as illustrated before, to obtain the band structure in the strain free state and in a state with 5% unidirectional tensile strain. The band gap structures from these two cases are presented in Fig. 5.14 (a) and (b). This figure shows that the strain free specimen has two band gaps that disappear when the 5% stretch is applied. The ramification of this observation is significant as it illustrates the potential for creating cellular architectures with tunable band gap properties that can be activated or deactivated using strain fields.

CHAPTER 6

Appendix

Appendix A. Electromechanical properties of common piezoelectric materials.

Table A.1: The room-temperature fundamental electromechanical properties of the piezoelectric materials, Barium Titanate, Barium Sodium Niobate, Lithium Niobate, and PVDF (single crystals) and PZT-7A (polycrystal), utilized in the analytical and finite-element models. The values for $(\mathbf{C}, \mathbf{e}, \kappa)$ are given in $(Pa, C/m^2, C/Vm)$ respectively [4, 5, 6, 7].

	Barium Titanate $BaTiO_3$	Barium Sodium Niobate $Ba_2NaNb_5O_{15}$	Lithium Niobate $LiNbO_3$	PZT-7A $Pb\left(Zr_xTi_{1-x}\right)O_3$	PVDF $-\left(C_2H_2F_2\right)_n-$
C_{11}	1.504E+11	2.389E+11	2.029E+11	1.480E+11	4.840E+09
C_{12}	6.563E+10	1.042E+11	5.292E+10	7.620E+10	2.720E+09
C_{22}	1.504E+11	2.474E+11	2.029E+11	1.480E+11	4.840E+09
C_{13}	6.594E+10	5.006E+10	7.491E+10	7.420E+10	2.220E+09
C_{23}	6.594E+10	5.214E+10	7.491E+10	7.420E+10	2.220E+09
C_{33}	1.455E+11	1.351E+11	2.431E+11	1.310E+11	4.630E+09
C_{14}	0.000	0.000	8.999E+09	0.000	0.000
C_{24}	0.000	0.000	-8.999E+09	0.000	0.000
C_{44}	4.386E+10	6.494E+10	5.590E+10	2.530E+10	5.260E+07
C_{55}	4.386E+10	6.579E+10	5.590E+10	2.530E+10	5.260E+07
C_{56}	0.000	0.000	8.985E+09	0.000	0.000
C_{66}	4.237E+10	7.576E+10	7.488E+10	3.590E+10	1.060E+09
e_{15}	11.404	2.763	3.424	9.310	-1.999E-03
e_{16}	0.000	0.000	-2.534	0.000	0.000
e_{21}	0.000	0.000	-2.538	0.000	0.000
e_{22}	0.000	0.000	-2.538	0.000	0.000
e_{24}	11.404	3.377	3.423	9.310	-1.999E-03
e_{31}	-4.322	-0.445	0.194	-2.324	4.344E-03
e_{32}	-4.322	-0.285	0.194	-2.324	4.344E-03
e_{33}	17.36	4.335	1.309	10.99	-1.099E-01
κ_{11}	1.284E-08	2.081E-09	7.437E-10	3.984E-09	6.641E-11
κ_{22}	1.284E-08	2.187E-09	7.437E-10	3.984E-09	6.641E-11
κ_{33}	1.505E-08	4.516E-10	2.656E-10	2.081E-09	7.083E-11

Appendix B. The concentration tensors for strain and electric field A, a, B, b

The expressions for the average strain and electric field in the particle phase can be used to derive expressions for the effective elastic, piezoelectric, and dielectric tensors. Solving (4.37) and (4.38) for the two unknowns $\bar{\varepsilon}_{mn}^{(2)}$ and $\bar{\phi}_{mn}^{(2)}$ we obtain equations with the following form:-

$$\bar{\varepsilon}_{kl}^{(2)} = A_{mnkl}^{(2)}\varepsilon_{mn}^0 + a_{klq}^{(2)}\phi_{,q}^0, \qquad \bar{\phi}_{,o}^{(2)} = B_{omn}^{(2)}\varepsilon_{mn}^0 + b_{op}^{(2)}\phi_{,p}^0 \qquad (A.1)$$

where **A** and **a** are the strain concentration tensors for the particle phase and **B** and **b** are the corresponding electric field concentration tensors. The expressions for the effective moduli tensors in terms of the concentration tensors are given by:

$$\widetilde{L}_{ijkl} = L_{ijkl}^{(1)} + c^{(2)}\Delta L_{ijmn}^{(2)}A_{mnkl}^{(2)} + c^{(2)}\Delta e_{pij}^{(2)}B_{pkl}^{(2)} \qquad (A.2)$$

$$\widetilde{e}_{imn} = e_{imn}^{(1)} + c^{(2)}\Delta e_{ikl}^{(2)}A_{klmn}^{(2)} - c^{(2)}\Delta\kappa_{ik}^{(2)}B_{kmn}^{(2)} \qquad (A.3)$$

$$\widetilde{\kappa}_{in} = \kappa_{in}^{(1)} + c^{(2)}\Delta\kappa_{ik}^{(2)}b_{kn}^{(2)} - c^{(2)}\Delta e_{ikl}^{(2)}a_{kln}^{(2)} \qquad (A.4)$$

The explicit expressions for the concentration tensors in terms of the microstructural tensors, are given below. At this point it would worthwhile to mention that solving for the fourth-order strain concentration tensor $\mathbf{A^{(2)}}$ would require the implementation of a numerical code capable of solving 36 equations in 36 unknowns in order to determine all its independent components. Note that the concentration tensor $\mathbf{A^{(2)}}$ only has minor symmetry.

$$\mathbf{A^{(2)}} = \left[\mathbf{I^s} - \left(\mathbf{P^{(22)}\Delta L^{(2)}} + \mathbf{Q^{(22)}\Delta e^{(2)}}\right) - \left(\mathbf{P^{(22)}\Delta e^{(2)}} - \mathbf{Q^{(22)}\Delta\kappa^{(2)}}\right)\right.$$
$$\left.\left\{\mathbf{I} - \left(\mathbf{Q^{(22)}\Delta e^{(2)}} - \mathbf{R^{(22)}\Delta\kappa^{(2)}}\right)\right\}^{-1}\left(\mathbf{Q^{(22)}\Delta L^{(2)}} + \mathbf{R^{(22)}\Delta e^{(2)}}\right)\right]^{-1}$$
$$(A.5)$$

$$\mathbf{a^{(2)}} = -\mathbf{A^{(2)}}\left(\mathbf{P^{(22)}\Delta e^{(22)}} - \mathbf{Q^{(22)}\Delta\kappa^{(2)}}\right)\{\mathbf{I}$$

$$- \left(\mathbf{Q^{(22)}} \mathbf{\Delta e^{(2)}} - \mathbf{R^{(22)}} \mathbf{\Delta \kappa^{(2)}} \right) \right\}^{-1} \qquad \text{(A.6)}$$

$$\mathbf{B^{(2)}} = \left\{ \mathbf{I} - \left(\mathbf{Q^{(22)}} \mathbf{\Delta e^{(2)}} - \mathbf{R^{(22)}} \mathbf{\Delta \kappa^{(2)}} \right) \right\}^{-1}$$
$$\left(\mathbf{Q^{(22)}} \mathbf{\Delta L^{(2)}} + \mathbf{R^{(22)}} \mathbf{\Delta e^{(2)}} \right) \qquad \text{(A.7)}$$

$$\mathbf{b^{(2)}} = \left\{ \mathbf{I} - \left(\mathbf{Q^{(22)}} \mathbf{\Delta e^{(2)}} - \mathbf{R^{(22)}} \mathbf{\Delta \kappa^{(2)}} \right) \right\}^{-1}$$
$$+ \ \mathbf{B^{(2)}} \left(\mathbf{P^{(22)}} \mathbf{\Delta e^{(2)}} - \mathbf{Q^{(22)}} \mathbf{\Delta \kappa^{(2)}} \right)$$
$$\left\{ \mathbf{I} - \left(\mathbf{Q^{(22)}} \mathbf{\Delta e^{(2)}} - \mathbf{R^{(22)}} \mathbf{\Delta \kappa^{(2)}} \right) \right\}^{-1} \qquad \text{(A.8)}$$

where the tensors $\mathbf{I}$ and $\mathbf{I^s}$ are the 2nd and 4th order identity tensors, respectively. The symmetric 4th-order identity tensor is defined in terms of the Kronecker delta as follows:

$$I^s_{ijkl} = \frac{1}{2} \left(\delta_{ik} \delta_{jl} + \delta_{il} \delta_{jk} \right) \qquad \text{(A.9)}$$

$$\delta_{ij} = \begin{cases} 1 & \text{if } i = j; \\ 0 & \text{if } i \neq j. \end{cases} \qquad \text{(A.10)}$$

Appendix C. The microstructural tensors P, Q, R

In this appendix, explicit expressions for the components of the microstructural tensors $\mathbf{P}, \mathbf{Q}, \mathbf{R}$ which characterize the three types of geometric configurations i.e., (a) periodic square distribution of long pores/fibers, (b) periodic cubic distribution of spheres, and (c) hexagonal distribution of long pores/fibers, have been given.

Periodic square distribution

For the periodic square distribution, the base vectors $\mathbf{Y}_i$ ($i = 1, 2, 3$) are given by $\mathbf{Y}_1 = d\,\mathbf{e}_1$, $\mathbf{Y}_2 = d\,\mathbf{e}_2$, $\mathbf{Y}_3 = \infty\,\mathbf{e}_3$, where d is the length of edge of the

square.

$$P_{ijmn} = \sum_{\substack{n_1=-\infty \\ -\{n_1=n_2=0\}}}^{+\infty} \sum_{n_2=-\infty}^{+\infty} c^{(2)} H_{ijmn}^s \frac{4J_1^2(bk)}{b^2 k^2}, \tag{A.11}$$

$$Q_{ijk} = \sum_{\substack{n_1=-\infty \\ -\{n_1=n_2=0\}}}^{+\infty} \sum_{n_2=-\infty}^{+\infty} c^{(2)} \beta_{ijk}^s \frac{4J_1^2(bk)}{b^2 k^2}, \tag{A.12}$$

$$R_{ij} = \sum_{\substack{n_1=-\infty \\ -\{n_1=n_2=0\}}}^{+\infty} \sum_{n_2=-\infty}^{+\infty} c^{(2)} \gamma_{ij}^s \frac{4J_1^2(bk)}{b^2 k^2}, \tag{A.13}$$

where $\xi_1 = 2\pi n_1/d$, $\xi_2 = 2\pi n_2/d$, $\xi_3 = 0$, $b = \sqrt{\frac{c^{(2)}}{\pi}}$, and $k = 2\pi\sqrt{n_1^2 + n_2^2}$ and it is recalled that $J_1(\cdot)$ is the Bessel function of first kind and $c^{(2)}$ is the volume fraction of the second phase. The superscript "s" on the tensors on the right-hand side indicates symmetrization.

Periodic cubic distribution

For the periodic cubic distribution of spherical voids, the base vectors $\mathbf{Y}_i$ ($i = 1, 2, 3$) are given by $\mathbf{Y}_1 = d\,\mathbf{e}_1$, $\mathbf{Y}_2 = d\,\mathbf{e}_2$, $\mathbf{Y}_3 = d\,\mathbf{e}_3$. The expressions for $\mathbf{P}$, $\mathbf{Q}$, $\mathbf{R}$ specializes to:

$$P_{ijmn} = \sum_{\substack{n_1=-\infty \\ -\{n_1=n_2=n_3=0\}}}^{+\infty} \sum_{n_2=-\infty}^{+\infty} \sum_{n_3=-\infty}^{+\infty} c^{(2)} H_{ijmn}^s \left[\frac{3\left(-bk\cos(bk) + \sin(bk)\right)}{b^3 k^3} \right]^2, \tag{A.14}$$

$$Q_{ijk} = \sum_{\substack{n_1=-\infty \\ -\{n_1=n_2=n_3=0\}}}^{+\infty} \sum_{n_2=-\infty}^{+\infty} \sum_{n_3=-\infty}^{+\infty} c^{(2)} \beta_{ijk}^s \left[\frac{3\left(-bk\cos(bk) + \sin(bk)\right)}{b^3 k^3} \right]^2, \tag{A.15}$$

$$R_{ij} = \sum_{\substack{n_1=-\infty \\ -\{n_1=n_2=n_3=0\}}}^{+\infty} \sum_{n_2=-\infty}^{+\infty} \sum_{n_3=-\infty}^{+\infty} c^{(2)} \gamma_{ij}^s \left[\frac{3\left(-bk\cos(bk) + \sin(bk)\right)}{b^3 k^3} \right]^2, \tag{A.16}$$

100

where $\xi_1 = 2\pi n_1/d$, $\xi_2 = 2\pi n_2/d$, $\xi_3 = 2\pi n_3/d$, $b = \left[\frac{3c^{(2)}}{4\pi}\right]^{\frac{1}{3}}$, and $k = 2\pi\sqrt{n_1^2 + n_2^2 + n_3^2}$.

Periodic hexagonal distribution

For the periodic hexagonal distribution, the base vectors $\mathbf{Y}_i$ $(i = 1, 2, 3)$ are given by $\mathbf{Y}_1 = \sqrt{3}d\,\mathbf{e}_1$, $\mathbf{Y}_2 = \sqrt{3}d/2\,\mathbf{e}_1 + 3d/2\,\mathbf{e}_2$, $\mathbf{Y}_3 = \infty\,\mathbf{e}_3$, where d is the length of the sides of the regular hexagon, so that expressions for $\mathbf{P}$, $\mathbf{Q}$, $\mathbf{R}$ specializes to:

$$\mathrm{P}_{ijmn} = \sum_{\substack{n_1=-\infty \\ -\{n_1=n_2=0\}}}^{+\infty} \sum_{n_2=-\infty}^{+\infty} c^{(2)}\mathrm{H}_{ijmn}^s \frac{4J_1^2(bk)}{b^2k^2}, \tag{A.17}$$

$$\mathrm{Q}_{ijk} = \sum_{\substack{n_1=-\infty \\ -\{n_1=n_2=0\}}}^{+\infty} \sum_{n_2=-\infty}^{+\infty} c^{(2)}\beta_{ijk}^s \frac{4J_1^2(bk)}{b^2k^2}, \tag{A.18}$$

$$\mathrm{R}_{ij} = \sum_{\substack{n_1=-\infty \\ -\{n_1=n_2=0\}}}^{+\infty} \sum_{n_2=-\infty}^{+\infty} c^{(2)}\gamma_{ij}^s \frac{4J_1^2(bk)}{b^2k^2}, \tag{A.19}$$

where $\xi_1 = 2\pi n_1/\left(\sqrt{3}d\right)$, $\xi_2 = 2\pi(2n_2 - n_1)/3d$, $\xi_3 = 0$. Note that now, $b = \sqrt{\frac{3\sqrt{3}c^{(2)}}{2\pi}}$, and $k = \frac{4\pi}{3}\sqrt{n_1^2 - n_1n_2 + n_2^2}$

Appendix D. Explicit closed-form expressions for K, q and p for a square, hexagonal and cubic distribution of fibers/pores in a general anisotropic piezoelectric matrix.

The closed-form expressions for all the components of $\mathbf{K}$, $\mathbf{q}$ and the scalar quantity p, derived in Eqs. (4.20) and (4.21) for square, hexagonal and cubic distribution of fibers/pores (of arbitrary geometry) in a general anisotropic piezoelectric matrix are provided in the three tables D.1, D.2 and D.3. It can be observed that the components of $\mathbf{K}$, $\mathbf{q}$ and p are dependent on the periodic

101

Table D.1: A table showing all the components of the quantities used in Eq.(4.20) for a square distribution of fibers/pores in a general anisotropic piezoelectric matrix.

Component	Square
K_{11}	$4\pi^2\left(C_{11}n_1^2 + 2C_{16}n_1n_2 + C_{66}n_2^2\right)/d^2$
$K_{12} = K_{21}$	$4\pi^2\left(C_{12}n_1n_2 + C_{16}n_1^2 + C_{26}n_2^2 + C_{66}n_1n_2\right)/d^2$
$K_{13} = K_{31}$	$4\pi^2\left(C_{14}n_1n_2 + C_{15}n_1^2 + C_{46}n_2^2 + C_{56}n_1n_2\right)/d^2$
K_{22}	$4\pi^2\left(C_{22}n_2^2 + 2C_{26}n_1n_2 + C_{66}n_1^2\right)/d^2$
$K_{23} = K_{32}$	$4\pi^2\left(C_{24}n_2^2 + C_{25}n_1n_2 + C_{46}n_1n_2 + C_{56}n_1^2\right)/d^2$
K_{33}	$4\pi^2\left(C_{44}n_2^2 + 2C_{45}n_1n_2 + C_{55}n_1^2\right)/d^2$
q_1	$4\pi^2\left(e_{11}n_1^2 + e_{16}n_1n_2 + e_{21}n_1n_2 + e_{26}n_2^2\right)/d^2$
q_2	$4\pi^2\left(e_{12}n_1n_2 + e_{16}n_1^2 + e_{22}n_2^2 + e_{26}n_1n_2\right)/d^2$
q_3	$4\pi^2\left(e_{14}n_1n_2 + e_{15}n_1^2 + e_{24}n_2^2 + e_{25}n_1n_2\right)/d^2$
p	$4\pi^2\left(\kappa_{11}n_1^2 + 2\kappa_{12}n_1n_2 + \kappa_{22}n_2^2\right)/d^2$

distribution of the second phase as well the elastic, piezoelectric and dielectric constants. The periodic Green's operators given in Eqs. (4.26),(4.27) and (4.28), can be derived by using the expressions provided in the tables. The notation used in the tables is the Voigt contracted notation as explained in Section 4.4. According to this notation the indices, $11 = 1$, $22 = 2$, $33 = 3$, $23 = 4$, $13 = 5$, $12 = 6$. Therefore $L_{1111} = C_{11}$, $L_{3333} = C_{33}$, $L_{2323} = C_{44}$, etc. The second subscript of the piezoelectric constants follow the aforementioned Voigt notation, whereby $e_{111} = e_{11}$, $e_{122} = e_{12}$, $e_{133} = e_{13}$, $e_{123} = e_{14}$, etc. The quantity denoted by "d" is the length of the sides of the square, cube or hexagonal unit-cell.

Table D.2: A table showing all the components of the quantities used in Eq.(4.20) for a hexagonal distribution of fibers/pores in a general anisotropic piezoelectric matrix.

Component	Hexagonal
K_{11}	$(4\pi^2/9)\left(3C_{11}n_1^2 - 2C_{16}\sqrt{3}n_1^2 + 4C_{16}\sqrt{3}n_1n_2 + C_{66}n_1^2 - 4C_{66}n_1n_2 + 4C_{66}n_2^2\right)/d^2$
$K_{12} = K_{21}$	$-(4\pi^2/9)\left(-3C_{16}n_1^2 + C_{12}\sqrt{3}n_1^2 - 2C_{12}\sqrt{3}n_1n_2 + C_{66}\sqrt{3}n_1^2 - 2C_{66}\sqrt{3}n_1n_2 - C_{26}n_1^2 + 4C_{26}n_1n_2 - 4C_{26}n_2^2\right)/d^2$
$K_{13} = K_{31}$	$-(4\pi^2/9)\left(-3C_{15}n_1^2 + C_{14}\sqrt{3}n_1^2 - 2C_{14}\sqrt{3}n_1n_2 + C_{56}\sqrt{3}n_1^2 - 2C_{56}\sqrt{3}n_1n_2 - C_{46}n_1^2 + 4C_{46}n_1n_2 - 4C_{46}n_2^2\right)/d^2$
K_{22}	$(4\pi^2/9)\left(3C_{66}n_1^2 - 2C_{26}\sqrt{3}n_1^2 + 4C_{26}\sqrt{3}n_1n_2 + C_{22}n_1^2 - 4C_{22}n_1n_2 + 4C_{22}n_2^2\right)/d^2$
$K_{23} = K_{32}$	$(4\pi^2/9)\left(3C_{56}n_1^2 - C_{25}\sqrt{3}n_1^2 + 2C_{25}\sqrt{3}n_1n_2 - C_{46}\sqrt{3}n_1^2 + 2C_{46}\sqrt{3}n_1n_2 + C_{24}n_1^2 - 4C_{24}n_1n_2 + 4C_{24}n_2^2\right)/d^2$
K_{33}	$(4\pi^2/9)\left(3C_{55}n_1^2 - 2C_{45}\sqrt{3}n_1^2 + 4C_{45}\sqrt{3}n_1n_2 + C_{44}n_1^2 - 4C_{44}n_1n_2 + 4C_{44}n_2^2\right)/d^2$
q_1	$-(4\pi^2/9)\left(\sqrt{3}e_{16}n_1^2 - 2\sqrt{3}e_{16}n_1n_2 + \sqrt{3}e_{21}n_1^2 - 2\sqrt{3}e_{21}n_1n_2 - 3e_{11}n_1^2 - e_{26}n_1^2 + 4e_{26}n_1n_2 - 4e_{26}n_2^2\right)/d^2$
q_2	$-(4\pi^2/9)\left(\sqrt{3}e_{12}n_1^2 - 2\sqrt{3}e_{12}n_1n_2 + \sqrt{3}e_{26}n_1^2 - 2\sqrt{3}e_{26}n_1n_2 - 3e_{16}n_1^2 - e_{22}n_1^2 + 4e_{22}n_1n_2 - 4e_{22}n_2^2\right)/d^2$
q_3	$-(4\pi^2/9)\left(\sqrt{3}e_{14}n_1^2 - 2\sqrt{3}e_{14}n_1n_2 + \sqrt{3}e_{25}n_1^2 - 2\sqrt{3}e_{25}n_1n_2 - 3e_{15}n_1^2 - e_{24}n_1^2 + 4e_{24}n_1n_2 - 4e_{24}n_2^2\right)/d^2$
p	$-(4\pi^2/9)\left(2\sqrt{3}\kappa_{12}n_1^2 - 4\sqrt{3}\kappa_{12}n_1n_2 - 3\kappa_{11}n_1^2 - \kappa_{22}n_1^2 + 4\kappa_{22}n_1n_2 - 4\kappa_{22}n_2^2\right)/d^2$

Table D.3: A table showing all the components of the quantities used in Eq.(4.20) for a cubic distribution of fibers/pores in a general anisotropic piezoelectric matrix.

Component	Cubic
K_{11}	$4\pi^2\left(C_{11}n_1^2 + 2C_{15}n_1n_3 + 2C_{16}n_1n_2 + C_{55}n_3^2 + 2C_{56}n_2n_3 + C_{66}n_2^2\right)/d^2$
$K_{12} = K_{21}$	$4\pi^2\left(C_{12}n_1n_2 + C_{14}n_1n_3 + C_{16}n_1^2 + C_{25}n_2n_3 + C_{26}n_2^2 + C_{45}n_3^2 + C_{46}n_2n_3 + C_{56}n_1n_3 + C_{66}n_1n_2\right)/d^2$
$K_{13} = K_{31}$	$4\pi^2\left(C_{13}n_1n_3 + C_{14}n_1n_2 + C_{15}n_1^2 + C_{35}n_3^2 + C_{36}n_2n_3 + C_{45}n_2n_3 + C_{46}n_2^2 + C_{55}n_1n_3 + C_{56}n_1n_2\right)/d^2$
K_{22}	$4\pi^2\left(C_{22}n_2^2 + 2C_{24}n_2n_3 + 2C_{26}n_1n_2 + C_{44}n_3^2 + 2C_{46}n_1n_3 + C_{66}n_1^2\right)/d^2$
$K_{23} = K_{32}$	$4\pi^2\left(C_{23}n_2n_3 + C_{24}n_2^2 + C_{25}n_1n_2 + C_{34}n_3^2 + C_{36}n_1n_3 + C_{44}n_2n_3 + C_{45}n_1n_3 + C_{46}n_1n_2 + C_{56}n_1^2\right)/d^2$
K_{33}	$4\pi^2\left(C_{33}n_3^2 + 2C_{34}n_2n_3 + 2C_{35}n_1n_3 + C_{44}n_2^2 + 2C_{45}n_1n_2 + C_{55}n_1^2\right)/d^2$
q_1	$4\pi^2\left(e_{11}n_1^2 + e_{15}n_1n_3 + e_{16}n_1n_2 + e_{21}n_1n_2 + e_{25}n_2n_3 + e_{26}n_2^2 + e_{31}n_1n_3 + e_{35}n_3^2 + e_{36}n_2n_3\right)/d^2$
q_2	$4\pi^2\left(e_{12}n_1n_2 + e_{14}n_1n_3 + e_{16}n_1^2 + e_{22}n_2^2 + e_{24}n_2n_3 + e_{26}n_1n_2 + e_{32}n_2n_3 + e_{34}n_3^2 + e_{36}n_1n_3\right)/d^2$
q_3	$4\pi^2\left(e_{13}n_1n_3 + e_{14}n_1n_2 + e_{15}n_1^2 + e_{23}n_2n_3 + e_{24}n_2^2 + e_{25}n_1n_2 + e_{33}n_3^2 + e_{34}n_2n_3 + e_{35}n_1n_3\right)/d^2$
p	$4\pi^2\left(\kappa_{11}n_1^2 + 2\kappa_{12}n_1n_2 + 2\kappa_{13}n_1n_3 + \kappa_{22}n_2^2 + 2\kappa_{23}n_2n_3 + \kappa_{33}n_3^2\right)/d^2$

Bibliography

[1] I. G. Masters, K. E. Evans, Models for the elastic deformation of honeycombs, Composite Structures 35 (4) (1996) 403–422.

[2] J. Bravo-Castillero, R. Guinovart-Diaz, F. J. Sabina, R. Rodrguez-Ramos, Closed-form expressions for the effective coefficients of a fiber-reinforced composite with transversely isotropic constituents - II. piezoelectric and square symmetry, Mechanics of Materials 33 (4) (2001) 237 – 248. doi:10.1016/S0167-6636(00)00060-0.

[3] J. Gibson, L., F. Ashby, M., Cellular Solids: Structure and Properties, 1997.

[4] H. Jaffe, D. Berlincourt, Piezoelectric transducer materials, Proceedings of the IEEE 53 (10) (1965) 1372–1386.

[5] A. Warner, G. Coquin, J. Fink, Elastic and piezoelectric constants of $Ba_2NaNb_5O_{15}$, Journal of Applied Physics 40 (11) (1969) 4353–4356.

[6] A. Warner, M. Onoe, G. Coquin, Determination of elastic and piezoelectric constants for crystals in class (3m), The journal of the acoustical society of America 42 (1967) 1223.

[7] H. Wang, Q. Zhang, L. Cross, A. Sykes, Piezoelectric, dielectric, and elastic properties of poly (vinylidene fluoride/trifluoroethylene), Journal of applied physics 74 (5) (1993) 3394–3398.

[8] M. F. Ashby, T. Evans, N. Fleck, J. Hutchinson, H. Wadley, Metal Foams: A Design Guide, BUTTERWORTH-HEINEMANN, 2000.

[9] G. Lorna J, Biomechanics of cellular solids, Journal of Biomechanics 38 (3) (2005) 377–399.

[10] N. A. Fleck, V. S. Deshpande, M. F. Ashby, Micro-architectured materials: past, present and future, Proceedings of the Royal Society a-Mathematical Physical and Engineering Sciences 466 (2121) (2010) 2495–2516.

[11] S. M. Pingle, N. A. Fleck, V. S. Deshpande, H. N. G. Wadley, Collapse mechanism maps for a hollow pyramidal lattice, Proceedings of the Royal Society A: Mathematical, Physical and Engineering Science 467 (2128) (2011) 985–1011.

[12] M. Alkhader, M. Vural, Mechanical response of cellular solids: Role of cellular topology and microstructural irregularity, International Journal of Engineering Science 46 (10) (2008) 1035–1051.

[13] M. Alkhader, M. Vural, The partition of elastic strain energy in solid foams and lattice structures, Acta Materialia 57 (8) (2009) 2429–2439.

[14] R. Broos, R. Herrington, F. Casati, Endurance of polyurethane automotive seating foams under varying temperature and humidity conditions, Journal of Cellular Plastics 36 (3) (2000) 207–245.

[15] T. M. Marsalko, Product development of polyurethane foams for automotive applications, Abstracts of Papers of the American Chemical Society 215 (1998) U344–U344.

[16] M. R. Kinkelaar, K. D. Cavender, G. Crocco, Vibrational characterization of various polyurethane foams employed in automotive seating applications, Journal of Cellular Plastics 34 (2) (1998) 155–173.

[17] H. F. Seibert, Applications for pmi foams in aerospace sandwich structures, Reinforced Plastics 50 (1) (2006) 44–48.

[18] S. Gupta, A. Shukla, Blast performance of marine foam core sandwich composites at extreme temperatures, Experimental Mechanics 52 (9) (2012) 1521–1534.

[19] A. T. Grenier, N. A. Dembsey, J. R. Barnett, Fire characteristics of cored composite materials for marine use, Fire Safety Journal 30 (2) (1998) 137–159.

[20] J. M. Ortega, J. Hartman, J. N. Rodriguez, D. J. Maitland, Virtual treatment of basilar aneurysms using shape memory polymer foam, Annals of Biomedical Engineering (2013) 1–19.

[21] W. Hwang, B. L. Volk, F. Akberali, P. Singhal, J. C. Criscione, D. J. Maitland, Estimation of aneurysm wall stresses created by treatment with a shape memory polymer foam device, Biomechanics And Modeling In Mechanobiology 11 (5) (2012) 715–729.

[22] K. S. Challagulla, T. A. Venkatesh, Computational modeling of piezoelectric foams, JOM 65 (2) (2013) 256–266.

[23] K. S. Challagulla, T. A. Venkatesh, Electromechanical response of piezoelectric foams, Acta Materialia 60 (5) (2012) 2111–2127.

[24] S. Iyer, T. A. Venkatesh, Electromechanical response of (3-0) porous piezoelectric materials: Effects of porosity shape, Journal of Applied Physics 110 (3) (2011) 034109–8.

[25] S. Iyer, T. A. Venkatesh, Electromechanical response of porous piezoelectric materials: Effects of porosity connectivity, Applied Physics Letters 97 (7) (2010) 072904–3.

[26] R. Kar-Gupta, T. A. Venkatesh, Electromechanical response of porous piezoelectric materials, Acta Materialia 54 (15) (2006) 4063–4078.

[27] C. Witherspoon, P. Zheng, M. Chmielus, S. C. Vogel, D. C. Dunand, P. Mllner, Texture and training of magnetic shape memory foam, Acta Materialia 61 (6) (2013) 2113–2120.

[28] M. J. Haun, R. E. Newnham, An experimental and theoretical study of 13 and 1-3-0 piezoelectric pzt-polymer composites for hydrophone applications, Ferroelectrics 68 (1) (1986) 123–139.

[29] R. Newnham, D. Skinner, L. Cross, Connectivity and piezoelectric-pyroelectric composites, Materials Research Bulletin 13 (1978) 525–536.

[30] T. Arai, K. Ayusawa, H. Sato, T. Miyata, K. Kawamura, K. Kobayashi, Properties of hydrophone with porous piezoelectric ceramics, Japanese Journal of Applied Physics Part 1-Regular Papers Short Notes and Review Papers 30 (9B) (1991) 2253–2255.

[31] J. F. Li, K. Takagi, M. Ono, W. Pan, R. Watanabe, A. Almajid, M. Taya, Fabrication and evaluation of porous piezoelectric ceramics and porosity-graded piezoelectric actuators, Journal of the American Ceramic Society 86 (7) (2003) 1094–1098.

[32] S. Marselli, V. Pavia, C. Galassi, E. Roncari, F. Craciun, G. Guidarelli, Porous piezoelectric ceramic hydrophone, Journal of the Acoustical Society of America 106 (2) (1999) 733–738.

[33] R. Y. Ting, Piezoelectric properties of a porous pzt ceramic, Ferroelectrics 65 (1985) 11–20.

[34] J. Ueda, T. W. Secord, H. H. Asada, Large effective-strain piezoelectric actuators using nested cellular architecture with exponential strain amplification mechanisms, Mechatronics, IEEE/ASME Transactions on 15 (5) (2010) 770–782.

[35] U. Bast, W. Wersing, The influence of internal voids with 3-1 connectivity on the properties of piezoelectric ceramics prepared by a new planar process, Ferroelectrics 94 (1989) 229–242.

[36] W. Wirges, M. Wegener, O. Voronina, L. Zirkel, R. Gerhard-Multhaupt, Optimized preparation of elastically soft, highly piezoelectric, cellular ferroelectrets from nonvoided poly(ethylene terephthalate) films, Advanced Functional Materials 17 (2) (2007) 324–329.

[37] E. Roncari, C. Galassi, F. Craciun, C. Capiani, A. Piancastelli, A microstructural study of porous piezoelectric ceramics obtained by different

methods, Journal of the European Ceramic Society 21 (3) (2001) 409–417.

[38] S. H. Lee, S. H. Jun, H. E. Kim, Y. H. Koh, Fabrication of porous pzt-pzn piezoelectric ceramics with high hydrostatic figure of merits using camphene-based freeze casting, Journal of the American Ceramic Society 90 (9) (2007) 2807–2813.

[39] H. Banno, Effects of shape and volume fraction of closed pores on dielectric, elastic and electromechanical properties of dielectric and piezoelectic ceramics - a theoretical approach., American Ceramic Society Bulletin 66 (1987) 1332.

[40] M. L. Dunn, M. Taya, Electromechanical properties of porous piezoelectric ceramics, Journal of the American Ceramic Society 76 (7) (1993) 1697–1706.

[41] M. L. Dunn, H. A. Wienecke, Inclusions and inhomogeneities in transversely isotropic piezoelectric solids, International Journal of Solids and Structures 34 (27) (1997) 3571–3582.

[42] C. R. Bowen, V. Y. Topolov, Piezoelectric sensitivity of PbTiO$_3$-based ceramic/polymer composites with 0-3 and 3-3 connectivity, Acta Materialia 51 (17) (2003) 4965–4976.

[43] T. E. G. Alavarez-Arenas, F. M. Espinosa, Highly coupled dielectric behavior of porous ceramics embedding a polymer, Applied Physics Letters 68 (1996) 263–265.

[44] K. Challagulla, T. A. Venkatesh, Electromechanical response of 2-2 layered piezoelectric composites: A micromechanical model based on the asymptotic homogenization method, Philosophical Magazine 89 (2009) 1197–1222.

[45] P. Bisegna, R. Luciano, On methods for bounding the overall properties of periodic piezoelectric fibrous composites, Journal of the Mechanics and Physics of Solids 45 (1997) 1329–1356.

[46] P. Bisegna, R. Luciano, Variational bounds for the overall properties of piezoelectric composites, Journal of the Mechanics and Physics of Solids 44 (1996) 583–602.

[47] M. Hori, S. Nemat-Nasser, Universal bounds for effective piezoelectric moduli, Mechanics of materials 30 (1) (1998) 1–19.

[48] M. L. Dunn, M. Taya, An analysis of piezoelectric composite materials containing ellipsoidal inhomogeneities, Proceedings of The Royal Society A 443 (1993) 265–287.

[49] M. L. Dunn, M. Taya, Electromechanical properties of porous piezo-electric ceramics, Journal of the American Ceramic Society 76 (1993) 1697–1706.

[50] J. Otero, R. Rodríguez-Ramos, G. Monsivais, R. Perez-Alvarez, Dynamical behavior of a layered piezocomposite using the asymptotic homogenization method, Mechanics of materials 37 (1) (2005) 33–44.

[51] Y. Mikata, Explicit determination of piezoelectric eshelby tensors for spheroidal inclusion, International Journal of Solids and Structures 38 (2001) 7045–7063.

[52] Y. Mikata, Determination of piezoelectric eshelby tensor in transversely isotropic piezoelectric solids, International Journal of Engineering Science 38 (2000) 605–641.

[53] R. Rodríguez-Ramos, F. J. Sabina, R. Guinovart-Díaz, J. Bravo-Castillero, Closed-form expressions for the effective coefficients of a fiber-reinforced composite with transversely isotropic constituents–i. elastic and square symmetry, Mechanics of materials 33 (4) (2001) 223–235.

[54] C. Lee, Theory of laminated piezoelectric plates for the design of distributed sensors/actuators. part i: Governing equations and reciprocal relationships, The Journal of the Acoustical Society of America 87 (1990) 1144.

[55] C. Bowen, V. Y. Topolov, Piezoelectric sensitivity of PbTiO$_3$-based ceramic/polymer composites with 0–3 and 3–3 connectivity, Acta materialia 51 (17) (2003) 4965–4976.

[56] Z. Chen, S. Yu, L. Meng, Y. Lin, Effective properties of layered magneto-electro-elastic composites, Composite Structures 57 (1) (2002) 177–182.

[57] R. Kar-Gupta, T. A. Venkatesh, Electromechanical response of 1-3 piezoelectric composites: An analytical model, Acta Materialia 55 (2007) 1093–1108.

[58] R. Kar-Gupta, C. Marcheselli, T. A. Venkatesh, Electromechanical response of 1–3 piezoelectric composites: Effect of fiber shape, Journal of Applied Physics 104 (2008) 024105–1–17.

[59] H. E. Pettermann, S. Suresh, A comprehensive unit cell model: a study of coupled effects in piezoelectric 1-3 composites, International Journal of Solids and Structures 37 (2000) 5447–5464.

[60] R. Kar-Gupta, T. A. Venkatesh, Electromechanical response of piezoelectric composites: Effects of geometric connectivity and grain size, Acta Materialia 56 (2008) 3810–3823.

[61] R. Kar-Gupta, T. A. Venkatesh, Electromechanical response of 1-3 piezoelectric composites: Effect of poling characteristics, Applied Physics Letters 98 (2005) 054102–1–3.

[62] S. Wang, A finite element model for the static and dynamic analysis of a piezoelectric bimorph, International Journal of Solids and Structures 41 (15) (2004) 4075–4096.

[63] S. Iyer, T. A. Venkatesh, Electromechanical response of porous piezoelectric materials: Effects of porosity connectivity, Applied Physics Letters 97 (7) (2010) 072904. doi:10.1063/1.3481416.
URL http://link.aip.org/link/?APL/97/072904/1

[64] S. Iyer, T. A. Venkatesh, Electromechanical response of (3-0) porous piezoelectric materials: Effects of porosity shape, Journal of Applied Physics 110 (3) (2011) 034109. doi:10.1063/1.3622509.
URL http://link.aip.org/link/?JAP/110/034109/1

[65] R. Kar-Gupta, T. A. Venkatesh, Electromechanical response of porous piezoelectric materials: Effects of porosity distribution, Applied Physics Letters 91 (6) (2007) 062904–3.

[66] C. Marcheselli, T. A. Venkatesh, Electromechanical response of 1-3 piezoelectric composites with hollow fibers, Applied Physics Letters 93 (2) (2008) 022903–022903–3.

[67] P. W. Bosse, K. S. Challagulla, T. A. Venkatesh, Effects of foam shape and porosity aspect ratio on the electromechanical properties of 3-3 piezoelectric foams, Acta Materialia 60 (19) (2012) 6464–6475.

[68] M. F. Ashby, T. Evans, N. Fleck, J. Hutchinson, H. Wadley, Metal Foams: A Design Guide, BUTTERWORTH-HEINEMANN, 2000.

[69] V. S. Deshpande, M. F. Ashby, N. A. Fleck, Foam topology: bending versus stretching dominated architectures, Acta Materialia 49 (6) (2001) 1035–1040.

[70] J. Gibson, L., F. Ashby, M., Cellular Solids: Structure and Properties, 1997.

[71] L. Brillouin, Wave propagation in periodic structures: electric filters and crystal lattices, DoverPublications. com, 2003.

[72] M. S. Kushwaha, P. Halevi, L. Dobrzynski, B. Djafarirouhani, Acoustic band-structure of periodic elastic composites, Physical Review Letters 71 (13) (1993) 2022–2025.

[73] S. Gonella, M. Ruzzene, Analysis of in-plane wave propagation in hexagonal and re-entrant lattices, Journal of Sound and Vibration 312 (1) (2008) 125–139.

[74] J. F. Nye, Physical properties of crystals : their representation by tensors and matrices, Oxford [Oxfordshire] : Clarendon Press ; New York : Oxford University Press, 1984.

[75] R. Kar-Gupta, T. Venkatesh, Electromechanical response of 1-3 piezoelectric composites: Effect of poling characteristics, Journal of applied physics 98 (5) (2005) 054102–054102–14.

[76] R. Kar-Gupta, T. Venkatesh, Electromechanical response of 1-3 piezoelectric composites: A numerical model to assess the effects of fiber distribution, Acta materialia 55 (4) (2007) 1275–1292.

[77] G. C. Saha, A. L. Kalamkarov, A. V. Georgiades, Micromechanical analysis of effective piezoelastic properties of smart composite sandwich shells made of generally orthotropic materials, Smart Materials and Structures 16 (3) (2007) 866–883.

[78] M. Vijaya, Piezoelectric Materials and Devices: Applications in Engineering and Medical Sciences, CRC Press, 2012.

[79] P. W. Bosse, K. S. Challagulla, T. A. Venkatesh, Effects of foam shape and porosity aspect ratio on the electromechanical properties of 3-3 piezoelectric foams, Acta Materialia 60 (19) (2012) 6464–6475.

[80] C. Marcheselli, T. Venkatesh, Electromechanical response of 1-3 piezoelectric composites with hollow fibers, Applied Physics Letters 93 (2) (2008) 022903–022903–3.

[81] J. F. Li, K. Takagi, M. Ono, W. Pan, R. Watanabe, A. Almajid, M. Taya, Fabrication and evaluation of porous piezoelectric ceramics and porosity-graded piezoelectric actuators, Journal of the American Ceramic Society 86 (7) (2003) 1094–1098.

[82] J. Ueda, T. W. Secord, H. H. Asada, Large effective-strain piezoelectric actuators using nested cellular architecture with exponential strain amplification mechanisms, Mechatronics, IEEE/ASME Transactions on 15 (5) (2010) 770–782.

[83] M. Alkhader, M. Vural, The partition of elastic strain energy in solid foams and lattice structures, Acta Materialia 57 (8) (2009) 2429–2439.

[84] J. D. Eshelby, The determination of the elastic field of an ellipsoidal inclusion, and related problems, Proceedings of the Royal Society of London. Series A, Mathematical and Physical Sciences 241 (1957) 376–396.

[85] R. Hill, Discontinuity relations in mechanics of solids, Progress in solid mechanics 2 (72) (1961) 245–276.

[86] L. J. Walpole, The elastic field of an inclusion in an anisotropic medium, Proceedings of the Royal Society of London. Series A, Mathematical and Physical Sciences 300 (1967) 270–289.

[87] N. Kinoshita, T. Mura, Elastic fields of inclusions in anisotropic media, physica status solidi (a) 5 (1971) 759–768.

[88] L. J. Walpole, The determination of the elastic field of an ellipsoidal inclusion in an anisotropic medium, Mathematics Proceedings of the Cambridge Philosophical Society 81 (1977) 283–289.

[89] A. C. Gavazzi, D. C. Lagoudas, On the numerical evaluation of eshelby's tensor and its application to elastoplastic fibrous composite, Computational Mechanics 7 (1990) 13–19.

[90] W. F. J. Deeg, The analysis of dislocation, crack, and inclusion problems in piezoelectric solids, Ph.D. thesis, Stanford Univ., CA. (1980).

[91] B. Wang, Three-dimensional analysis of an ellipsoidal inclusion in a piezoelectric material, International Journal of Solids and Structures 29 (1992) 293–308.

[92] Y. Benveniste, The determination of the elastic and electric fields in a piezoelectric inhomogeneity, Journal of Applied Physics 72 (1992) 1086–1095.

[93] T. Chen, Green's functions and the non-uniform transformation problem in a piezoelectric medium, Mechanics Research Communications 20 (1993a) 271–278.

[94] M. L. Dunn, H. A. Wienecke, Inclusions and inhomogeneities in transversely isotropic piezoelectric solids, International Journal of Solids and Structures 34 (1997) 3571–3582.

[95] J. Michel, H. Moulinec, P. Suquet, Effective properties of composite materials with periodic microstructure: a computational approach, Computer Methods in Applied Mechanics and Engineering 172 (1999) 109–143.

[96] M. Brun, O. Lopez-Pamies, P. Ponte Castañeda, Homogenization estimates for fiber-reinforced elastomers with periodic microstructures, International journal of solids and structures 44 (18) (2007) 5953–5979.

[97] R. Hill, Elastic properties of reinforced solids: some theoretical principles, Journal of the Mechanics and Physics of Solids 11 (5) (1963) 357–372.

[98] J. Michel, H. Moulinec, P. Suquet, A computational scheme for linear and non-linear composites with arbitrary phase contrast, International Journal for Numerical Methods in Engineering 52 (1-2) (2001) 139–160.

[99] G. Bonnet, Effective properties of elastic periodic composite media with fibers, Journal of the Mechanics and Physics of Solids 55 (5) (2007) 881–899.

[100] R. Langley, The response of two-dimensional periodic structures to point harmonic forcing, Journal of sound and vibration 197 (4) (1996) 447–469.

[101] O. Sigmund, J. S. Jensen, Systematic design of phononic band-gap materials and structures by topology optimization, Philosophical Transactions of the Royal Society of London Series a-Mathematical Physical and Engineering Sciences 361 (1806) (2003) 1001–1019.

[102] M. Ruzzene, F. Scarpa, F. Soranna, Wave beaming effects in two-dimensional cellular structures, Smart materials and structures 12 (3) (2003) 363.

[103] S. M. Jeong, M. Ruzzene, Analysis of vibration and wave propagation in cylindrical grid-like structures, Shock and Vibration 11 (3) (2004) 311–331.

[104] A. S. Phani, J. Woodhouse, N. Fleck, Wave propagation in two-dimensional periodic lattices, The Journal of the Acoustical Society of America 119 (2006) 1995.

[105] A. Diaz, A. Haddow, L. Ma, Design of band-gap grid structures, Structural and Multidisciplinary Optimization 29 (6) (2005) 418–431.

[106] K. Bertoldi, M. C. Boyce, Mechanically triggered transformations of phononic band gaps in periodic elastomeric structures, Physical Review B 77 (5).

[107] K. Bertoldi, M. C. Boyce, Wave propagation and instabilities in monolithic and periodically structured elastomeric materials undergoing large deformations, Physical Review B 78 (18).

115

[108] A. Khelif, B. Aoubiza, S. Mohammadi, A. Adibi, V. Laude, Complete band gaps in two-dimensional phononic crystal slabs, Physical Review E 74 (4).

[109] S. Mohammadi, A. A. Eftekhar, A. Khelif, H. Moubchir, R. Westafer, W. D. Hunt, A. Adibi, Complete phononic bandgaps and bandgap maps in two-dimensional silicon phononic crystal plates, Electronics Letters 43 (16) (2007) 898–899.

[110] M. Maldovan, Sound and heat revolutions in phononics, Nature 503 (7475) (2013) 209–217.

[111] M. Ruzzene, F. Scarpa, Directional and band-gap behavior of periodic auxetic lattices, physica status solidi (b) 242 (3) (2005) 665–680.

[112] M. Collet, M. Ouisse, M. Ruzzene, M. N. Ichchou, Floquetbloch decomposition for the computation of dispersion of two-dimensional periodic, damped mechanical systems, International Journal of Solids and Structures 48 (20) (2011) 2837–2848.

[113] D. Mead, A general theory of harmonic wave propagation in linear periodic systems with multiple coupling, Journal of Sound and Vibration 27 (2) (1973) 235–260.

[114] A. Spadoni, M. Ruzzene, S. Gonella, F. Scarpa, Phononic properties of hexagonal chiral lattices, Wave Motion 46 (7) (2009) 435–450.